

MSc Thesis  
Earth Structure and Dynamics  
Utrecht University

April 3<sup>rd</sup>, 2019



**Universiteit Utrecht**

**Petrogenesis and peak metamorphic conditions of the Sara's Lust  
Gneisses, Suriname**

Jeroen Goumans

1<sup>st</sup> supervisor: Prof. Dr. Paul Mason  
2<sup>nd</sup> supervisor: Dr. Leo Kriegsman

## **Abstract**

The Sara's Lust Gneisses are a recently separately named formation adjacent to the Marowijne Greenstone Belt in the Guiana Shield, Suriname. They comprise granitoids, amphibolites, mafic volcanics and plutons, and greywackes, which all underwent metamorphism up to amphibolite facies. Contact relationships between these gneisses and the lower grade metamorphic Marowijne Greenstone Belt are not well constrained and as a result, the geological relationship between the two is unknown. In this study emphasis is placed on the petrogenesis and metamorphic history of the Sara's Lust Gneisses. New petrographical data, bulk rock major and trace element chemistry data, mineral chemistry data and metamorphic peak conditions of the Sara's Lust Gneisses are presented in this report. Pseudosections, modelled with *Perple\_X*, and geothermometric calculations yield peak pressures of 4.6 - 5.5 ( $\pm 1$ ) kbar and temperatures 617 - 688 ( $\pm 50$ ) °C. Further, the mafic suite of the Sara's Lust Gneisses exhibits a high content of incompatible elements, which is construed with a plume-derived petrogenesis. The granitoids in the Sara's Lust Gneisses are A-type and their chemistry implies that they were generated in an ocean ridge. As their magmatic age ( $2.156 \pm 12$  Ga) is coeval with the subduction event of the Transamazonian Orogeny (2.18 - 2.13 Ga), these granitoids are interpreted to have formed in a back-arc basin setting. This is in contrast with other granitoids in the Marowijne Greenstone Belt, as these are mainly associated with arc-volcanism. Consequently, due to this spatial difference in the former subduction zone, it is likely that the Sara's Lust Gneisses neither represent the lower crustal equivalent, nor the basement of the Marowijne Greenstone Belt. Rather, they were situated adjacently to one another. During collision (2.11 - 2.08 Ga) the Marowijne Greenstone Belt was likely thrust onto the Sara's Lust Gneisses. This event resulted in metamorphism of the Sara's Lust Gneisses ( $2.084 \pm 18$  Ga). The provenance of the metagreywackes does not show a detectable influence of TTG material, which is in agreement with deposition in a back-arc basin setting. Hence, the petrogenetic history of the Sara's Lust Gneisses, and on a larger scale the Guiana Shield, is consistent with a shift in tectonic style from a mantle-plume upwelling style from the earliest part of Earth history towards modern-day horizontal tectonics.

## Table of contents

1. Introduction .....	3
2. Geological background.....	10
3. The Transamazonian Orogeny .....	11
4. Methodology .....	13
4.1. Light microscopy.....	13
4.2. X-ray Fluorescence.....	13
4.3. Laser Ablation Induced Coupled Mass Spectrometry.....	13
4.4. Electron Probe Micro Analysis .....	13
4.5. Geochronology .....	14
4.6. Perple_X modelling.....	14
5. Results .....	15
5.1. Petrography .....	15
5.2. Rock classification based on bulk rock chemistry.....	42
5.3. Major element geochemistry .....	47
5.4. Trace element geochemistry.....	49
5.4.1. General trace element trends in the Sara's Lust Gneisses .....	55
5.4.2. Trace element geochemistry of the mafic to intermediate suite.....	55
5.4.3. Trace element geochemistry of the felsic suite .....	55
5.4.4. Trace element geochemistry of the sedimentary suite.....	57
5.5. Electron Microprobe Analysis.....	57
5.5.1. Biotite .....	62
5.5.2. Amphibole .....	63
5.5.3. Feldspar .....	64
5.5.4. Garnet .....	65
5.5.5. Fibrolite .....	65
5.5.6. Opaques .....	66
5.5.7. Chlorite.....	66
6. Discussion .....	67
6.1. Peak metamorphic conditions.....	67
6.1.1. Pseudosections.....	67
6.1.2. Geothermometry.....	74
6.1.2.1 Biotite complications for geothermometry.....	74
6.1.2.2. Garnet complications for geothermometry.....	75

6.1.2.3. Pressure-Temperature relationship .....	76
6.1.3. Peak pressure and temperature .....	76
6.2. Trace element geochemistry .....	82
6.2.1. General anomalies .....	83
6.2.1.1. Large ionic lithophile elements .....	83
6.2.1.2. Nb, Ta, Ti .....	83
6.2.2. Trace element geochemistry of the meta-mafic to intermediate rocks and tectonic implications .....	83
6.2.3. Trace element geochemistry of the felsic suite and tectonic implications .....	88
6.2.4. Trace element geochemistry of the meta-sediments.....	90
6.3. The Sara's Lust Gneisses within the context of the Transamazonian Orogeny .....	90
6.3.1. Relationships between the Sara's Lust Gneisses and the Marowijne Greenstone Belt ...	90
6.3.1.1. The mafic to intermediate suite .....	90
6.3.1.2. The felsic suite.....	93
6.3.1.3. KG1006 .....	95
6.3.1.4. The sedimentary suite.....	96
6.3.2. Metamorphism.....	98
6.3.3. A tectonic relationship between the Sara's Lust Gneisses and the Marowijne Greenstone Belt .....	98
6.4. Geodynamic model.....	99
6.5. Geometric implications for the Transamazonian subduction zone.....	100
6.6. Comparison with the Birimian Terranes .....	100
7. Conclusion.....	101
8. Acknowledgements .....	102
9. References .....	102
Appendix A .....	109
Appendix B .....	113

## 1. Introduction

The Amazonian Craton forms the core of the continent of South America. This craton is divided by the Amazon-Solimões basin into the Central Brazilian Shield and the Guiana Shield (Figure 1). Two Archean nuclei have been recognised in the Guiana Shield: at the western edge (the Imataca Complex, Venezuela (Montgomery and Hurley, 1978)) and at the eastern edge (the northwest of Pará and the central and southwest of Amapá, Brazil (Rosa Costa et al., 2003)). Beside these Archean nuclei, the Guiana Shield predominantly comprises Paleoproterozoic crust. In the north of the shield, a TTG (Tonalite, Trondhjemitite, Granodiorite)-greenstone terrane is present, called the Marowijne Greenstone Belt. This belt stretches over 1500 km from Brazil to the north coast of Venezuela. The Sara's Lust Gneisses abut the Marowijne Greenstone Belt in the north and southwest of the belt (Figure 2). These gneisses were recently excluded from the Coeroeni area, for they yielded a higher estimated age (Kroonenberg et al., 2016). As a result, the Sara's Lust Gneisses are now defined as a formation on their own, of which little is currently known. This is mainly due to the fact that the Guiana Shield is almost entirely covered by dense tropical rainforest and is deeply weathered. As a consequence, geological fieldwork and sampling is difficult. The exact ages of the Sara's Lust Gneisses remains unknown and geological relationships between the Sara's Lust Gneisses and the adjacent Marowijne Greenstone Belt are currently poorly constrained. Cratons are the only pieces of crust where Precambrian formations, such as the Sara's Lust Gneisses, are preserved and are therefore crucial for studying Precambrian geological processes, such as plate tectonics. Studying such ancient rocks will eventually provide better constraints on the tectonic evolution during early Earth's history.



Figure 1 - The Amazonian Craton consists of the Guiana Shield and the Brazilian Shield. These shields are separated by the Amazon-Solimões basin. After Kroonenberg et al., 2016.

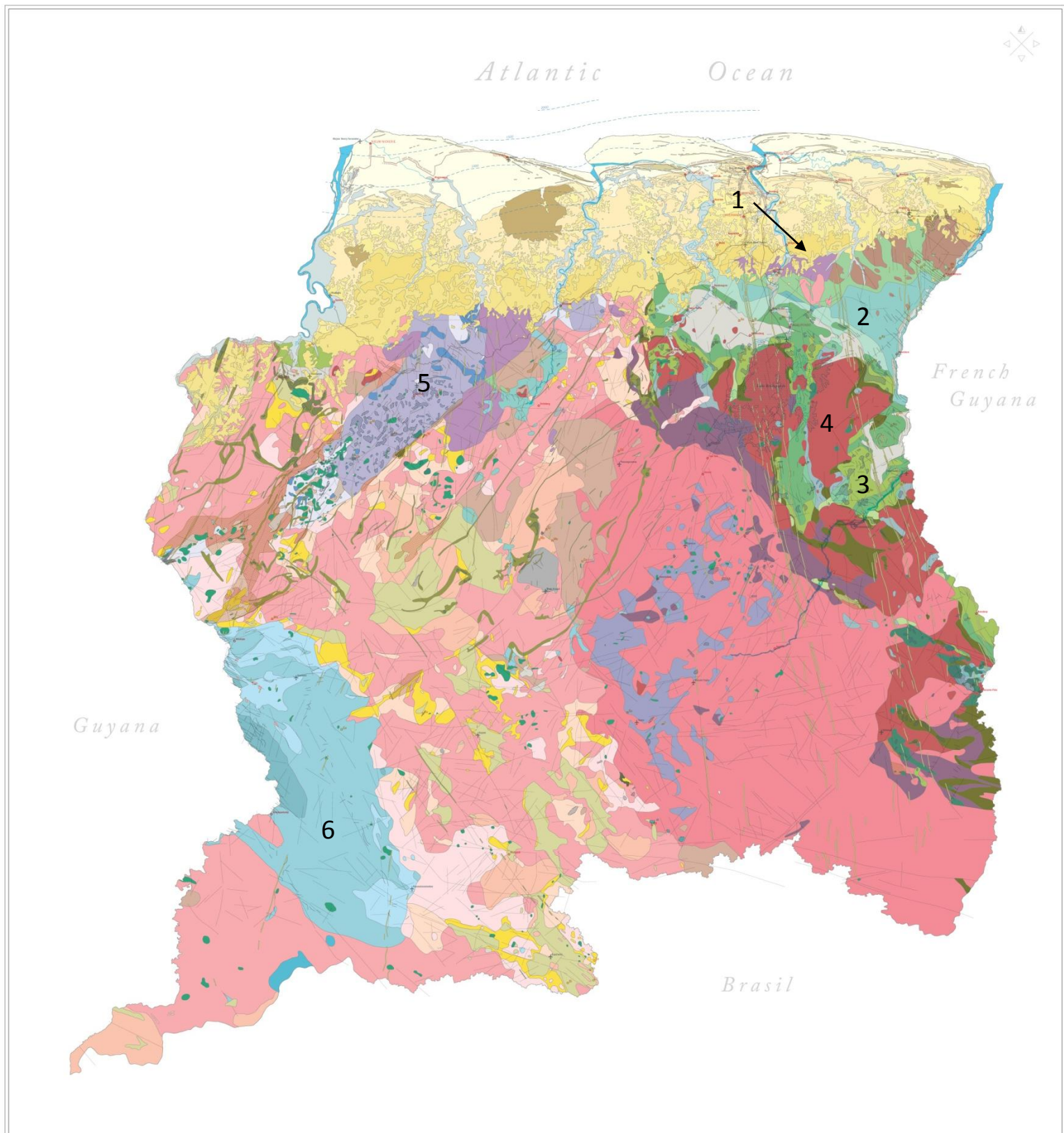


Figure 2 - Geological map of Suriname, produced by TNO (2018). This study focuses on the northern section of the Sara's Lust Gneisses, indicated with a black arrow. Important formations: Sara's Lust Gneisses in light purple (1), the Marowijne Greenstone Belt includes the Paramaka Formation in several shades of green (2) and the Armina Formation in turquoise (3), the Kabel Tonalite in dark red (4), the Bakhuis Granulite Belt in violet (5), the Cauarane-Coeroeni Gneiss Belt in blue (6).

Greenstone belts are solely preserved on cratons (Anhaeusser et al., 1969). The lithology and structure of greenstone belts can vary highly, contributing to their geological complexity (Anhaeusser, 2014). As a consequence, a straightforward definition for a greenstone belt is currently lacking. However, a general description of Furnes et al. (2015) reads that greenstone belts are *elongated to variably-shaped terranes of variable length and width, consisting of spatially and temporally related, Archean to Proterozoic intrusive and extrusive ultramafic, mafic to felsic rocks commonly associated with variable amounts and types of metasedimentary rocks, and intruded by granitoid plutons*. The term 'greenstone belt' was first used by Logan (1863), basing his definition on the presence of the green minerals chlorite, hornblende and epidote. These are present due to greenschist facies metamorphism that greenstone belts have predominantly undergone. Greenstone belts often contain numerous granitoid plutons and are regularly described as granite-greenstone terranes. These plutons compose a major part of the Archean crust. Much of these ancient granitoids fall in the Tonalite-Trondhjemite-Granodiorite (TTG) suite (Condie, 1981). For a granitoid to be classified as a TTG, it must possess several geochemical characteristics, of which the most notable are a high sodic content, relatively high Light Rare Earth Elements (LREE) and correspondingly low Heavy Rare Earth Elements (HREE) content.

The petrogenesis of greenstone belts with TTG and granite intrusions is a matter of debate. With respect to the onset of subduction, the tectonic environment of such rocks is currently enigmatic. Favouring Archean subduction, Arndt (2013) states that subduction zones are the only domains known where wet melting can readily occur due to the introduction of the hydrated slab in the mantle wedge. As a result, subduction zones are highly efficient felsic rock producers. In his view, the presence of primitive subduction zones in the Archean are the key to explaining why such extensive granite and TTG intrusions are present in Archean greenstone belts.

Another argument in favour of Archean subduction is that it explains the depletion in HREE in TTGs (Martin, 1987). This depletion is often attributed to partial melting of eclogitic crust. Garnet, being relatively rich in HREE, will remain stable in the residue as a peritectic phase, which in turn causes the melt to become low in HREE. A TTG melt, therefore, must have been generated in the garnet stability field, thus at relatively high pressure. Such a high pressure would advocate for the requirement of subduction processes for TTG generation. It has, however, been questioned if the HREE depletion of TTGs is a direct indicator for subduction. Condie (1981) states that the geochemistry of TTGs merely evidences partial melting of hydrated basaltic rocks which have undergone metamorphism towards garnet-bearing amphibolites or eclogite. Consequently, the geochemistry of TTGs would only imply that these were generated at high depths and that subduction is not necessarily invoked. Contrastingly, Martin (1999) found that TTGs share many geochemical features with modern day arc lavas called adakites that are interpreted in terms of slab melting. Their similarity would indicate that these rock

types have formed in a similar tectonic environment. In addition, seismic indicators are found for fossil Archean subduction plates (Calvert et al., 1995; De Wit & Tinker, 2004) implying that subduction was an operating process in the Archean.

Gneiss complexes in Archean terranes, such as those in West Greenland and in Swaziland, contain sheath folds, boudins, large-scale simple-shear deformation zones and nappe structures (McGregor, 1973; Jackson, 1984) (Figure 3a). Such structures are interpreted to imply horizontal shortening, thereby providing an indication for plate tectonics and subduction. Contrastingly, other greenstone belts, such as those found in the Dharwar Craton in India and the Eastern Pilbara region in Australia, exhibit structures which have evidently formed by non-plate tectonic processes (Figure 3b). These greenstone belts have a dome-like structure and comprise plutonic domes surrounded by ring faults (Gorman et al., 1978; Hickman, 1984; Bouhallier et al., 1995; Van Kranendonk et al., 2007). Such a structure is expectedly formed by gravity driven diapirism. In these models, a stagnant lithosphere is assumed where the crust was not broken up in individual plates. Convection still occurred but was restricted to the mantle. These convective cycles could cause upwelling of light felsic material and downwelling of heavy mafic material.

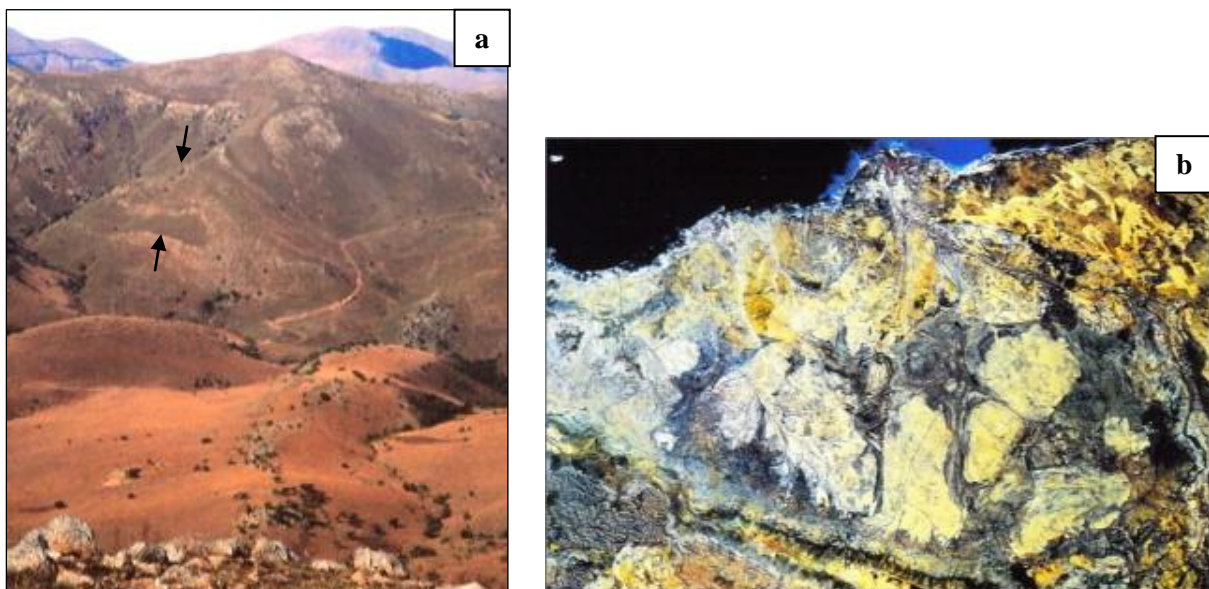


*Figure 3- a) Field image of nappe-like folds in the Barberton Greenstone Belt, indicated with the black arrows. b) Satellite image of the Western Pilbara Craton, illustrating the dome and basin structure. The image is ~400 km wide. Both images are after Anhaeusser (2014).*

Downwelling could cause the formation of granite-greenstone terranes by crustal delamination (Zegers & Van Keken, 2001) (Figure 4a). In such a model heavy eclogitic lower crust detaches and sinks in the mantle. This leads to upwelling and partial melting of the mantle increasing the temperature in the crust such that the lower crust partially melts, hence resulting in TTG melt production. Upwelling can



be explained in a plume-like setting (Figure 4b). A plume can form oceanic plateaus due to repetitious melting of oceanic crust. These can become as thick as 35 - 40 km, sufficient for the necessary pressure for garnet to be stable. Hence, an oceanic plateau could provide the required conditions for TTG melt production (Moyen & Martin, 2012). However, as already mentioned, another requirement for the generation of TTG is a hydrated source. The base of oceanic plateaux is in essence anhydrous. As a result, only small amounts of felsic magmas can be produced which does not match the high abundance of TTGs in cratons (Arndt, 2013). Moreover, typical felsic melts in oceanic plateau settings exhibit a different geochemistry in comparison with TTGs, with a higher abundance of HREEs and absence of negative Nb and Ta anomalies in the former (Martin et al., 2008).

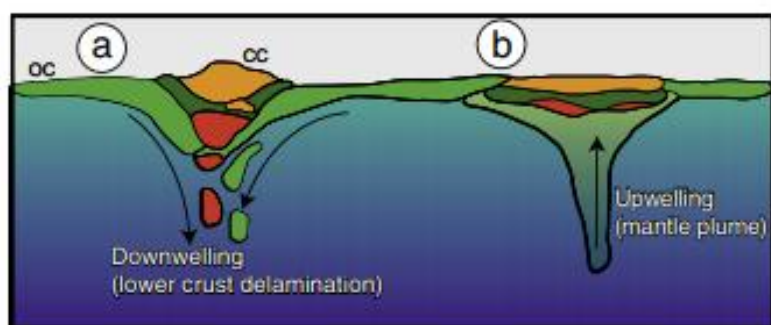


Figure 4 - a) Downwelling theory with crustal delamination. b) Upwelling theory invoking a mantle plume. After Moyen & Martin, 2012.

Another line of evidence opposing Archean subduction is the work of Labrosse & Jaupart (2007). They argued that the Earth was 200 °C hotter in the Archean than it is today. The lithosphere was, as a consequence, more buoyant. This makes it more difficult to subduct material and it is arguable if subduction is even possible with a much higher buoyancy counterforce. Models comprising gravity driven diapirism intuitively fit a hotter Earth. In addition, Stern (2008) states that lithological indicators for subduction, such as blueschists, ophiolites, eclogites and mélanges are absent in Archean terranes and argues that the lack of these indicators in Archean crust implies that modern-day subduction was not an ongoing process in the Archean.

Lastly, some greenstone belts, such as the Belingwe Greenstone Belt, Zimbabwe (Bickle et al., 1975) and the Abitibi Greenstone Belt, Canada (Barnes et al., 1983), include komatiite volcanism. The formation of these extremely high temperature magnesium-rich lavas may require the involvement of a mantle plume as a heat source (Fyfe, 1978; Nisbet et al., 1993).

It is unlikely that one particular tectonic style was responsible for the formation of granite-greenstone terranes. This is especially well-demonstrated with the contrast of tectonic settings between the Eastern and Western Pilbara Craton, Australia. Smithies et al. (2006) showed that the Pilbara Craton can be subdivided into the 3.53 - 3.2 Ga old plume-generated Eastern Pilbara Craton and the dome-

structure-lacking and younger 3.3 - 3.05 Ga old Western Pilbara Craton possessing geochemical indicators for subduction. It has, hence, been argued that the oldest greenstone belts were formed by within-plate processes but that subduction occurred at least locally in the late Archean (Moyen & Martin, 2012).

Moyen (2011) postulated that TTG rocks comprise a wide range of granitic rocks with slightly varying composition and he subdivided the TTG suite in a high-, medium- and low-pressure group. The melting temperatures of these sub-groups is, however, similar (Moyen & Martin, 2012). This results in varying geothermal gradients for the three TTG sub-groups which is unexplainable with a single tectonic setting. Rather, the high-pressure TTGs are probably associated with subduction and the low-pressure TTGs are more likely to be produced in an oceanic plateau or plume-like setting. The medium-pressure TTGs formed along a geothermal gradient assumed to be too high for subduction to operate and too low for a plateau-like setting. It is, therefore, plausible that the medium-pressure sub-group can be generated in different tectonic environments.

With respect to the discussion between horizontal and vertical tectonics, the tectonic evolution of the Guiana Shield is thought to exemplify the transition between the two contrasting tectonic styles (Vanderhaeghe et al., 1998). Structurally, the Paleoproterozoic Marowijne Greenstone Belt is very similar to the dome-and-basin-like structures of Archean greenstone belts which have formed prior to subduction according to these authors. Yet, during the Transamazonian Orogeny the Guiana Shield and the West African Shield collided and formed a new supercontinent, resembling modern-day orogenic events.

Contact relationships between older gneisses and greenstone belts are often not well constrained and this is also the case for the Sara's Lust Gneisses and the Marowijne Greenstone Belt. This makes it challenging to constrain the geological relationship between the potentially older gneisses and the greenstone belt. Three theories are preliminarily proposed all plausibly explaining the higher-grade metamorphic Sara's Lust Gneisses abutting the lower-grade metamorphic Marowijne Greenstone Belt: 1) The Sara's Lust Gneisses could represent the basement upon which the sedimentary and volcanic sequences of the greenstone belt were deposited, as is for example the case for the Yangtze Block in the North China Craton (Jiao et al., 2009). In this scenario, the Sara's Lust Gneisses need to be older than the Marowijne Greenstone Belt. 2) The Sara's Lust Gneisses have a direct petrogenetic relationship with the Marowijne Greenstone Belt, where the Sara's Lust Gneisses could be the lower crustal equivalent of the lower-grade metamorphic Marowijne Greenstone Belt. This hypothesis has also been advanced for the felsic volcanics peripheral to the Barberton Greenstone Belt, South Africa (De Wit et al., 1987). This theory would potentially be supported by the two formations being geochemically similar and yielding a comparable age. 3) The Sara's Lust Gneisses and the Marowijne Greenstone Belt could have a tectonic relationship, where the Marowijne Greenstone Belt thrust

onto the Sara's Lust Gneisses with consequent higher-grade metamorphism in the Sara's Lust Gneisses. In this scenario, the Marowijne Greenstone Belt is allochthonous and a petrogenetic connection is not necessarily the case.

This study focuses on the petrogenesis and metamorphic history of the Sara's Lust Gneisses. Drill cores of ~15 cm long and rock samples of ~20 cm diameter from the northern section of the Sara's Lust Gneisses were provided by Prof. Dr. Salomon Kroonenberg. Figure 5 shows the locations from where the rock samples have been taken. These samples were be analysed geochemically and petrographically. One aim of this thesis is to derive the peak metamorphic conditions that the Sara's Lust Gneisses were subjected to, providing new constraints on their geological evolution. Petrographic analysis, mineral chemistry using the Electron Probe Microanalyser (EPM) and bulk rock geochemistry analysis with X-Ray Fluorescence (XRF) enable the construction of pseudosections to constrain the peak metamorphic conditions to which the Sara's Lust Gneisses were subjected to. Further, the protoliths of the Sara's Lust Gneisses were determined through petrographic research and major and trace element geochemistry, using XRF analysis and Laser Ablation Induced Coupled Plasma-Mass Spectrometry (LA-ICP-MS). The tectonic setting(s) is / are interpreted through trace element geochemistry. The data combined will enable comparing the Sara's Lust Gneisses with other formations within the Marowijne Greenstone Belt to investigate their geological link. Finally, a geodynamic model is proposed summarising the petrogenetic history of the Sara's Lust Gneisses.

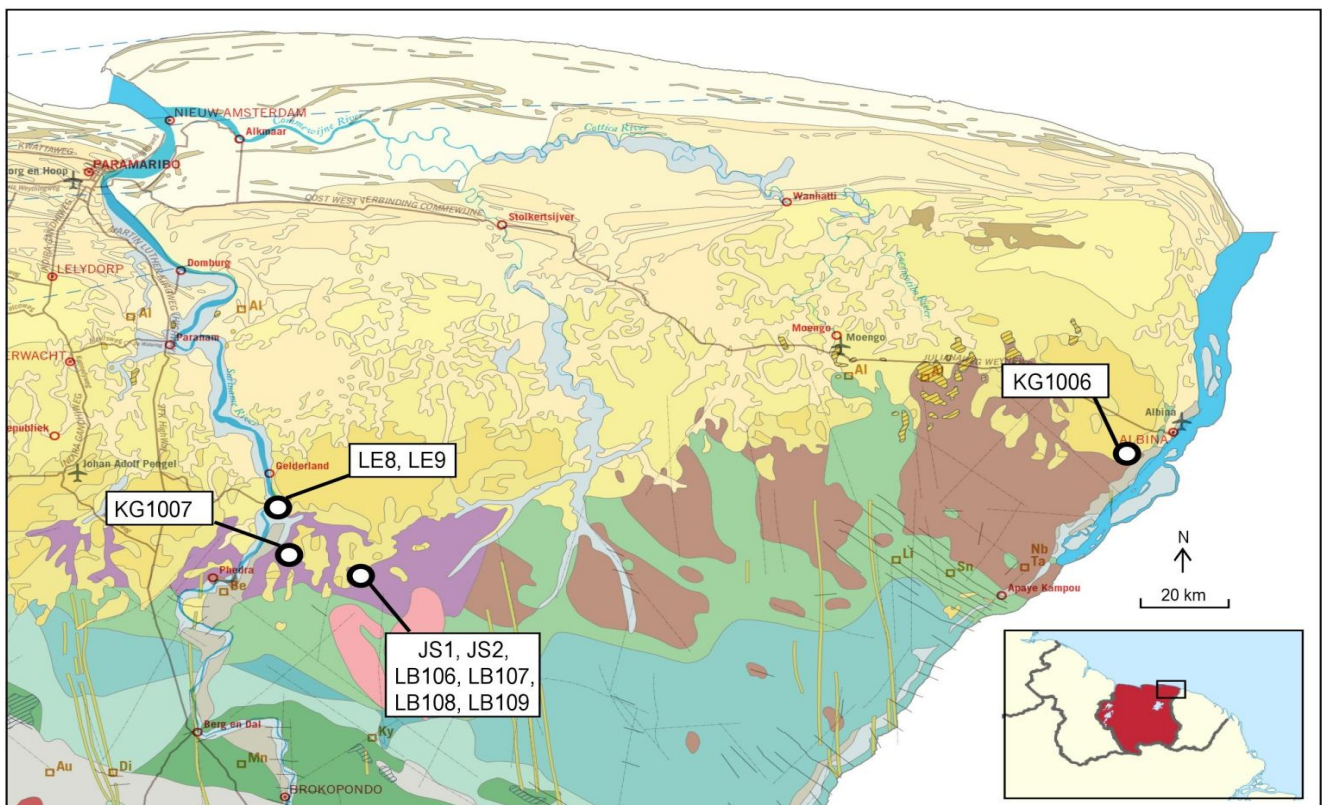


Figure 5 -The geological map of Suriname zoomed in to the Sara's Lust Gneisses showing the sample locations.

## 2. Geological background

The Marowijne Greenstone Belt is subdivided into several formations: 1) the Paramaka Formation, composed of mafic volcanic rocks including pillow lavas, 2) the Armina Formation, comprising metagreywackes and phyllites representing metaturbidites, 3) the Rosebel Formation, overlying the Paramaka and Armina Formation and consisting of metaconglomerates and meta-arenites, 4) the Bemau Ultramafite which is composed of minimally two generations of mafic to ultramafic plutons, 5) TTG and granite plutons that have intruded the Armina formation. These granitoids include the Akinto Soela Granite, the Kabel Tonalite, the Patamacca Two-Mica Granite, the Phedra Granite and the Tibiti Granite, (Bleys, 1951; Schols & Cohen, 1951; Bosma et al., 1983, 1984; Veenstra, 1983; Delor et al., 2003a; Yang, 2014; Kroonenberg et al., 2016; Kromopawiro, 2019). The Marowijne Greenstone Belt is bordered in the south by a felsic metavolcanic belt called the Dalbana Formation (Bosma, 1971). In the south, the Dalbana Formation is, in turn, bounded by the Central Guiana Belt (De Roever et al., 2015). This belt consists of two sections: the Cauarane-Coeroeni Gneiss Belt and the Bakhuis Granulite Belt. The Cauarane-Coeroeni Gneiss Belt chiefly comprises amphibolite- to granulite-facies quartzofeldspathic gneisses and metapelitic gneisses (Kroonenberg, 1976). The Bakhuis Granulite Belt consists of granulites of intermediate and mafic composition with peak metamorphic conditions up to 1050 °C and 9 kbar (De Roever et al., 2003). A 3 km thick sedimentary unit called the Roraima Supergroup was deposited on top of the aforementioned formations (Reis et al., 1990). This unit consists of sequences of sandstones, conglomerates and tuffs. Furthermore, the Avanavero Dolerites cross-cut all earlier units and are present as dykes and sills (Reis et al., 2013). In the west of the Guiana Shield high-grade metamorphic rocks are located comprising the Rio Negro Belt (Tassinari et al., 1996).

In the north and southwest, the Marowijne Greenstone Belt is flanked by the Sara's Lust Gneisses (Bosma et al., 1983, 1984, Kroonenberg et al., 2016) (Figure 2). In the southwestern flank, the Sara's Lust Gneisses predominantly consist of garnet-biotite gneisses, andalusite-cordierite sillimanite schists and ortho- and clinopyroxene gneisses, in which the presence of orthopyroxene, if metamorphic, would evidence that metamorphic conditions were up to granulite facies. It is, however, unknown whether orthopyroxene is present as a magmatic or a metamorphic mineral. Nonetheless, the Sara's Lust Gneisses mainly consist of amphibolite facies metamorphic rocks (Barink, 1975; Ho Len Fat, 1975). The southwestern section of the Sara's Lust Gneisses continues into South Guiana as the Tamouri Complex, yielded Pb-evaporation ages on zircons of 2.165 - 2.155 Ga ( $\pm$  6 Ma) (Delor et al., 2003a). The northern section of the Sara's Lust Gneisses mainly consists of hornblende-biotite gneisses, garnet-biotite gneisses, biotite-plagioclase gneisses, quartzofeldspathic gneisses, sillimanite-biotite-muscovite gneisses, amphibolites and calc-silicate rocks (Kroonenberg et al., 2016). The gneisses are, to a certain extent, migmatized (Bosma, 1983). The amphibolites locally contain garnet

and clinopyroxene indicating that metamorphic conditions were reached to upper amphibolites facies metamorphism (Kroonenberg et al., 2016).

### **3. The Transamazonian Orogeny**

The formation of the crust of the Guiana Shield is chiefly attributed to the Transamazonian Orogeny (2.26 - 2.09 Ga), which was first defined by Hurley et al. (1967). Prior to this orogenic event, tholeiitic gabbros were produced around 2.26 Ga in the Île de Cayenne in French Guiana (Delor et al., 2003a). This stage lasted until around 2.20 Ga (Figure 5, stage 1). The tectonic setting of the formation of the rocks from the Île de Cayenne has been a matter of debate. According to Vanderhaeghe et al. (1998) these metavolcanics possess similar geochemical characteristics as volcanics derived from a mid-oceanic ridge or back-arc basin. This theory was further worked out by Delor et al. (2003a) (Figure 5). A mid-oceanic ridge or back-arc basin, however, is dissimilar with the proposed petrogenesis of the juvenile oceanic crust of the Birimian terranes, located on the West African Craton. This craton formerly coalesced with the Guiana Shield, making proposed tectonic settings for the West African Craton arguably representative for the Guiana Shield. For the West African Craton the involvement of a mantle plume is postulated (Abouchami et al., 1990; Boher et al., 1992), basing their proposition on comparing the geochemistry of Birimian basalts with MORB composition and plume-derived basalts. A mantle plume would have generated vast volumes of juvenile magmas, composing an oceanic plateau. Opposing Vanderhaeghe's (1998) and Delor's (2003a) proposition, Velasquez et al. (2011) found geochemical indicators in basalts from Venezuela that fit a mantle plume-related setting in the Guiana Shield.

The first event (2.18 - 2.13 Ga) of the Transamazonian Orogeny comprises the subduction of oceanic crust below the Guiana Shield due to the convergence between the Guiana Shield and the West African Shield. This led to the generation of TTG intrusions (Vanderhaeghe et al., 1998; Delor et al., 2003a) (Figure 5, stage 2 & 3). The volcanic suites of the Paramaka Formation yield a geochemical back-arc affinity and are consequently interpreted to be formed in the back-arc of the Transamazonian subduction zone (Veenstra, 1983; Daoust et al., 2011; Kroonenberg et al., 2016; Kromopawiro, 2019). Subsequent emergence of the volcanic arc resulted in the formation of turbidity currents, which deposited the greywackes of the Armina Formation (Daoust et al., 2011; Naipal & Kroonenberg, 2016). The continued convergence led to collision of the West African Shield and the Guiana Shield (2.11 - 2.08 Ga) (Figure 5, stage 4). A shift in tectonic style in this stage is recognised in the Rosebel Formation, which is interpreted as the fluvial infill of newly formed pull-apart basins due to oblique plate convergence (Delor 2003a, 2003b; Daoust et al., 2011). This phase resulted amongst others in the generation of the Patamacca Two - Mica Granite intruding the Armina Formation.

Contemporaneously, the Bemau Ultramafites intruded in the Paramaka Formation (Kroonenberg et al., 2016).

The collisional stage was followed by a crustal thinning event (2.07 - 2.06 Ga) (Figure 5, stage 5). The Cauarane Coeroeni Gneiss Belt and Bakhuis Granulite Belt underwent HT-LP metamorphism (Kroonenberg, 1975, Delor et al., 2003b). Mantle upwelling has been invoked to provide the high temperatures during metamorphism, as recorded in the Bakhuis Granulite Belt and the Cauarane - Coeroeni Gneiss Belt (Delor et al., 2003a; Daoust et al., 2011). The Transamazonian Orogeny was followed by a phase of extensive magmatism (1.99 - 1.95 Ga). This phase comprises the generation of vast amounts of magmas, including charnockites, mafic and felsic intrusions, of which the latter is the Dalbana Formation (Bosma et al., 1983; Bosma et al., 1984; Delor et al., 2003b). The extensive plutonism was generated in a post-collisional setting (Reis et al., 2000) and likely provided UHT conditions necessary for the generation of charnockites (Klaver et al., 2015).

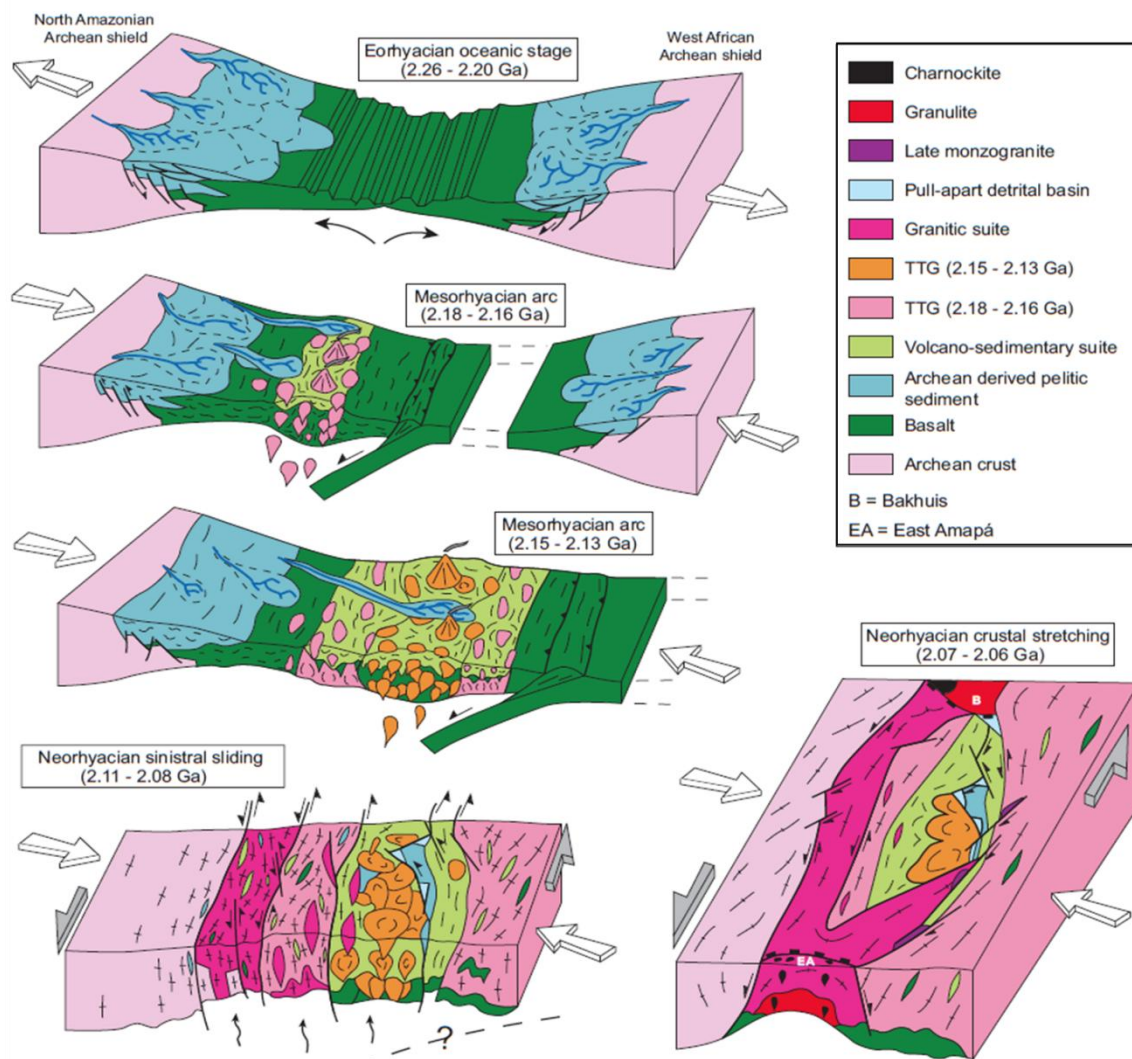


Figure 6 - Geodynamic model comprising the different stages of the Transamazonian Orogeny. After Delor et al., 2003a.

## **4. Methodology**

### **4.1. Light microscopy**

Thin sections of all the 16 rock samples were produced for petrographic research. Petrography was carried out with a Zeiss Axio transmitted light microscope, equipped with a coupled digital camera for high resolution photographs. Preliminary protolith identification, rock type classification and estimations of the metamorphic facies were conducted based on petrography.

### **4.2. X-ray Fluorescence**

X-ray fluorescence was carried out to analyse the bulk rock chemistry of the rock samples. The Thermo ARL 9400 sequential XRF at the Geo Lab of Utrecht University was equipped with a rhodium tube. The rock samples were crushed and non-altered rock chips were picked for analysis. These chips were grinded to a powder. Of about 10 - 30 grams of rock powder glass fusion beads were prepared for XRF analysis. The standards ISE921, GSD1 and GSS2 were used for the calibration of the data. The oxide concentrations were corrected for any effects of Loss On Ignition (LOI).

### **4.3. Laser Ablation Induced Coupled Mass Spectrometry**

The same glass fusion beads were used for trace element geochemical analysis with Laser Ablation Inductively Coupled Plasma Mass Spectrometry. Trace element analysis was conducted with a ThermoFischer Scientific Element 2 magnetic sector ICP-MS and a 193 nm Lambda Physik excimer laser with GeoLas optics, situated at the GeoLab of Utrecht University. XRF and LA-ICP-MS data were calibrated based on Si content. Background contamination was subtracted from the sample trace element content. Each sample was analysed three times for one minute so that any chemical heterogeneity and analytical errors could be averaged out. The spectrometer operated with a pulse energy of 11 J/cm<sup>2</sup>, a spot size of 120 µm and a repetition rate of 10 Hz. Laser data were processed with the GLITTER software. The isotopes used for the calculation of the concentrations are reported in Table 21. Calibration was performed against NIST 612 glass and BCR2-G was used as a secondary standard to assess accuracy, which was typically within 10% of reference values. The used isotopes for the analysis of element concentrations are <sup>45</sup>Sc, <sup>49</sup>Ti, <sup>51</sup>V, <sup>52</sup>Cr, <sup>59</sup>Co, <sup>60</sup>Ni, <sup>63</sup>Cu, <sup>66</sup>Zn, <sup>85</sup>Rb, <sup>88</sup>Sr, <sup>89</sup>Y, <sup>90</sup>Zr, <sup>93</sup>Nb, <sup>133</sup>Cs, <sup>137</sup>Ba, <sup>139</sup>La, <sup>140</sup>Ce, <sup>141</sup>Pr, <sup>146</sup>Nd, <sup>147</sup>Sm, <sup>151</sup>Eu and <sup>153</sup>Eu, <sup>157</sup>Gd, <sup>159</sup>Tb, <sup>163</sup>Dy, <sup>165</sup>Ho, <sup>166</sup>Er, <sup>172</sup>Yb, <sup>175</sup>Lu, <sup>178</sup>Hf, <sup>181</sup>Ta, <sup>208</sup>Pb, <sup>232</sup>Th and <sup>238</sup>U. The isotope concentrations were converted to element concentrations using the natural abundances of the isotopes.

### **4.4. Electron Probe Micro Analysis**

Based on petrography, 3 samples (LB106A, LB106B and LE9) were selected for Electron Probe Micro analysis using the JEOL JXA-8530F Hyperprobe Field Emission Electron Probe Microanalyser, situated at the GeoLab of Utrecht University. These samples exhibited a certain mineral content of

which further chemical investigation was presumably valuable. Thin sections were carbon coated prior to analysis. A beam current of 20 nA and an acceleration voltage of 15 kV were used. Semi-quantitative preliminary analysis during the EPM sessions was performed with Energy Dispersive X-Ray Spectroscopy (EDS). Wavelength Dispersive X-Ray Spectroscopy (WDS) was used for quantitative chemical analysis.

#### **4.5. Geochronology**

To derive the age of KG1006, the rock sample was sent to the institute 'Overburden Drilling Management Limited' in Ottawa, Canada for mineral separation. Thereafter, 23 zircons were picked and mounted on a thin section. These zircons were polished until the internal structure was exposed. Cathodoluminescence (CL) analysis was carried with the same electron microprobe as the mineral chemistry analysis. Based on the CL images, the least altered spots were selected for LA-ICP MS analysis. Three zircons were too small for LA-ICP-MS analysis. Abundances of  $^{206}\text{Pb}$ ,  $^{207}\text{Pb}$ ,  $^{238}\text{U}$  and  $^{235}\text{U}$  were measured for the deduction of the zircon ages. The GLITTER software was used for processing the data. The measurement standard ZR91500 was used for calibration. For the larger zircons, a spot size of 30  $\mu\text{m}$  was used, 20  $\mu\text{m}$  was used for the smaller zircons. The laser operated with a pulse energy of 6.2  $\text{J}/\text{cm}^2$  and a repetition rate of 10 Hz. Pb and U isotope concentrations of KG1007 were measured in an earlier study by Jeroen Postema, with data processing conducted by Dr. Leo Kriegsman. The derivation of the geochronological age of KG1006 is left out of this report, for it was decided to exclude KG1006 from the Sara's Lust Gneisses (see Section 6.3.1.3. for further elaboration). The CL images of the zircons from KG1006 are reported in Appendix A.

#### **4.6. Perple\_X modelling**

The bulk rock chemistry in weight percentage of LB106A, LB106B and LE9 was used as input for Perple\_X modelling (version 6.6.9.) to compute pseudosections. Solution models were used for solid solution minerals. An overview of all the solution models used is depicted in Table 1. Additional mineral isopleths were computed, for both mineral abundances and mineral compositions. The mineral abundance isopleths were compared with petrographic observations, the mineral composition isopleths with EPM data. The results of the garnet-biotite geothermometer of Ferry and Spear (1978) were combined with the pseudosections and isopleths to infer the peak metamorphic conditions of the Sara's Lust Gneisses.



*Table 1 - Summary of all the solution models used in Perple\_X*

Mineral	Reference	Note
Biotite	Tajčmanová et al., 2009	Includes Tschermak substitution and Mn content
Chlorite	Holland et al., 1998	
Cordierite		Ideal
Clinoamphibole	Diener et al., 2007	
Clinopyroxene	Holland & Powell, 1996	
Garnet	Holland & Powell, 1998	
Melt	White et al., 2001	
Muscovite (white mica)	Holland & Powell, 1998	
Orthoamphibole	Diener et al., 2007	
Plagioclase	Newton et al., 1980	High structural state
K-feldspar	Waldbaum & Thompson, 1968	

## 5. Results

### 5.1. Petrography

Petrographic observations on mineral content and textures are summarised in a table per thin section (Table 2 - 17). Further, if metamorphism was recognised in the thin sections, a metamorphic facies was deduced. For each sample a table is provided with a summary of the petrographic observations. Preliminary interpretations are also given for the protolith (for metamorphosed rocks) or rock types (for unmetamorphosed rocks) based on petrographic observations supported with EPM data. The IUGS mineral abbreviations were used in the petrographic images (Siivola & Schmid, 2007). A more extensive protolith classification based on major and trace element geochemistry (and mineral content for the Streckeisen diagram (1967)) can be found in Section 5.2.

Table 2 - Summary of petrographic observations of JS1A. Percentages are estimated.

JS1A			
Mineral content	Percentage	Textures	Rock type
k-feldspar (microcline, orthoclase)	30	biotite is present in between felsic minerals	biotite granite
quartz	30	metamorphic textures are lacking	
biotite	25		
plagioclase	11	homogeneous distribution of minerals	
epidote	2		
magnetite	1	quartz and feldspar grains have a	
muscovite	1	heterogeneous grain size	
apatite	accessory		
monazite	accessory		
tourmaline	accessory		
zircon	accessory		
carbonate	secondary		

Sedimentary structures were not observed in the rock sample. Gneissic bands or other metamorphic textures were not present (Figure 7a, b). Biotite often formed around quartz and feldspar grains (Figure 7c). The main mineralogy comprises quartz, feldspars and biotite and minor epidote. Quartz and feldspar grains exhibit a heterogeneous grain size where fine-grained grains fill the spaces between coarser grains. Accessory minerals are apatite, monazite, tourmaline and zircon. Domains with a higher amount of felsic minerals were not macroscopically visible. Further, minerals are distributed homogeneously throughout the thin section.

The presence of homogeneously distributed minerals with finer grained minerals filling the matrix between coarser grains indicates a magmatic origin. The biotite in between coarser grained felsic minerals is interpreted as a magmatic feature. A substantial amount of quartz and feldspar crystallised out of the melt before biotite. Thereafter, biotite crystallised in between these grains to form the observed texture. Although this is in contradiction with the Bowen's series (Bowen, 1956), it is not unlikely. Magmas become fluid-enriched during fractional crystallization. As a result, the fluid-rich melts may crystallise hydrous phases such as biotite (and epidote) in between other already formed crystals. The minor carbonate observed is secondary due to the introduction of carbonate rich fluids. The different compositional domains were separately analysed with XRF (Table 18) and differed only little in silica content (dark bands (JS1A1) contained 66.20 wt% SiO<sub>2</sub> and white bands (JS1A2) contained 68.90 wt% SiO<sub>2</sub> ). For this reason, the more felsic domains are not interpreted as leucosomes as a result of migmatization, but merely as a result of compositional heterogeneity of the plutonic protolith.

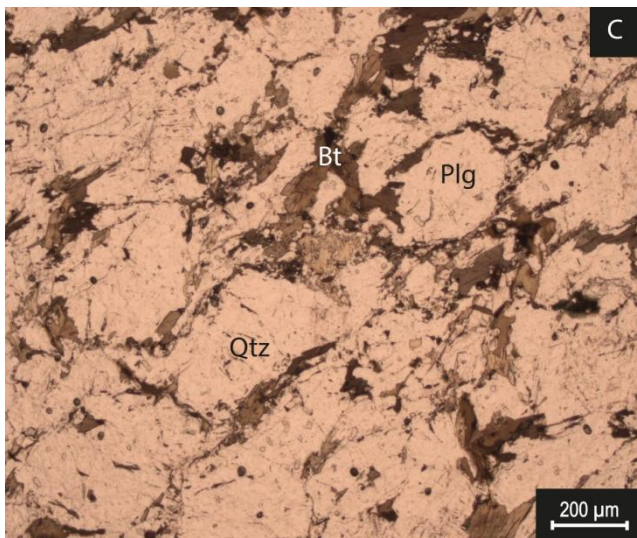
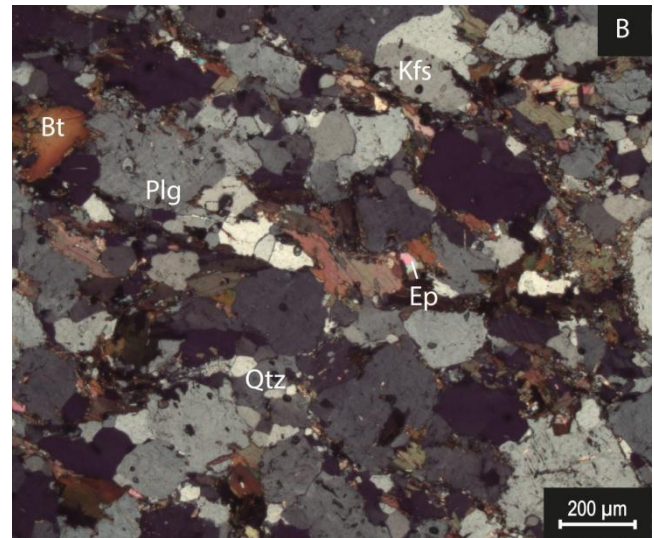
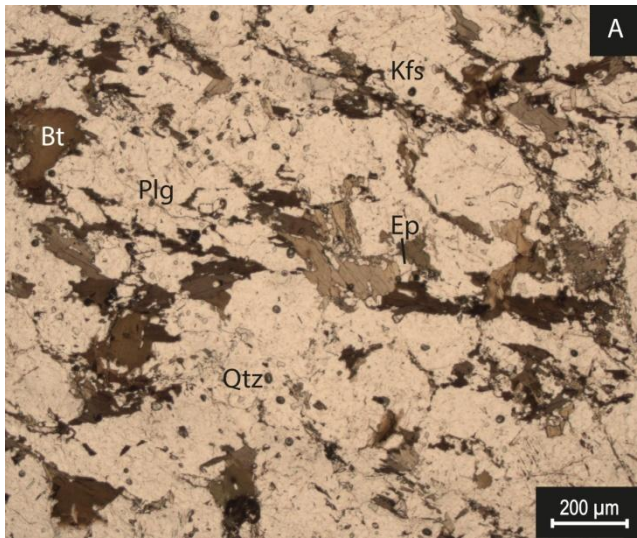


Figure 7 - Petrographic images of JS1A. a & b) An isotropic texture lacking a foliation, a in Plane Polarised Light (PPL), b in Crossed Polarised Light (XPL). c) Biotite crystallised in between feldspars and quartz in PPL.

Table 3 - Summary of petrographic observations of JS1B. Percentages are estimated.

<b>JS1B</b>			
<b>Mineral content</b>	<b>Percentage</b>	<b>Textures</b>	<b>Rock type</b>
quartz	36	bands with compositional differences and different grain size	granodiorite
biotite	25		
plagioclase	18	all phases exhibited a random orientation	
k-feldspar	10		
(microcline)			
hornblende	9	no metamorphic texture observed	
magnetite	1		
unknown mineral	1		
apatite	accessory		
epidote	accessory		
titanite	accessory		
tourmaline	accessory		
carbonate	secondary		

Compositional bands were observed with bands mainly composed of biotite and hornblende and more felsic bands consisting of quartz, feldspar (Figure 8a, b). All phases were found to have a random orientation. Other zones are very rich in biotite and quartz. Biotite is present in higher quantity compared to JS1A. This, and the presence of hornblende, indicates that JS1B is more mafic in composition than JS1A. Hornblende is partly converted into biotite. Moreover, biotite is dark coloured due to high titanium content. Further, a mineral was observed which could not be identified with the light microscope. It has the following characteristics: colourless, high relief and high birefringence colours. It might be a colourless pyroxene, but for a convincing identification chemical analysis of this particular mineral is necessary. In the more quartzo-feldspathic domains biotite is mainly present around quartz and feldspar grains (Figure 8c, d). Beside the main mineralogy, tourmaline, epidote, titanite and apatite were found to be present as accessory minerals. Carbonate is present as a secondary phase in low quantity. Metamorphic textures were not observed.

Similarly to JS1A, biotite around felsic minerals is interpreted as the consequence of biotite crystallising out of the melt at a late stage. Therefore, the protolith is interpreted as plutonic. Because all phases exhibited a random orientation, the banding is probably not due to deformation. Rather, the bands are interpreted as a magmatic texture. The compositional bands are not thought to be a metamorphic feature as felsic plutonic rocks are stable until melting temperatures are reached during metamorphism. Rather, the alternation of more felsic and mafic bands can represent igneous layering in the magma chamber. Furthermore, the conversion of hornblende to biotite is likely to be retrograde.

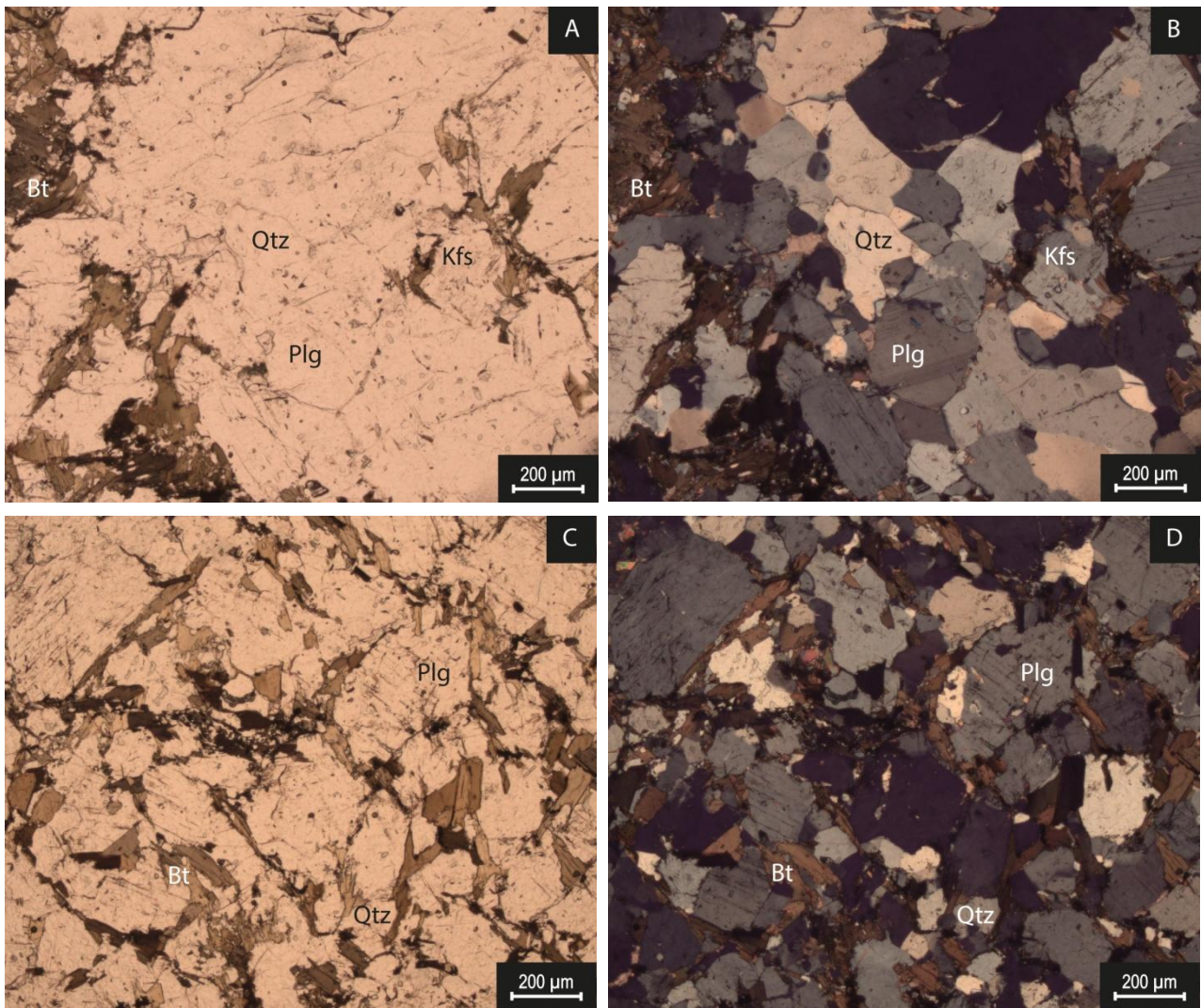


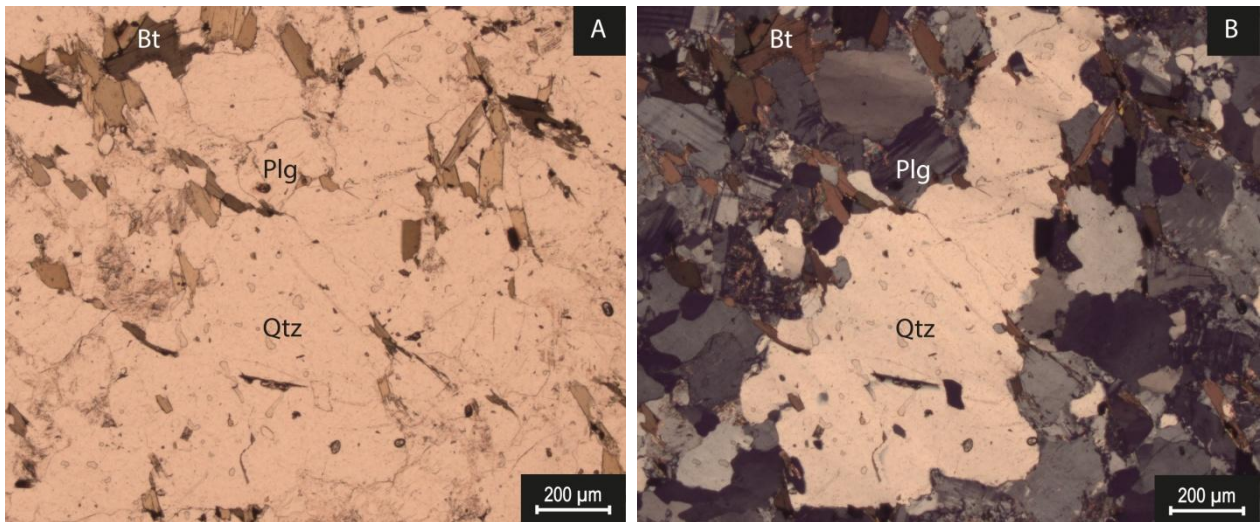
Figure 8 - Petrographic images of JS1B. a & b) Zone which almost entirely consists of feldspars and quartz, a in PPL, b in XPL. c & d) Biotite mainly in between feldspar and quartz grains, c in PPL, d in XPL.

Table 4 - Summary of petrographic observations of JS2A. Percentages are estimated.

<b>JS2A</b>			
<b>Mineral content</b>	<b>Percentage</b>	<b>Textures</b>	<b>Rock type</b>
plagioclase	37	some biotite grains show a weak certain	biotite granite
quartz	28	foliation	
biotite	20		
k-feldspar (microcline)	15	phaneritic texture	
muscovite	accessory		
magnetite	accessory		
zircon	accessory		

JS2A was found to mainly consist of plagioclase, quartz, biotite and k-feldspar. A substantial part of the biotite crystals display a preferable orientation, however this alignment is not dominantly present. Muscovite is exclusively present at the grain boundaries of biotite grains. Areas are present where biotite is completely absent. These biotite-absent areas are present as patches instead of alternating layers. Zircon and magnetite are present as an accessory mineral. Fairly large (up to 4 mm) quartz ribbons are present containing biotite and feldspar inclusions (Figure 9a, b). Moreover, the grain boundaries of these quartz ribbons are irregular. A clear gneissic layering other metamorphic textures are not found.

As muscovite is solely present around biotite grains, it is implied that muscovite formed as an alteration product of biotite. Further, the absence of metamorphic textures indicates that JS2A did not undergo much mineralogical change during prograde metamorphism. As a result, a metamorphic facies has not been derived. This is, again, explained by the felsic composition. Consequently, the weak foliation is expected to be a property of the protolith. JS2A exhibits a non-metamorphic phaneritic texture. Therefore, the protolith was interpreted as plutonic. Further, the large quartz ribbons observed indicate that quartz crystallisation occurred. This can be either due to an increase of stress as a result of retrograde deformation or during prograde metamorphism as a result of increasing temperature.



*Figure 9 - Petrographic images of JS2A. Large quartz ribbon with biotite and feldspar inclusions, a in PPL, b in XPL.*

Table 5 - Summary of petrographic observations of JS2B. Percentages are estimated.

<b>JS2B</b>			
<b>Mineral content</b>	<b>Percentage</b>	<b>Textures</b>	<b>Rock type</b>
quartz	35	bands of biotite enclosing quartz and	granodiorite
biotite	25	feldspar grains	
plagioclase	22		
hornblende	8	biotite and quartz intergrowth	
k-feldspar	8		
(microcline)		myrmekite texture in k-feldspar grain	
epidote	2		
magnetite	accessory	crystals are randomly orientated	
apatite	accessory		
rutile	accessory	phaneritic texture	
titanite	accessory		
tourmaline	accessory		
zircon	accessory		

JS2B was found to mainly consists of quartz, biotite, plagioclase, k-feldspar and hornblende. Biotite is, based on its colour, rich in iron and titanium and is sometimes chloritised and to a lesser extent altered to muscovite. Epidote is, compared to other samples, present in relatively high amounts. Titanium-rich phases are present as accessory minerals. Other accessory minerals are zircon, tourmaline and apatite. Similar textures are observed as in JS1A: quartz and feldspar grains entirely enclosed by biotite. Myrmekite textures in a microcline crystal intergrown with quartz (Figure 10a). Further, intergrowths of partly chloritised biotite and quartz are present (Figure 10b).

Randomly orientated crystals in a phaneritic texture indicate a plutonic protolith. In addition, the myrmekite textures present in a microcline crystal also strongly imply a plutonic petrogenesis. Biotite crystallised in between quartz and feldspar grains. This texture is interpreted as a result of the late magmatic crystallisation of biotite. The intergrowths of biotite and quartz could possibly represent remnants of pyroxene. Granitic magmas tend to erase their own mafic mineral content (Stevens, 2018). As a result, pyroxene may have reacted with the melt to form biotite and quartz during magmatic crystallisation. Subsequently, the remnants of pyroxene reacted with magmatic (or other) fluids to form chlorite. Following this reasoning, the protolith was more mafic than is displayed in the current mineral content. Chemical analysis on these intergrowths will give the chemistry of these chlorite and biotite grains to subsequently determine if these are the remnants of pyroxene. If these intergrowths indeed were pyroxenes, it would imply that this felsic plutonic rock crystallised out a fairly dry melt as pyroxene formed instead of hydrous biotite.



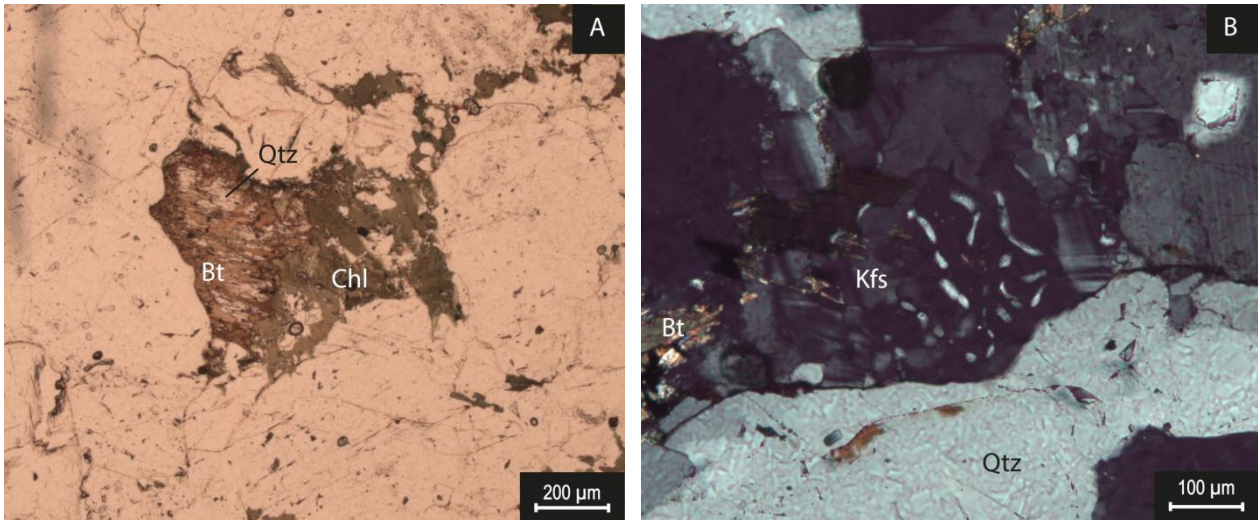


Figure 10 - Petrographic images of JS2B. a) Intergrowth of quartz and partly chloritised biotite, possibly a remnant of pyroxene, in PPL. b) Myrmekite texture in a k-feldspar grain, in XPL.

Table 6 - Summary of petrographic observations of KG1006. Percentages are estimated.

KG1006			
Mineral content	Percentage	Texture	Rock type
quartz	49	no metamorphic foliation present	felsic plutonic
plagioclase	25	phaneritic texture	
biotite	14		
k-feldspar (microcline)	12		
apatite	accessory		
magnetite	accessory		
monazite	accessory		
zircon	accessory		

KG1006 was found to consist predominantly of quartz. In addition, plagioclase, biotite and K-feldspar are present. Metamorphic textures and minerals are not present. Apatite, monazite and zircon are found as accessory minerals. The texture of KG1006 is phaneritic (Figure 11a, b).

Because KG1006 is phaneritic but metamorphic indicators lack, the rock is assumed to be felsic plutonic. This also explains why KG1006 does not exhibit metamorphic minerals.

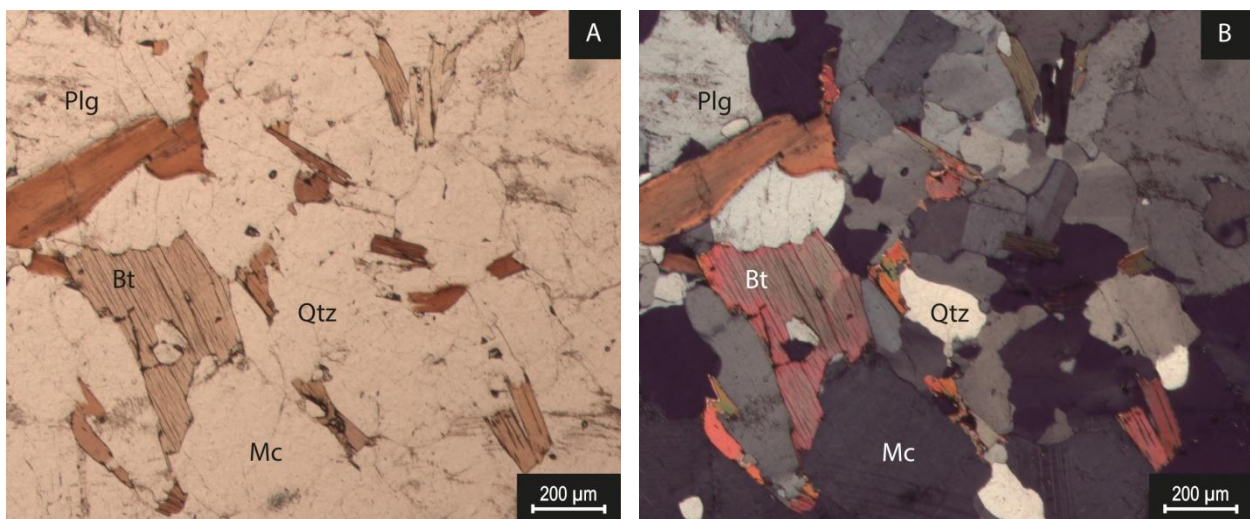


Figure 11 - Petrographic images of KG1006. No foliation is present, a in PPL, b in XPL.

Table 7 - Summary of petrographic observations of KG1007. Percentages are estimated.

KG1007			
Mineral content	Percentage	Texture	Rock type
quartz	34	no metamorphic foliation	felsic plutonic
biotite	30		
plagioclase	21	phaneritic texture	
k-feldspar (microcline, orthoclase)	10		
hornblende	3		
muscovite	1		
magnetite	1		
titanite	accessory		
zircon	accessory		
carbonate	secondary		

Muscovite is solely present around biotite grains. KG1007 yields a higher quantity in hornblende and biotite compared to KG1006. Moreover, a large titanite grain is present (Figure 12a, b). Further, biotite is slightly greener compared to the biotite in KG1006, likely due to a higher iron content. Aside these observations, KG1006 and KG1007 were found to be very similar.

As muscovite is only present around biotite grains, it is expected that biotite altered to muscovite during retrogradation. For the same reasons as KG1006, a plutonic protolith is suggested for KG1007, but with a slightly more mafic composition.

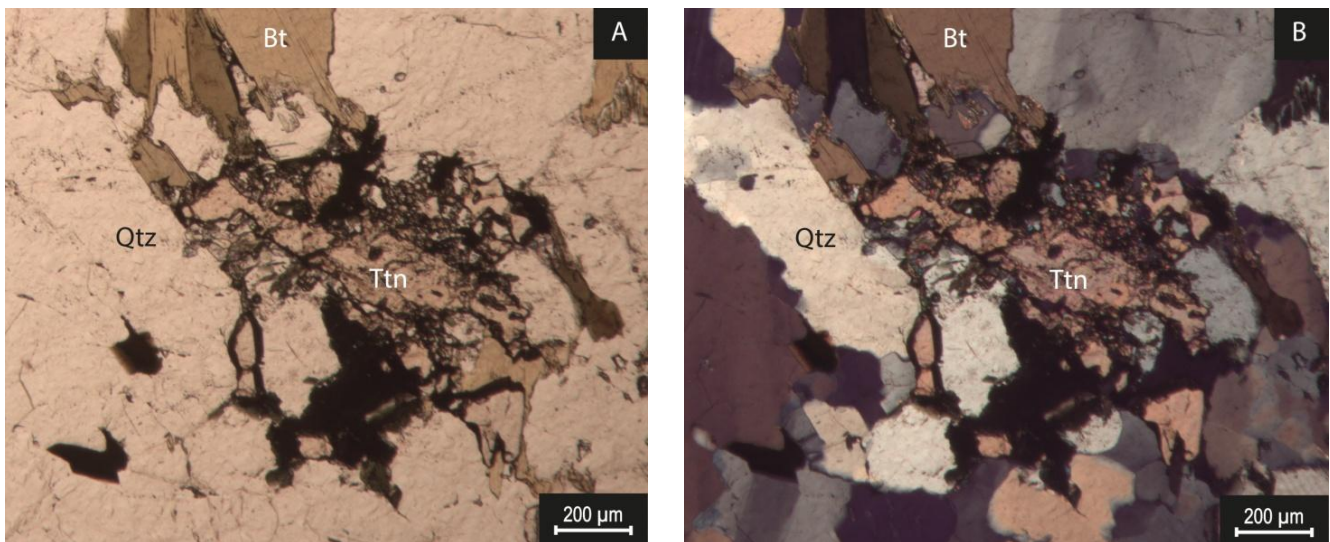


Figure 12 - Petrographic images of KG1007. Large titanite grain, a in PPL, b in XPL.

Table 8 - Summary of petrographic observations of LB106A. Percentages are estimated.

<b>LB106A</b>					
<b>Mineral content</b>	<b>Percentage</b>	<b>Texture</b>	<b>Protolith</b>	<b>Metamorphic facies</b>	<b>Rock type</b>
plagioclase	40	compositional	volcano-	amphibolite	biotite-garnet gneiss
biotite	30	bands with	sedimentary		
quartz	21	magnetite-rich			
garnet	5	bands and			
ilmenite	3	(chloritised)			
magnetite	2	biotite-rich bands			
anthophyllite	2				
apatite	accessory	small shear zones			
zircon	accessory	are present			

LB106A was found to display compositional gneissic bands. This gneissic layering is mainly expressed by biotite grains aligned along a preferred orientation. Further, WDS analysis on the opaques evidences the presence of both ilmenite and magnetite. Bands with larger amounts of magnetite and bands almost entirely composed of quartz are also present. The main mineral assemblage comprises plagioclase, biotite, quartz and garnet. Biotite is, based on its light colour, poor in titanium and is sporadically altered to chlorite. Sometimes, plagioclase grains have biotite rims (Figure 13a, b). As biotite and garnet are both present in the same stable assemblage, geothermometry is possible with LB106A. Further, the garnets are subhedral and surrounded by predominantly plagioclase and quartz. One colourless mineral with high relief and low birefringence colours could not be identified with petrographic research. It has the following optical properties: high relief, colourless, low birefringence colours and anhedral crystal shape, yet it seems that it shows a blocky crystal habit (Figure 13c, d). This specific mineral was analysed with WDS and turned out to be anthophyllite. Biotite was found to be locally intergrown with anthophyllite.

The presence of shear zones indicates that LB106A underwent deformation. Minerals close to the shear zones are still sheared and have not recrystallised. Hence, deformation must have taken place after metamorphism and during exhumation. Further, the metamorphic formation of anthophyllite is likely associated with hydrothermal alteration of volcanic rocks prior to metamorphism. Schumacher (1988) argued that alteration of volcanic rocks especially by seawater causes the deviating chemical composition that subsequently led to the metamorphic growth of anthophyllite. The intergrown anthophyllite and biotite evidence that they crystallised coevally, implying that they are stable together. This plagioclase-biotite-garnet gneiss likely underwent metamorphism at amphibolites facies conditions.

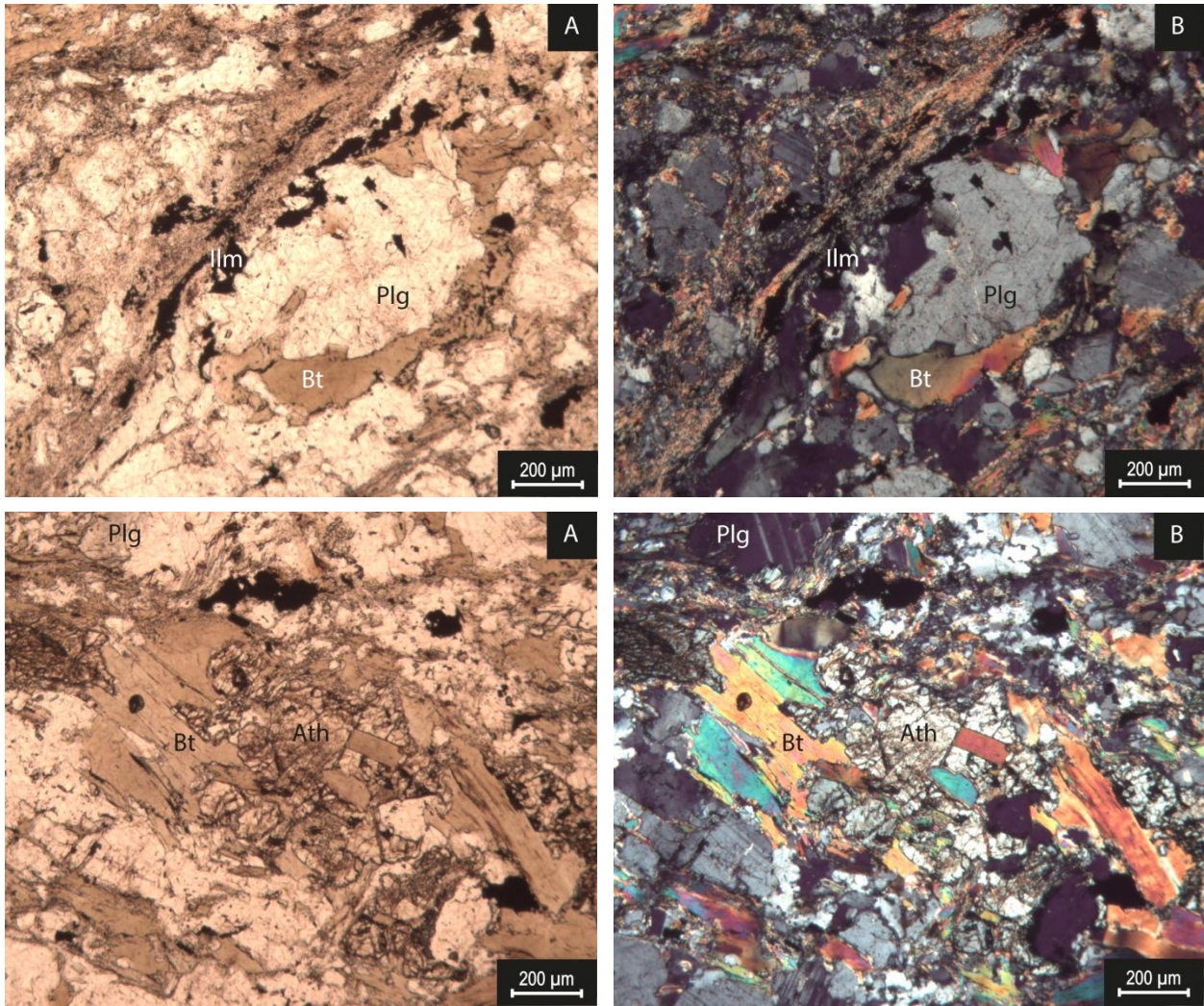


Figure 13 - Petrographic images of LB106A. a & b) Plagioclase grain with biotite around it, a in PPL, b in XPL. c & d) Anthophyllite intergrown with biotite, c in PPL, d in XPL.

Table 9 - Summary of petrographic observations of LB106B. Percentages are estimated.

<b>LB106B</b>						
<b>Mineral content</b>	<b>Percentage</b>		<b>Texture</b>	<b>Protolith</b>	<b>Metamorphic facies</b>	<b>Rock type</b>
	<b>1:</b>	<b>2:</b>				
quartz	36	32	small scaled	volcano-	amphibolite	biotite-garnet
plagioclase	33	40	shear zones are	sedimentary		gneiss (1) and
biotite	23	4	present			anthophyllite-
garnet	3	-				bearing
anthophyllite	1	20	minerals are			gneiss (2)
ilmenite	1	1	predominantly			
magnetite	1	2	homogeneously			
chlorite	1	1	distributed			
tourmaline	1	-				
monazite	accessory		gneissic bands			
titanite	accessory		are absent			
carbonate	secondary					

Two main lithologies were found to be present in LB106B: 1) quartz, plagioclase, biotite, garnet (Figure 14a, b) and 2) quartz, feldspars and orthoamphibole (Figure 14c, d). The latter yields the following optical properties upon which it is classified as orthoamphibole: two sets of cleavages with intersecting angles of  $120^\circ$  and  $60^\circ$ , moderate to high relief, colourless in PPL, straight extinction and low to moderate birefringence colours. This phase is chemically analysed with WDS and is anthophyllite. Anthophyllite is in lesser extent present in the garnet-bearing lithology and looks altered. Moreover, garnet and anthophyllite do not share grain boundaries. Therefore, it is suggested that these do not belong to the same stable assemblage. Conversely, garnet is stable with biotite. This makes geothermometry applicable to LB106B. EPM analysis on biotite and garnet chemistry is required to investigate their chemical composition for geothermometry. Further, biotite, magnetite and ilmenite are enriched in some bands. An evident gneissic banding lacks because anthophyllite crystals are clearly randomly distributed instead of aligned along a certain foliation. Garnet grains have an anhedral shape. One tourmaline crystal of  $\sim 1$  mm length is present in lithology 1 (Figure 14e, f). Accessory minerals are monazite and titanite. Anthophyllite is sometimes replaced by light coloured chlorite.

Local differences in chemical composition due to a certain layering explains the presence of different metamorphic mineral assemblages. The compositional bands are assumed to be a feature of the protolith for a gneissic banding is absent. Different lithologies are present due to compositional differences in the protolith. The presence of anthophyllite indicates a volcanic protolith. Further, the presence of tourmaline may indicate influx of boron-rich fluids during metasomatic alteration.

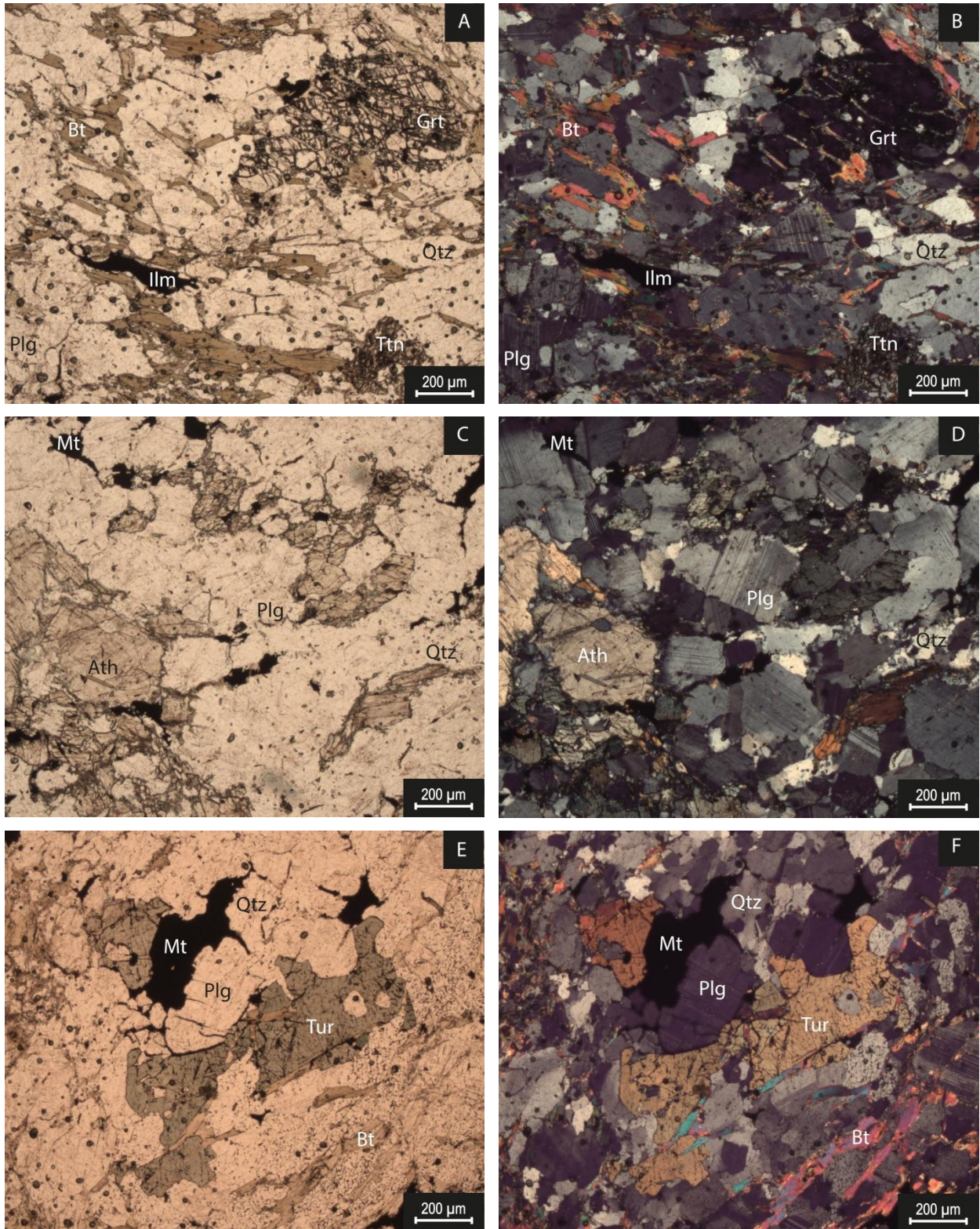


Figure 14 - Petrographic images of LB106B. a & b) Lithology 1, composed of mainly quartz, feldspar, biotite and garnet, a in PPL, b in XPL. c & d) Lithology 2, composed of mainly quartz, feldspar and anthophyllite, c in PPL, d in XPL. e & f) Large tourmaline crystal, e in PPL, f in XPL..

Table 10 - Summary of petrographic observations of LB107A. Percentages are estimated.

<b>LB107A</b>					
<b>Mineral content</b>	<b>Percentage</b>	<b>Texture</b>	<b>Protolith</b>	<b>Metamorphic facies</b>	<b>Rock type</b>
hornblende	35	some bands enriched in		amphibolite	hornblende-
plagioclase	34	biotite, in hornblende			rich gneiss
k-feldspar (microcline)	8	plus biotite, or in quartz			
biotite	10	feldspars and quartz			
quartz	10	exhibit heterogeneous			
ilmenite	2	grain sizes			
magnetite	1				
apatite	accessory	gneissic banding lacks			
titanite	accessory				

LB107A was found to be mainly composed of hornblende, plagioclase, k-feldspar, biotite and quartz. Hornblendes often contain biotite inclusions. Compositional bands are present, with bands mainly composed of hornblende, biotite, or felsic minerals (Figure 15a, b). Hornblende often contain rims enriched in magnetite. The grain size within the compositional bands is heterogeneous, with finer grains mainly being present around coarser grains (Figure 15c, d). Further, LB107A does not display any indication of prograde metamorphic textures.

Primary compositional layers are maintained despite the metamorphic overprint. As a result, some bands are strongly enriched in biotite, in hornblende plus biotite, or in quartz. These could either be explained by igneous layering within a magma chamber or by compositional layers in a volcano-sedimentary rock. The heterogeneous grain size may favour a volcano-sedimentary origin. However, it is thought that the majority of the minerals are metamorphic. Consequently, a heterogeneous grain size does not necessarily give implications on the petrogenesis of the protolith. In addition, it seems that the contact zones between grains show evidence for grain size reduction, a texture often referred to as 'mortar texture'. It indicates mylonitisation under relatively high differential stress and low temperature. Therefore, these heterogeneous grain sizes are likely the result of deformation. Further, biotite inclusions in hornblende are interpreted as a result of growth of hornblende during to prograde metamorphism and possibly indicates the melting reaction 'Bt + Qtz + Plg → Hbl + melt'. The primary textures of the protolith are assumed to have been erased by the metamorphic overprint such that the petrogenesis of the protolith could not be recognised from petrography. The rimmed hornblendes are interpreted as retrograde release of iron.



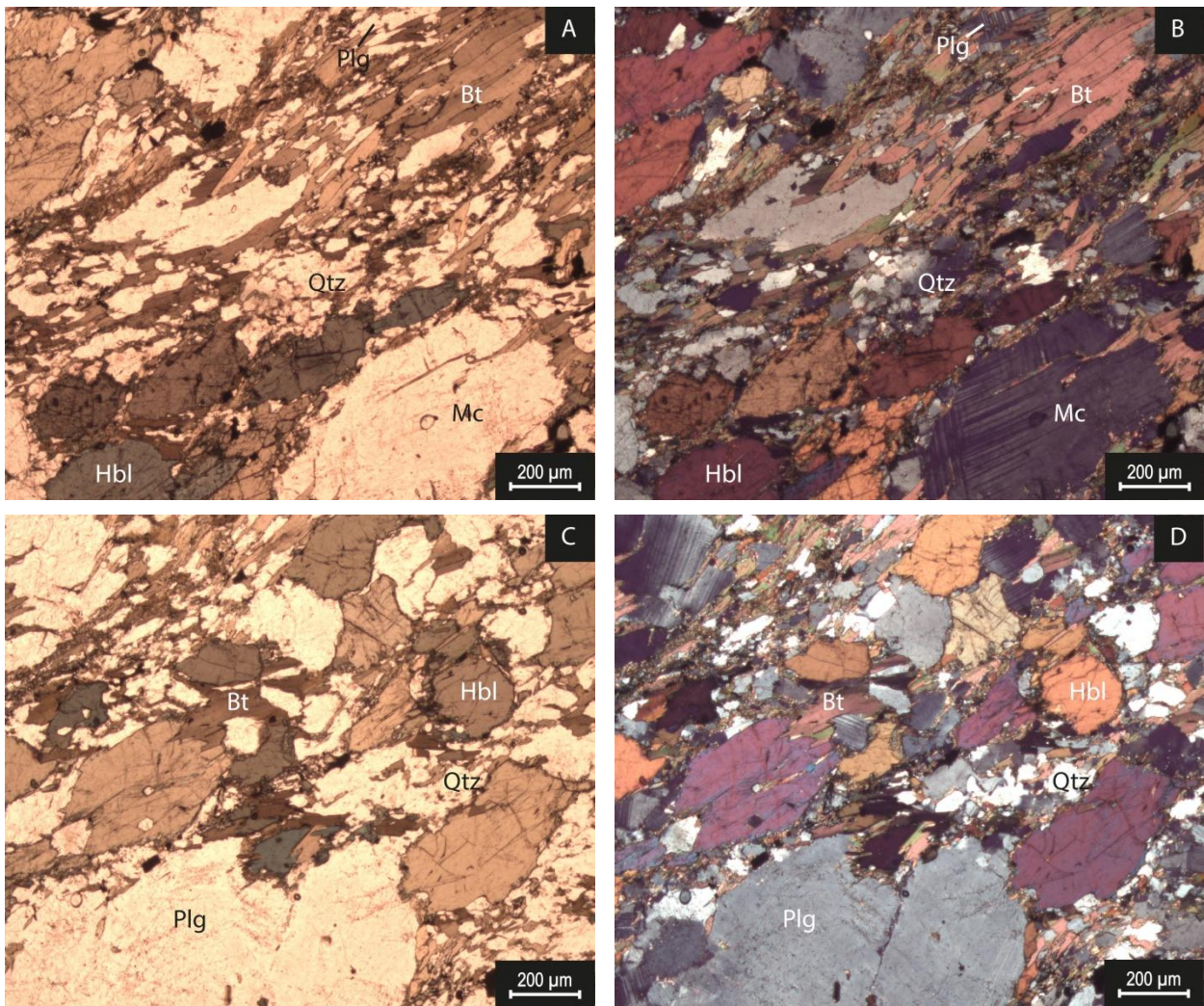


*Figure 15 - Petrographic images of LB107A. a & b) Bands mainly composed of biotite and bands mainly composed of hornblende, a in PPL, b in XPL. c & d) Quartz and feldspars exhibit heterogeneous grain sizes where finer grains are around coarser grains, c in PPL, d in XPL.*

Table 11 - Summary of petrographic observations of LB107B. Percentages are estimated.

<b>LB107B</b>					
<b>Mineral content</b>	<b>Percentage</b>	<b>Texture</b>	<b>Protolith</b>	<b>Metamorphic facies</b>	<b>Rock type</b>
hornblende	40	compositional bands,	?	amphibolite	amphibolite
plagioclase	32	bands enriched in			
quartz	12	biotite or hornblende			
k-feldspar	7				
(microcline, orthoclase)		bands with larger and smaller grains			
biotite	5				
ilmenite	3	hornblendes are weakly			
magnetite	1	aligned			
apatite	accessory				
titanite	accessory				

LB107B was found to chiefly be composed of hornblende and plagioclase. Biotite, k-feldspar, quartz, ilmenite and magnetite are present in lesser extent. A metamorphic foliation lacks. Apatite and titanite are accessory. Grain size is heterogeneous in the majority of LB107B. Hornblendes are somewhat aligned, yet a gneissic banding is absent (Figure 16a, b). The overgrowth of metamorphic hornblende and plagioclase eliminated the textures of the protolith. Nevertheless, compositional bands are present.

The compositional bands are assumed to be a property of the protolith. These can be both explained by magmatic and (volcano-)sedimentary processes. As a consequence, the petrogenesis of the protolith could not be derived with petrography alone. The weak alignment of hornblendes are likely caused by deformation which resulted in the preferable growth direction of the crystals. Based on metamorphic mineral content and only a weak alignment of minerals, LB107B is classified as an amphibolite.

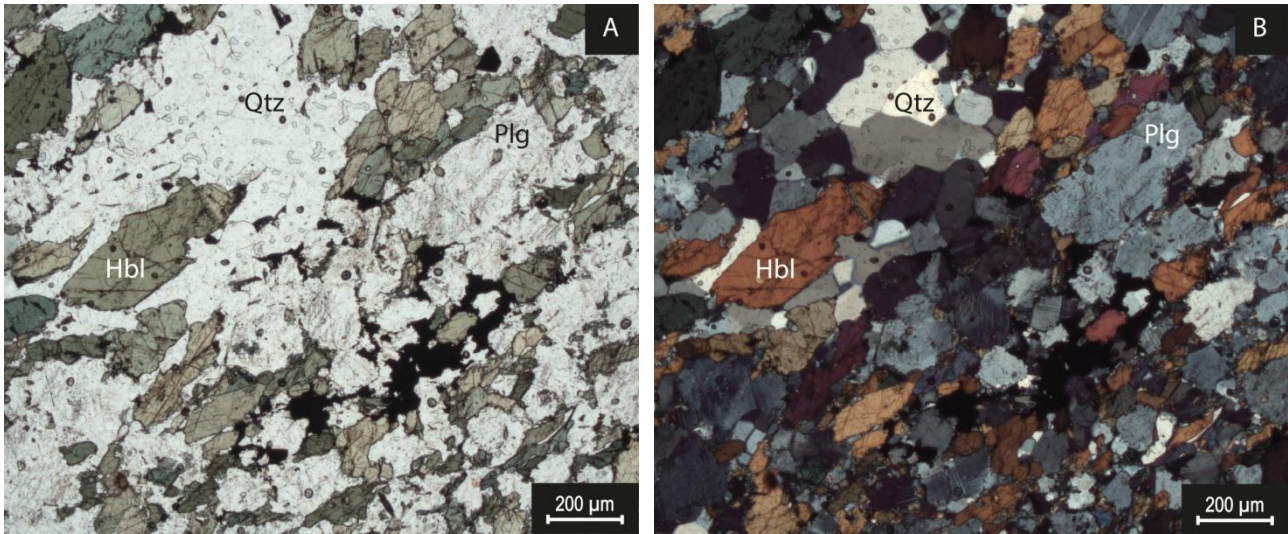


Figure 16 - Petrographic images of LB107B. Minerals are somewhat aligned and exhibit varying grain sizes, a in PPL, b in XPL.

Table 12 - Summary of petrographic observations of LB108A. Percentages are estimated.

LB108A			
Mineral content	Percentage	Texture	Rock type
quartz	57	weak gneissic banding	weakly deformed biotite granite
biotite	16		
plagioclase	10	biotite often around quartz and feldspar grains	
k-feldspar	8		
(microcline)	3	shear zones are present	
ilmenite	3		
amphibole	1		
magnetite	1		
epidote	accessory		
apatite	accessory		
titanite	accessory		
zircon	accessory		
carbonate	secondary		

In LB108A bands of biotite were found to be present, where biotite is sporadically altered to chlorite. Quartz, of which LB108A mainly consists, also shows a slight foliation. This foliation looks like a gneissic foliation. Within some biotite grains, remnants of a green mineral are found, which is likely an amphibole, either actinolite or hornblende. Further, biotite is often found around quartz and feldspar grains. Feldspars are less abundant compared to other samples. Apatite, zircon and titanite are present as accessory minerals and some minor carbonate is present as a secondary phase. Small shear zones are present throughout the thin section (Figure 17a, b).

The growth of biotite around felsic minerals can, again, be explained by a late biotite crystallisation in a magma chamber. Hence, a plutonic protolith is suggested. Carbonates are assumed to be present as a secondary mineral.

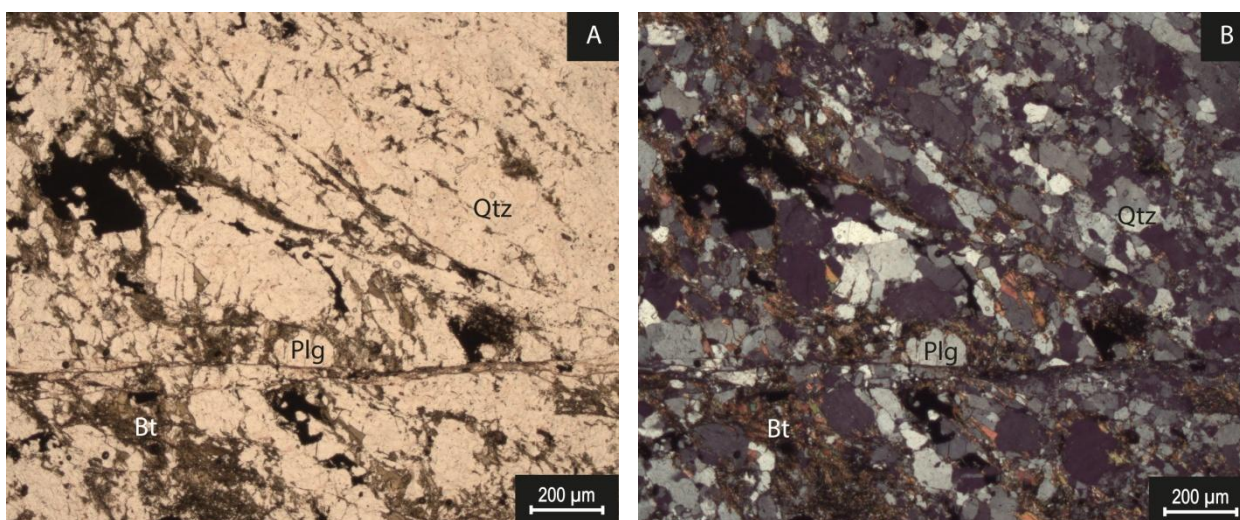


Figure 17 - Petrographic images of LB108A. Small scale shear zones are present, a in PPL, b in XPL.

Table 13 - Summary of petrographic observations of LB108B. Percentages are estimated.

<b>LB108B</b>			
<b>Mineral content</b>	<b>Percentage</b>	<b>Texture</b>	<b>Rock type</b>
quartz	40	small grained shear zones	cataclastic biotite
plagioclase	22		granite
biotite	20	gneissic bands do not seem to be	
k-feldspar (microcline, orthoclase)	10	present	
secondary opaques	6	biotite chiefly present around	
magnetite	2	quartz and feldspars	
actinolite	2		
muscovite	1	bands with more quartz and more	
apatite	accessory	biotite present	
zircon	accessory		
carbonate	secondary		

LB108B was found to be very similar to LB108A. Aside the similarities, LB108B looks slightly more deformed. Shear zones are abundantly present and some grains are fractured. Within these shear zones opaques and carbonates are present (Figure 18a, b). Biotite grains mainly grew around quartz and feldspars. Actinolite is present, but often substantially converted to biotite. Muscovite is solely present on the grain boundaries of biotite grains. Apatite and zircon are accessory.

Muscovite is assumed to be the alteration product of biotite. LB108B is, based on the same grounds as LB108A, also assumed to be a felsic plutonic rock. Shear zones are present in higher quantities compared to other samples, indicating that LB108B underwent higher-grade deformation. During deformation, the introduction of fluids may have caused the crystallisation of opaques and carbonates in the micro shear zones. The secondary opaques could not be identified because crystal habits lack.

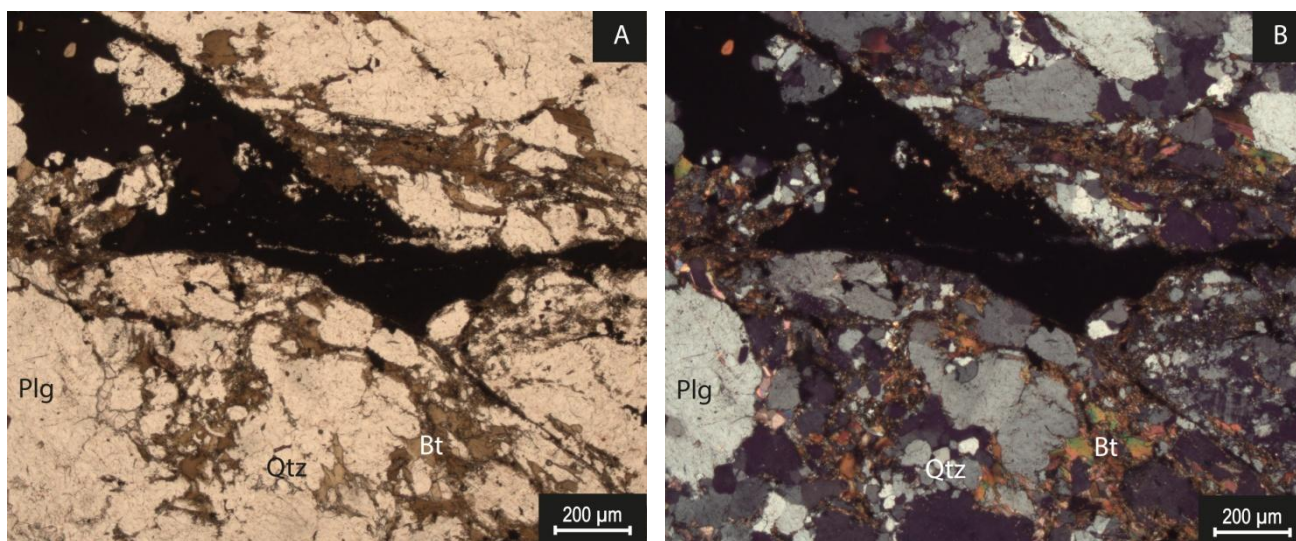


Figure 18 - Petrographic images of LB108B. Shear zone with secondary carbonates and opaque phases.

Table 14 - Summary of petrographic observations of LB109A. Percentages are estimated.

<b>LB109A</b>					
<b>Mineral content</b>	<b>Percentage</b>	<b>Texture</b>	<b>Protolith</b>	<b>Metamorphic facies</b>	<b>Rock type</b>
actinolite	35	schistosity visible, with quartz plus feldspar bands and actinolite plus cummingtonite bands  other zones displays random orientation of minerals  quartz shows heterogeneous grain size  ophitic textures in actinolites  shear zones are present	mafic	amphibolite	Amphibole-rich-schist
quartz	25		plutonic		
cummingtonite	15				
plagioclase	14				
biotite	10				
k-feldspar	2				
(microcline)					
magnetite	1				
apatite	accessory				
zircon	accessory				

LB109A was found to mainly consist of amphiboles, namely actinolite and cummingtonite. Cummingtonite is an amphibole with high iron and magnesium. As a consequence, the protolith needed to be rich in iron and magnesium. Apatite and zircon are present as accessory mineral. Compositional bands of biotite and amphiboles alternated with quartz- and feldspar-rich bands are present. Ophitic textures are present with actinolite enclosing plagioclase crystals (Figure 19a, b). Cummingtonite and actinolite are found sharing grain boundaries and are therefore stable together (Figure 19c, d). Further, actinolite and biotite are sometimes intergrown (Figure 19e, f). Small shear zones are present throughout the thin section. Some amphibole is replaced by epidote and biotite is often altered to chlorite, both likely during retrogradation. Texturally, some domains exhibit a clear schistosity, whilst other domains contain randomly orientated crystals.

Shear zones are the consequence of ductile deformation during exhumation. The intergrowth of biotite and actinolite suggest coeval crystallisation during prograde metamorphism. Ophitic textures are formed in intrusions, implying that the protolith of LB109A was plutonic. Thence, the compositional bands of alternating biotite-amphibole and quartz-feldspar are assumed to be the result of igneous layering in a magma chamber. Possibly, the locally present schistosity texture indicates localised deformation.

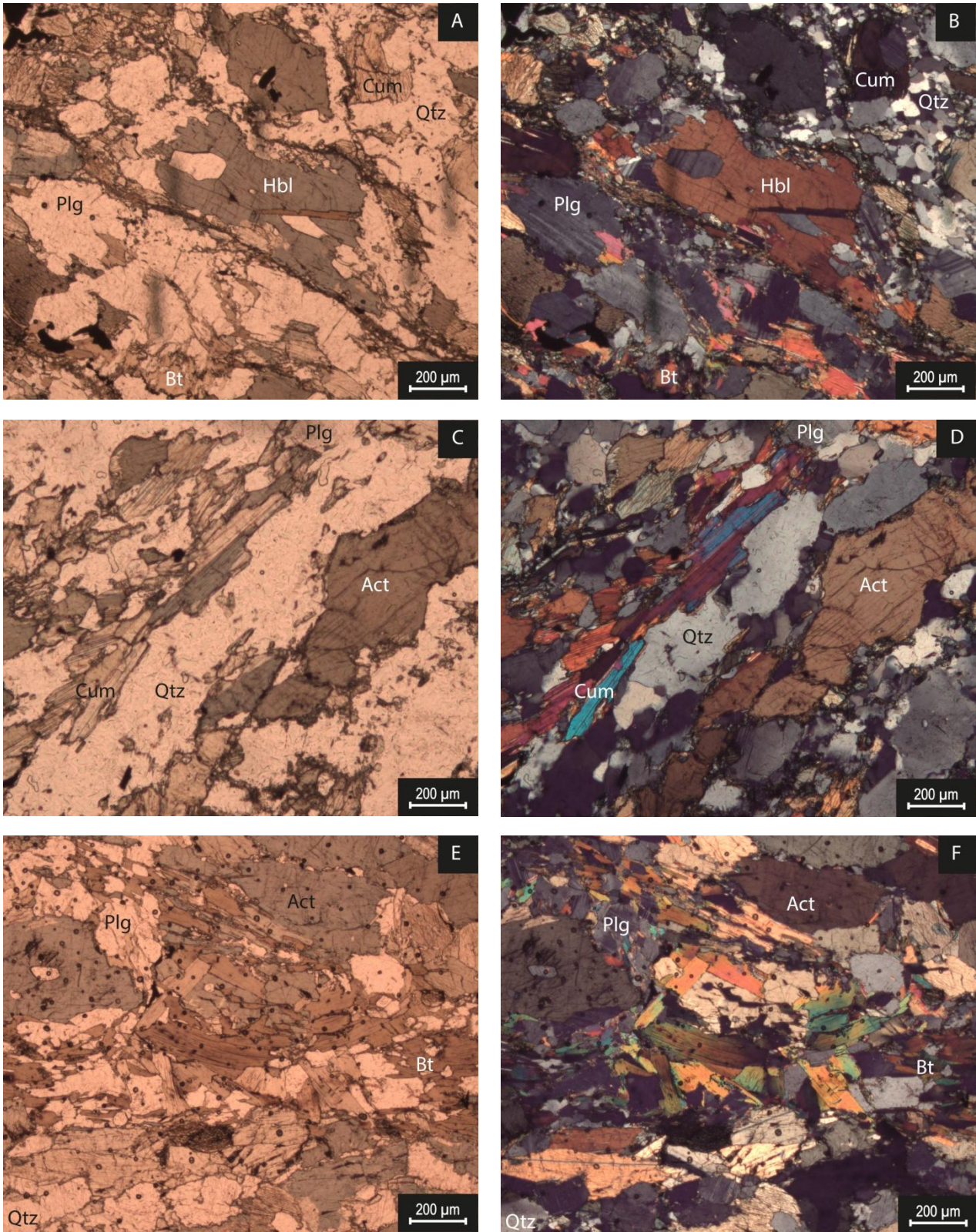


Figure 19 - Petrographic images of LB109A. a & b) Ophitic textures with actinolite enclosing plagioclase crystals, a in PPL, b in XPL. c & d) Cummingtonite is present adjacent to actinolite, c in PPL, d in XPL. e & f) Biotite and actinolite are intergrown, e in PPL, f in XPL.

Table 15 - Summary of petrographic observations of LB109B. Percentages are estimated.

<b>LB109B</b>					
<b>Mineral content</b>	<b>Percentage</b>	<b>Texture</b>	<b>Protolith</b>	<b>Metamorphic facies</b>	<b>Rock type</b>
feldspars & quartz	30	mylonitic texture	mafic volcanic / mafic plutonic	-	blastomylonite
actinolite	25	biotite-rich and biotite-poor layers are present			
micas (biotite)	25				
chlorite	15				
magnetite	3				
ilmenite	2				
zircon	accessory				

Two compositional domains were found to be present: 1) quartz- and feldspar-rich domains, and 2) biotite-rich areas. Further, LB109B is strongly sheared (Figure 19a, b). Actinolite grains clearly show a foliation which is also followed by aligned micas. These micas are likely mainly biotite and have not grown to large flakes. Instead, these are present as fine grained phases in between actinolite and quartz and feldspar grains. Actinolite is often altered to biotite and chlorite. As a result of the high degree of shear, quartz and feldspars are not easily distinguished for they all show similar zoning patterns.

LB109B is strongly mylonitised, indicating shear deformation. Because actinolite is abundant, it is suggested that the protolith of LB109B was magmatic. The introduction of fluids during shearing could have provided alkalis for the alteration of actinolite to micas. Two theories are suggested for the different compositional domains: either these compositional bands were already present in the protolith, or these domains underwent different intensities of fluid interactions resulting in more and less alteration to micas and chlorite. As mainly retrograde minerals are present, a peak metamorphic facies could not be inferred.



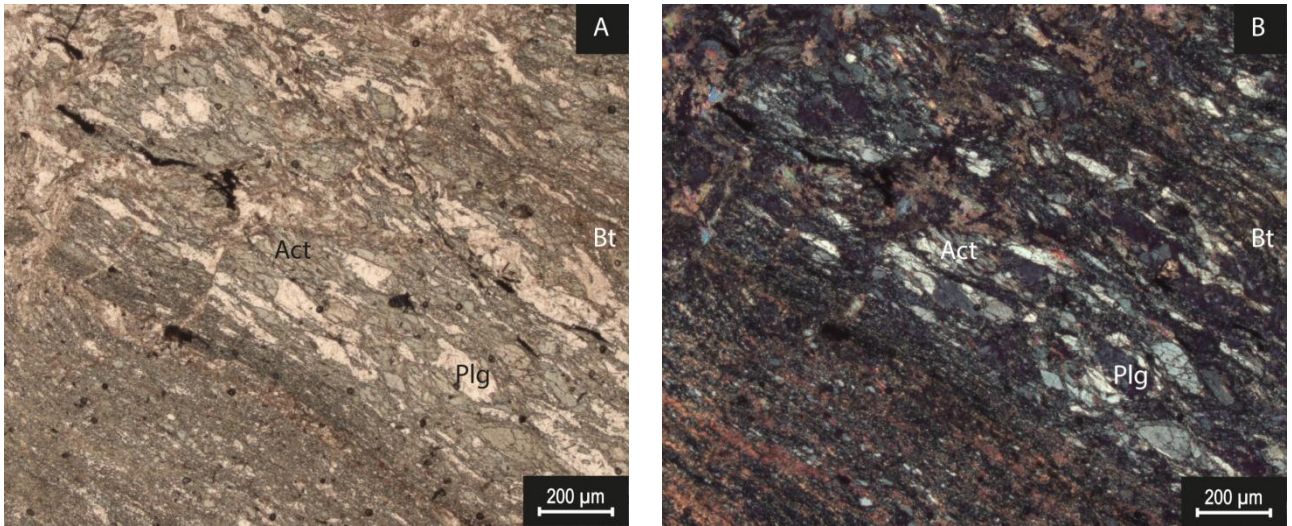


*Figure 19 - Petrographic images of LBI09B. Mylonitic texture is present, a in PPL, b in XPL.*

Table 16 - Summary of petrographic observations of LE8. Percentages are estimated.

LE8					
Mineral content	Percentage	Texture	Protolith	Metamorphic facies	Rock type
quartz	40	biotite is present in a preferred orientation	sedimentary	-	biotite-gneiss
biotite	30				
plagioclase	23	elongate quartz ribbons follow the same foliation as biotite			
magnetite	5				
muscovite	2				
apatite	accessory				
tourmaline	accessory				
zircon	accessory				

The main mineralogy of LE8 was found to consist of quartz, plagioclase and biotite. Large elongate quartz ribbons are present. The quartz ribbons are aligned along a certain foliation. This foliation is also observed in the preferred biotite orientation (Figure 20a, b). Further, biotite has a dark colour due to high titanium content.

The protolith is considered to be sedimentary because: 1) the texture of the drill core looks, similarly to the texture of LE9, somewhat sedimentary, and, 2) LE8 chiefly consists of quartz and micas. Quartz ribbons have formed due to quartz recrystallisation, likely by grain boundary migration. Further, the strong foliation present in LE8 is thought to be gneissic. Iron loss from biotite is likely during retrograde process. Deducing a metamorphic facies was not possible because the mineral assemblage is not characteristic for certain pressure and temperature conditions.

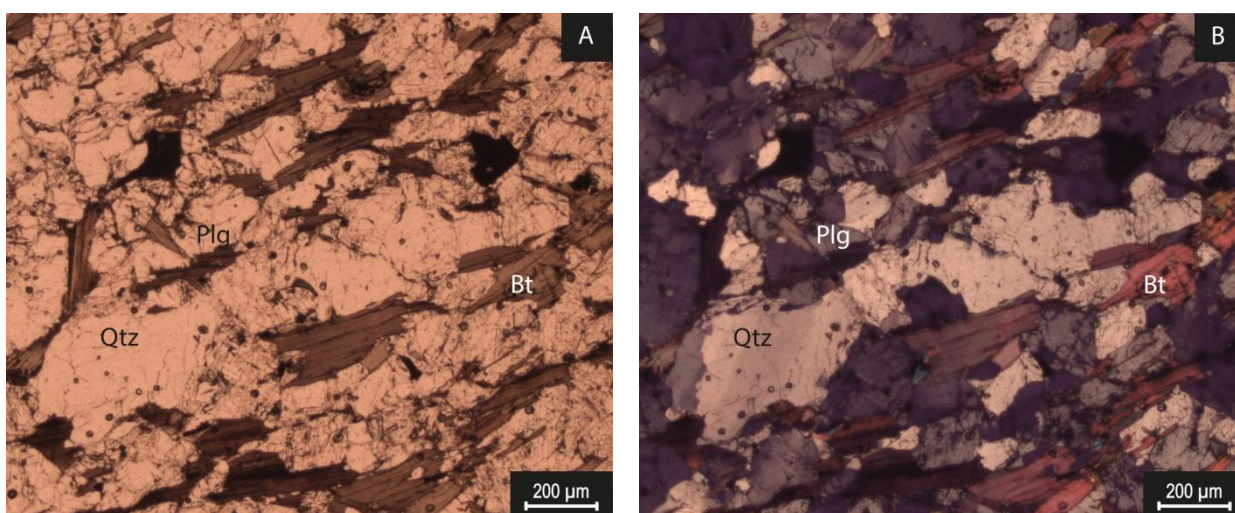


Figure 20 - Petrographic images of LE8. Quartz ribbons and biotite grains follow the same foliation, a in PPL, b in XPL.

Table 17 - Summary of petrographic observations of LE9. Percentages are estimated.

LE9					
Mineral content	Percentage	Texture	Protolith	Metamorphic facies	Rock name
biotite	26	gneissic bands are	sedimentary	amphibolite	biotite -
quartz	30	present, mainly			
fibrolite	15	expressed by fibrolite			gneiss
plagioclase	12				
muscovite	7	muscovite is often			
magnetite	6	intergrown with biotite			
chlorite	4				
apatite	accessory				
monazite	accessory				

The most notable mineral found in LE9 is fibrolite, also visible in the hand sample. Beside fibrolite, LE9 is mainly composed of biotite, muscovite, quartz and plagioclase. Biotite grains are dark due to high titanium content and are occasionally replaced by chlorite. LE9 exhibits gneissic bands, mainly expressed by fibrolite (Figure 21a, b). Furthermore, muscovite and biotite are sometimes intergrown (Figure 21c, d).

Muscovite and biotite are stable together, evidenced by their intergrown character. This implies that muscovite appears as a primary mineral and, hence, forms a stable assemblage with quartz. EDS and WDS analysis is performed on the opaques and feldspars of LE9. All the analysed opaques are magnetite and all the analysed feldspars are plagioclase. Fibrolite, biotite and muscovite together form a stable assemblage, strongly implying a sedimentary protolith. The fibrolite grains display a strong gneissic foliation. Fibrolite is a relatively lower grade metamorphic fibrous variety of sillimanite. Its presence constrains the thermal conditions of peak metamorphism being higher than 530 °C (Bohlen et al., 1991). Above 603 - 662 °C, quartz and muscovite react to sanidine, sillimanite and water (Althaus et al., 1970). Therefore, LE9 underwent peak metamorphism below these given temperatures, thus amphibolites facies conditions.

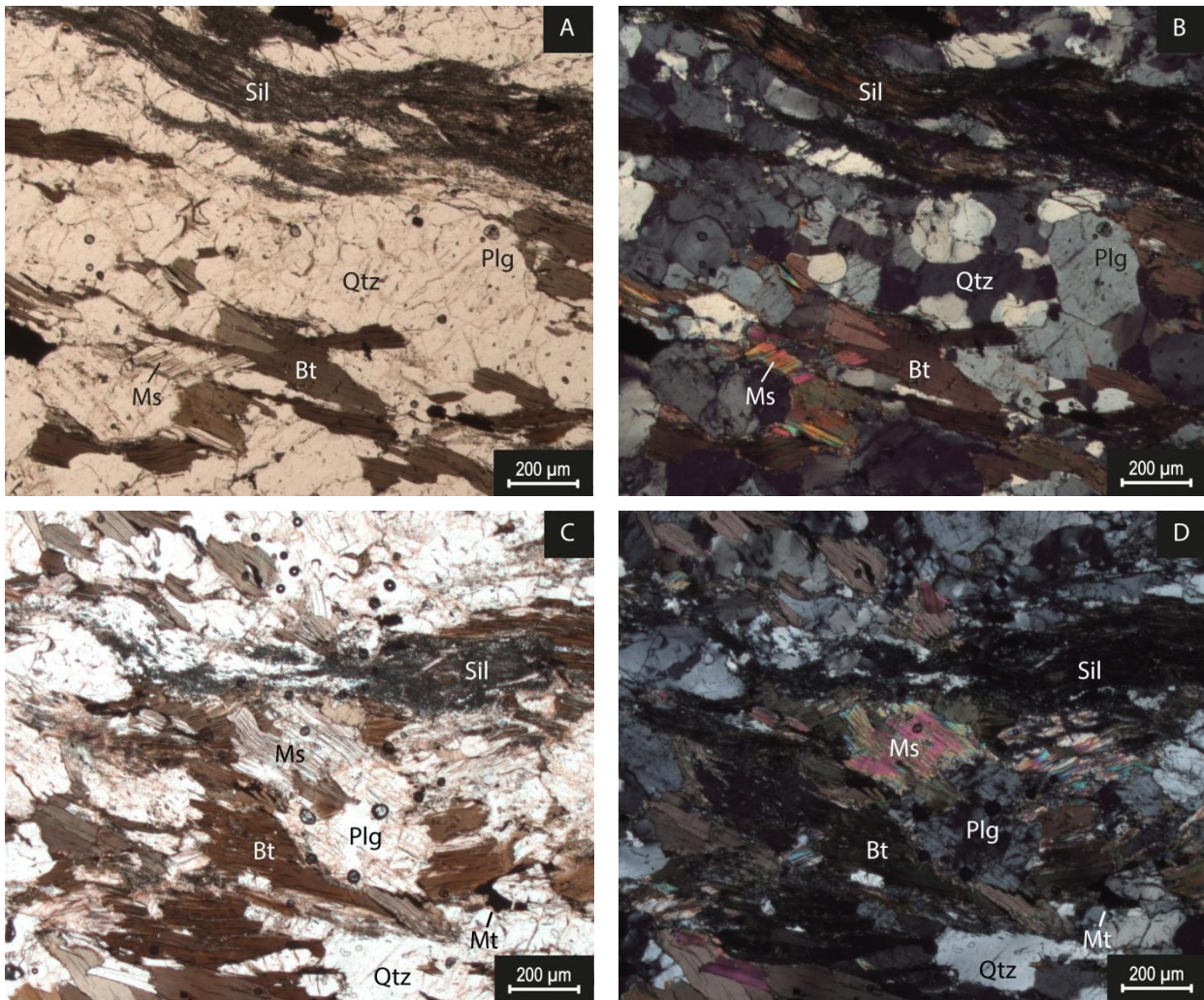


Figure 21 - Petrographic images of LE9. a & b) alternating bands with fibrolite, quartz and biotite, a in PPL, b in XPL. c & d) Muscovite is intergrown with biotite, c in PPL, d in XPL.

The Sara's Lust Gneisses were significantly deformed during exhumation. Shear zones are abundantly present and LB109B is mylonitised. In addition, retrograde reactions including fluid interactions resulted in the formation of muscovite, chlorite, iron-rich phases and epidote, and the introduction of secondary carbonates. Due to metamorphic reactions having erased much of the textures of the protolith, protolith identification can be challenging for the Sara's Lust Gneisses. Consequently, the protoliths of few samples were unidentifiable with petrography.

## 5.2. Rock classification based on bulk rock chemistry

All samples are, based on petrography, categorised in the felsic, mafic or sedimentary suite. The different suites of the Sara's Lust Gneisses are plotted in several discrimination diagrams for further rock classification. Bulk rock major element and trace element data used for these diagrams are reported in Tables 19 and 20, and Table 21, respectively. The Excel package Turnplot (Marshall, 1996) was used for plotting the Sara's Lust Gneisses in these diagrams.

The volcanic discrimination diagram of Le Bas et al. (1986) was used for the metavolcanic rocks of the Sara's Lust Gneisses (Figure 22). This diagram is partly based on  $K_2O$  content.  $K_2O$  was likely lost during fluid alteration (for further explanation, see Section 6.2.1.1.). Hence, classifications based on this diagram were likely affected by alteration. For this reason, the discrimination diagram of Winchester & Floyd (1977) was used as well to affirm the results of the diagram of Le Bas et al. Winchester & Floyd's diagram uses immobile trace elements and silica content to distinguish between volcanic rocks (Figure 23). LB107A and LB107B are both categorised in the mafic suite as for both the protoliths must have been mafic in composition so that chiefly hornblende formed during prograde metamorphism. Furthermore, their relatively low silica content ( $SiO_2 = 53 - 55$  wt. %) also imply mafic composition. Both samples are excluded from rock discrimination diagrams because it could not be derived whether the protoliths of LB107A and LB107B are either volcanic or plutonic. Instead, LB107A and LB107B are classified as amphibolites. The mafic suite of the Sara's Lust Gneisses comprises calc-alkaline and tholeiitic compositions, evidenced by the diagram of Irvine & Baragar (1971) (Figure 24).

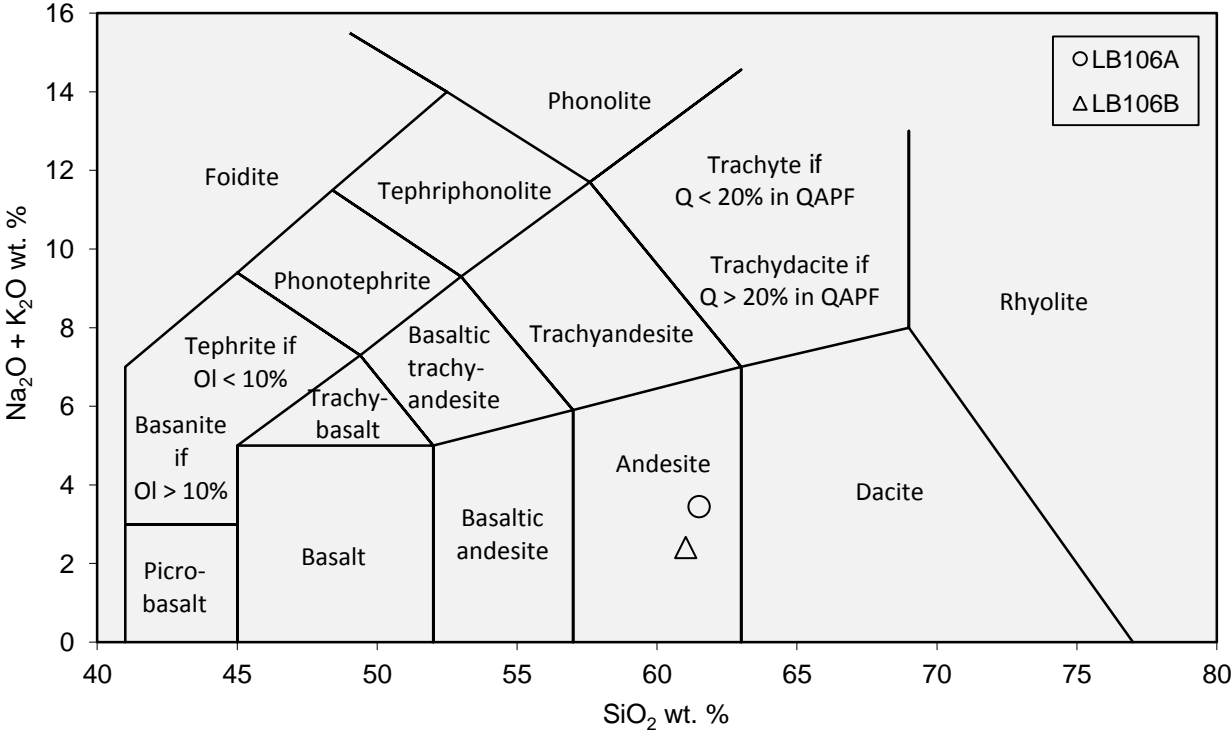


Figure 22 - Volcanic discrimination diagram from Le Bas et al. (1986).

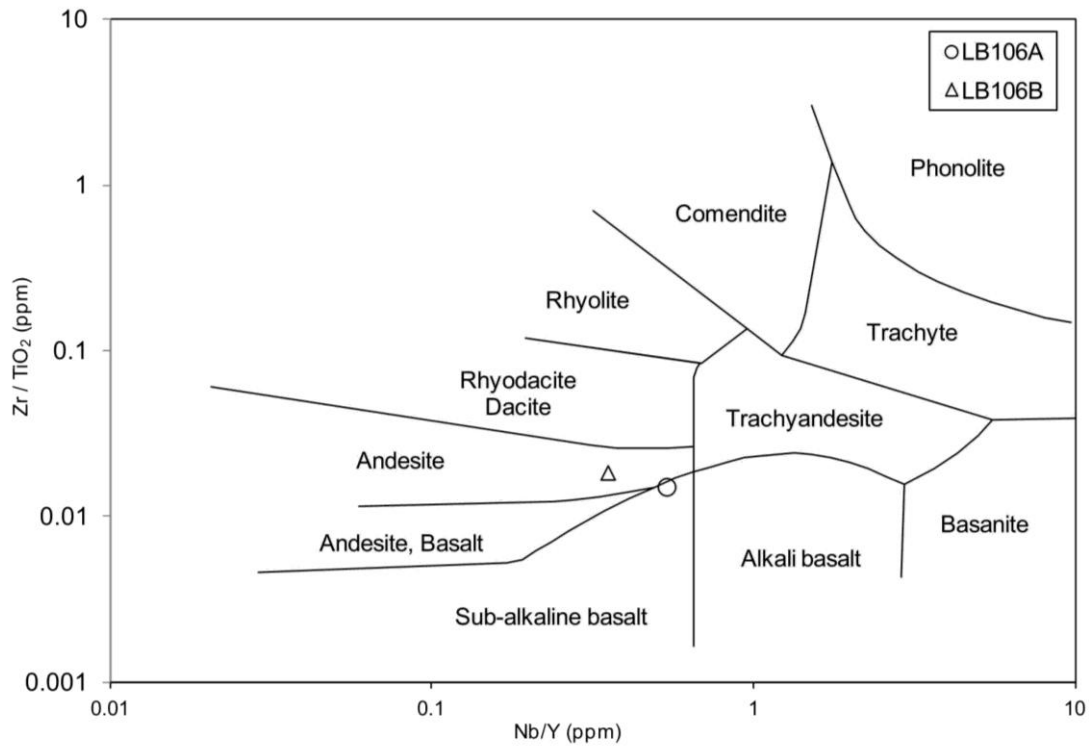


Figure 23 - Volcanic discrimination diagram of Winchester & Floyd (1977).

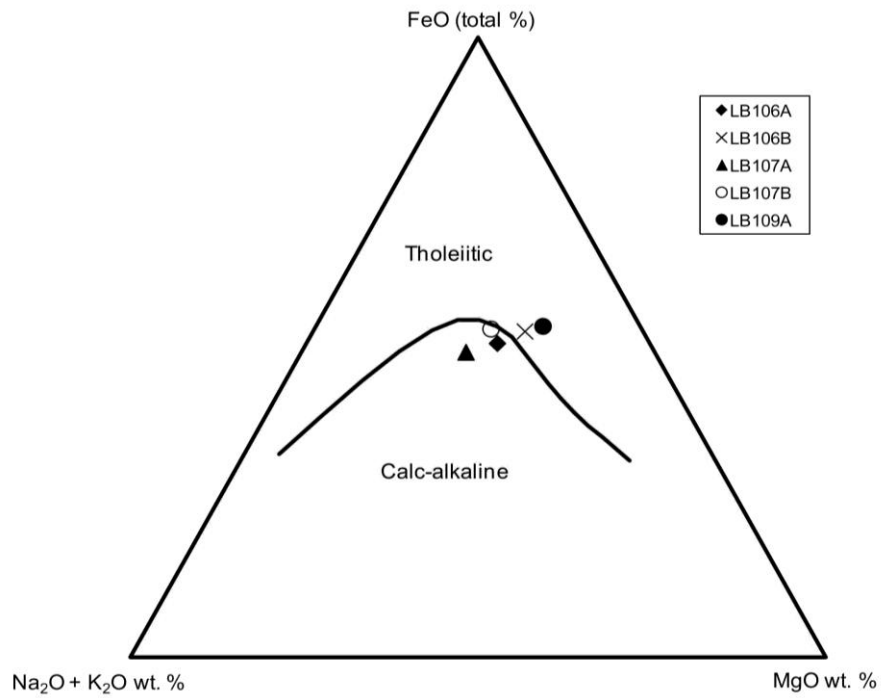


Figure 24 - Irvine & Baragar's (1971) diagram for the derivation of tholeiitic or calc-alkaline affinities for mafic volcanic.

The plutonic diagram from Streckeisen (1967) is based on mineral content (Figure 25). The abundance of quartz, plagioclase and K-feldspar was estimated based on petrographic observations. Streckeisen's diagram is only applicable for felsic plutons. To include mafic plutonic rocks and to inspect the consistency in rock classification results between multiple discrimination diagrams, the discrimination from Wilson (1989) was also used for pluton classification (Figure 26). A disadvantage of the latter diagram, however, is that it is not consistent with the boundaries of the volcanic diagram from Le Bas et al. (1986). Moreover, in Wilson's diagram pluton classification is partly based on  $K_2O$  content, which is likely affected by alteration. Yet, the results of Wilson's diagram are in reasonable agreement with the rock type outcomes of Streckeisen's diagram. Therefore, together they can be interpreted to give reliable results. KG1006 was not plotted in the diagrams of Streckeisen. Instead, the classification of KG1006 is discussed in Section 5.4.3.

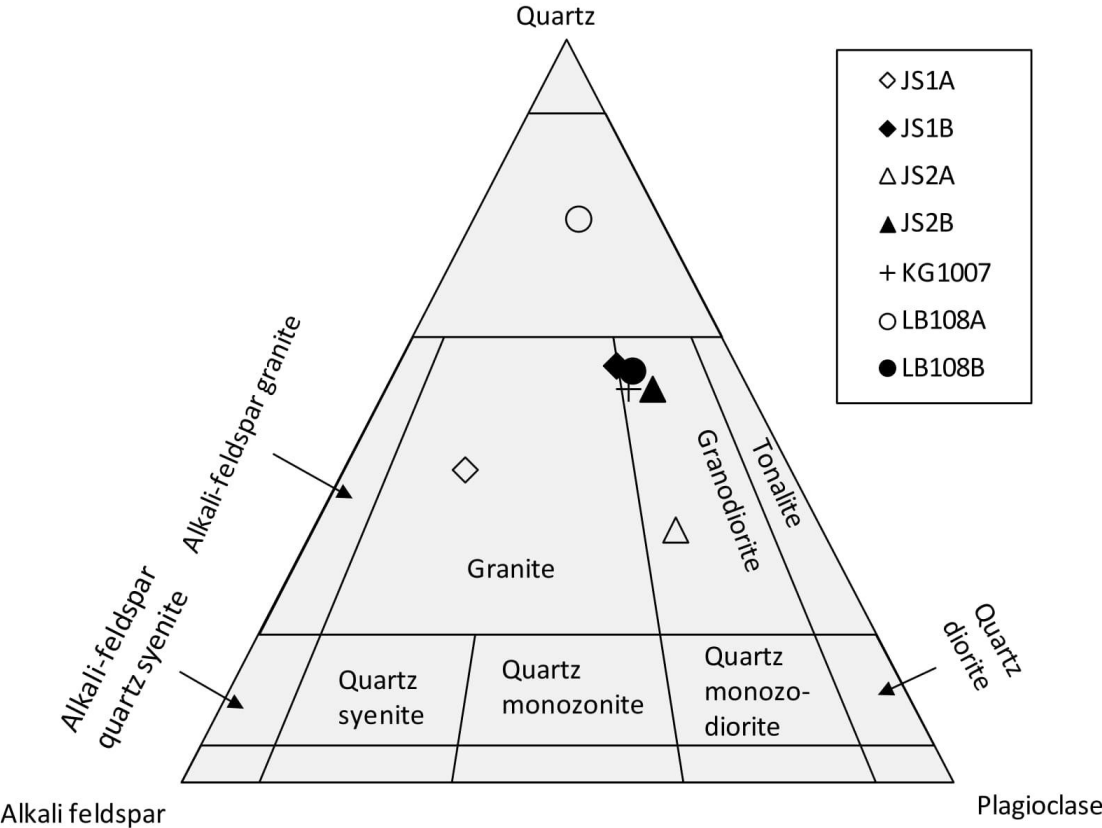


Figure 25 - Streckeisen's (1967) felsic plutonic discrimination diagram based on quartz and feldspar content.

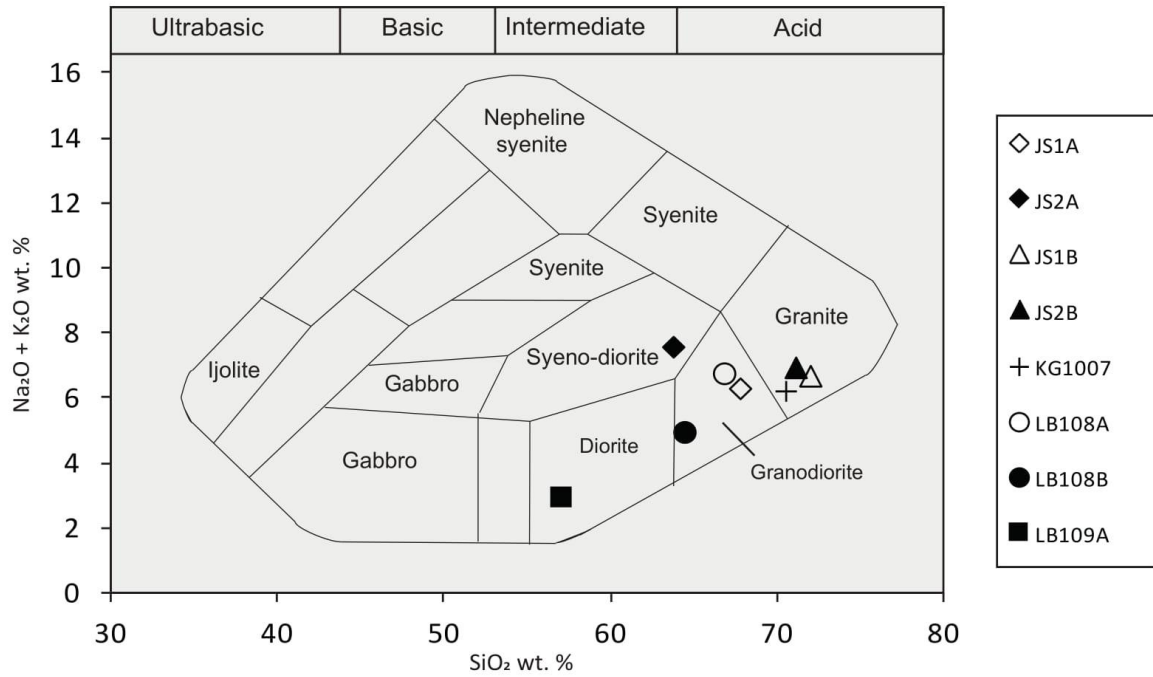


Figure 26 - Wilson's (1989) plutonic discrimination diagram.

For the metasediments of the Sara's Lust Gneisses, the diagram of Mackenzie & Garrels was used (1972) (Figure 27). A summary with all the deduced protoliths and rock types of the Sara's Lust Gneisses is given in Table 18.

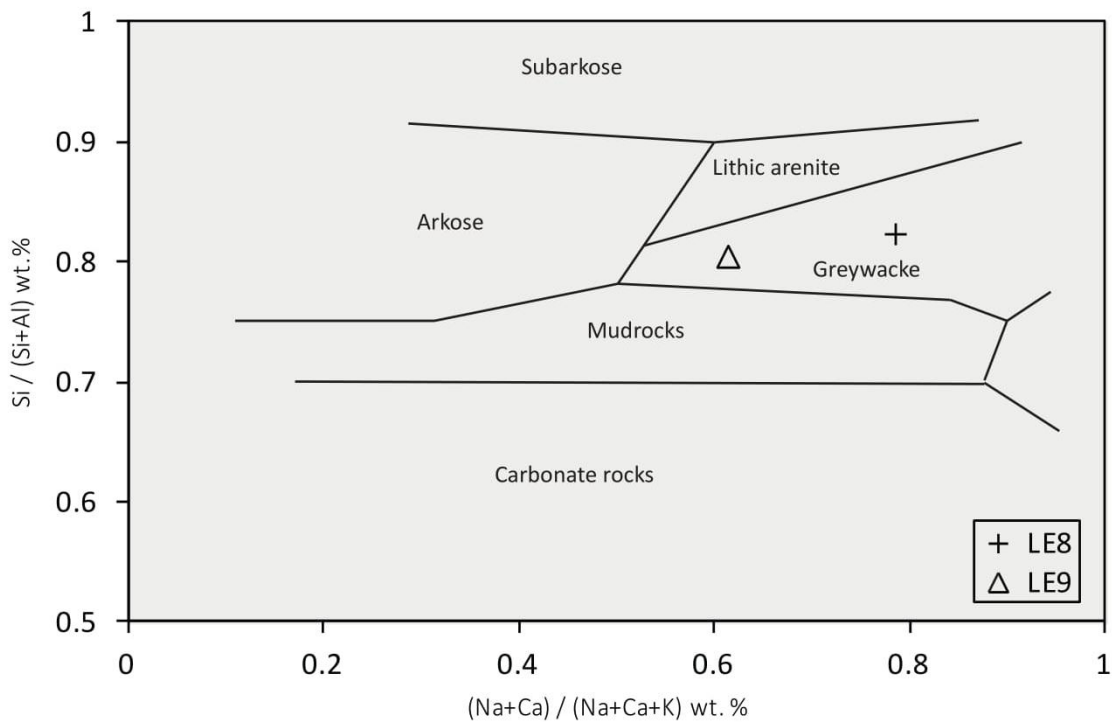


Figure 27 - Mackenzie & Garrels' (1972) discrimination diagrams for sediments.



Table 18 - Summary of all rock types. Classification of KG1006 is explained in Section 5.4.3.

Sample	Rock type / protolith classification based on:						Petrography
	Streckeisen (1967)	Wilson (1989)	Le Bas et al. (1986)	Winchester & Floyd (1977)	MacKenzie & Garrels (1972)	Moyen & Martin (2012)	
JS1A	Granite	Granodiorite					
JS1B	Granodiorite	Granodiorite					
JS2A	Granodiorite	Granite					
JS2B	Granodiorite	Granite					
KG1006							Trondhjemite
KG1007	Granite	Granite					
LB106A			(Meta-) andesite	(Meta-) sub-alkaline basalt			
LB106B			(Meta-) andesite	(Meta-) andesite			
LB107A							Amphibolite
LB107B							Amphibolite
LB108A	Granite	Granodiorite					
LB108B	Granodiorite	Granodiorite					
LB109A		(Meta-) diorite					
LB109B							Blastomylonite
LE8					(Meta-) greywacke		
LE9					(Meta-) greywacke		

### 5.3. Major element geochemistry

Bulk rock major element geochemistry analysis was conducted with XRF. JSA1 clearly contained compositional bands with black and white domains. These domains were separately analysed and were named JS1A1 and JS1A2, respectively. A bulk rock analysis was also carried out and was named JS1A3. LB109B was excluded from chemical analysis, as it exhibited such compositional heterogeneity on macroscopic scale that bulk rock analysis was considered invaluable. The major element oxides of the meta-igneous rocks were calculated on a loss-free basis, whereas the major element oxide concentrations of the metasedimentary rocks were calculated including LOI. The results of the bulk rock chemical analysis are reported in Tables 19 and 20.

Table 19 - Bulk rock major element data from XRF analysis. B.d. = below detection limits. LOI is excluded in the total weight percentage.

Oxide / Element	Unit	JS1A1	JS1A2	JS1A3	JS1B	JS2A	JS2B	KG1006	KG1007
Al <sub>2</sub> O <sub>3</sub>	wt. %	14.47	13.66	14.02	15.40	12.54	13.20	15.32	13.66
CaO		3.30	3.74	3.40	2.86	2.05	1.75	2.36	2.72
Fe <sub>2</sub> O <sub>3</sub>		5.63	4.21	4.93	6.29	3.66	4.21	1.84	4.26
K <sub>2</sub> O		2.10	1.27	1.71	3.20	2.98	2.71	1.63	1.11
MgO		0.98	0.69	0.83	1.05	0.61	0.58	0.79	0.36
MnO		0.10	0.09	0.09	0.11	0.07	0.07	0.02	0.07
Na <sub>2</sub> O		4.57	4.64	4.61	4.40	3.72	4.25	5.38	5.12
P <sub>2</sub> O <sub>5</sub>		0.14	0.14	0.13	0.19	0.07	0.07	0.09	0.07
SiO <sub>2</sub>		66.20	68.90	67.74	63.72	71.96	71.08	69.63	70.48
TiO <sub>2</sub>		0.63	0.56	0.57	0.72	0.39	0.46	0.29	0.34
Ba	ppm	502	171	434	938	952	899	1657	292
Cr		7	11	8	b.d.	7	6	22	b.d.
Ni		7	6	6	4	7	5	12	2
Sr		150	149	149	164	101	112	1046	110
Zr		337	265	313	348	298	401	116	255
LOI	wt. %	0.95	0.87	0.87	0.74	0.72	0.43	0.32	0.55
Total	wt. %	98.11	97.89	98.01	97.95	98.04	98.38	97.36	98.19

Table 19 - continued.

Oxide / Element	Unit	LB106A	LB106B	LB107A	LB107B	LB108A	LB108B	LB109A
Al <sub>2</sub> O <sub>3</sub>	wt. %	15.10	15.17	17.05	15.84	13.96	12.45	12.92
CaO		4.99	6.23	7.29	7.74	2.18	5.92	5.87
Fe <sub>2</sub> O <sub>3</sub>		7.93	7.41	9.61	9.93	6.23	7.64	11.21
K <sub>2</sub> O		0.93	1.01	1.01	0.30	1.18	0.71	0.74
MgO		4.28	4.27	4.59	4.73	1.13	1.45	6.81
MnO		0.15	0.18	0.17	0.15	0.10	0.25	0.15
Na <sub>2</sub> O		2.52	1.40	4.31	3.78	5.60	4.26	2.21
P <sub>2</sub> O <sub>5</sub>		0.15	0.20	0.23	0.23	0.09	0.41	0.08
SiO <sub>2</sub>		61.50	61.02	52.82	54.62	66.78	64.40	57.02
TiO <sub>2</sub>		0.95	0.85	1.16	1.19	0.47	0.56	1.07
Ba	ppm	418	384	704	134	825	524	390
Cr		30	27	101	26	16	15	209
Ni		25	26	53	28	7	12	88
Sr		249	201	248	348	186	209	232
Zr		144	158	189	131	383	316	120
LOI	wt. %	98.49	97.74	98.24	98.49	97.71	98.04	98.09
Total	wt. %	0.35	0.88	0.47	0.31	0.92	0.73	0.83

Table 20 - Bulk rock major element data from XRF analysis. B.d. = below detection limits. LOI is included in the total weight percentage.

Oxide / Element	Unit	LE8	LE9
Al <sub>2</sub> O <sub>3</sub>	wt. %	14.43	15.73
CaO		2.4	1.35
Fe <sub>2</sub> O <sub>3</sub>		6.48	8.47
K <sub>2</sub> O		1.69	2.37
MgO		1.48	2.18
MnO		0.09	0.08
Na <sub>2</sub> O		3.76	2.41
P <sub>2</sub> O <sub>5</sub>		0.1	0.07
SiO <sub>2</sub>		67.47	64.99
TiO <sub>2</sub>		0.71	0.8
Ba	ppm	471	467
Cr		146	156
Ni		36	50
Sr		255	201
Zr		172	166
LOI	wt. %	0.43	1.503
Total	wt. %	98.61	98.45

#### 5.4. Trace element geochemistry

LA-ICP-MS analysis was carried out to analyse the trace element concentrations. The LA-ICP-MS and XRF data were calibrated using SiO<sub>2</sub> content as an internal standard to correct for laser ablation yield. The trace element geochemical data are reported in Table 21.

Table 21 - Trace element geochemistry from LA-ICP-MS analysis. All values are in ppm. B. d. = below detection limits.

Element	JS1A1	JS1A2	JS1A3	JS1B	JS2A	JS2B	KG1006	KG1007
Sc	13.9	10.9	12	15.0	10.3	10.4	4.4	13.8
Ti	5180	4600	4600	5760	3160	3690	2600	2840
V	33.6	27	29	44	25	23.4	37.1	10.2
Cr	39	51	36	33	68	b.d.	60	b.d.
Co	42.4	43	45.3	30.1	45	47	69	37.5
Ni	b.d.	b.d.	b.d.	b.d.	b.d.	b.d.	b.d.	b.d.
Cu	b.d.	8.5	6	100	10	9.6	13	13.3
Zn	89.6	79	81	260	61	79	79	81
Rb	75.0	29.9	51	108	86	79.3	89	37.2
Sr	154.5	148	149	170	104	115	990	111.4
Y	45.2	43	42.2	51	42.7	54	7.8	39.6
Zr	380	283	341	383	330	460	126	295
Nb	22.8	27.3	23.2	27.0	25.2	27.0	4.8	18.4
Cs	1.5	0.5	1.1	2.24	0.7	0.8	2.4	0.9
Ba	473.8	160	410	940	970	870	1600	279
La	41.18	30.1	38.1	40	43	50	23.5	34.9
Ce	82	64	77	83	90	100	48	71
Pr	9	7.5	8.7	9.7	9.9	11.4	5.5	8.36
Nd	37	31	35	38.9	38.6	45	22	35
Sm	7.3	6.72	6.5	8.7	7.4	8.5	3.6	7.7
Eu	2	1.7	1.6	2.01	1.6	1.7	1.1	1.7
Gd	7.25	5.8	6.6	8.0	7.3	8.5	2.6	7.8
Tb	1.07	0.99	1.00	1.21	1.15	1.17	0.32	1.33
Dy	7.3	6.8	7.0	8.4	7.7	8.6	1.40	8.5
Ho	1.43	1.34	1.38	1.8	1.64	1.72	0.22	1.55
Er	4.5	4.14	4.1	5.2	4.5	5.2	0.7	4.2
Yb	4.56	4.6	4.1	5.5	4.3	5.0	0.6	3.3
Lu	0.7	0.71	0.59	0.82	0.72	0.80	0.09	0.41
Hf	8.8	6.5	8.3	9.1	8.6	11.3	3.4	7.4
Ta	2.23	3.1	2.5	2.23	2.4	1.9	1.4	1.50
Pb	5.3	5.0	5.3	8	10	11.6	13	14.2
Th	5.43	4.1	5.2	5.3	7.0	6.9	3.7	5.23
U	1.4	1.26	1.26	1.6	1.8	1.4	1.11	0.82

Table 21 - continued.

Element	LB106A	LB106B	LB107A	LB107B	LB108A	LB108B	LB109A	LE8	LE9
Sc	22.9	20.2	27.1	26	16.2	24.5	28.1	19	21.3
Ti	7900	6900	9400	9140	3770	8920	8660	5640	6430
V	193	182	187	206	37.7	186	217	112	161
Cr	65	41	147	52	53	37	250	210	230
Co	97	70	64.0	72.3	43.3	54.7	74.4	60	47.9
Ni	26	33	85	40	b.d.	b.d.	129	55	70.1
Cu	16.1	1580	9.0	300	15.4	63	13.7	17.4	5.3
Zn	80	83	130	18	71	115	105	103	124
Rb	29.9	33.1	29.9	2.01	41.7	24.1	29.8	66	118
Sr	259	207	257	342	177	250	245	254	208.4
Y	23.5	31	29.7	20.9	31.4	50.9	17.9	20.4	19.94
Zr	181	175	209	155	423	280	147	188	199
Nb	12.6	11.0	15.8	25.2	32.9	50.9	14.0	9.6	9.5
Cs	0.9	0.35	0.9	0.07	3.19	0.59	3.0	2.36	3.9
Ba	411	377	700	107	749	537	377	470	438
La	23.2	21.0	25.0	34.2	57.8	48	18.8	32.1	35.4
Ce	45	42.5	51.4	64.2	108.9	94	42.7	66.5	71.4
Pr	5.1	5.05	6.1	7.07	11.4	10.7	5.5	7.52	7.88
Nd	21.0	20.7	25.1	27.5	42.6	43	23.8	30.8	32.6
Sm	4.19	4.7	5.3	5.0	7.1	8.2	4.7	5.6	5.8
Eu	1.30	1.73	1.6	1.39	1.8	2.7	1.49	1.5	1.3
Gd	4.0	4.7	5.6	4.3	5.9	7.7	4.1	4.9	4.97
Tb	0.59	0.73	0.76	0.56	0.85	1.19	0.55	0.68	0.64
Dy	3.76	5.13	5.5	3.8	5.4	8.1	3.6	4.4	4.0
Ho	0.81	1.09	1.07	0.8	1.12	1.68	0.72	0.87	0.71
Er	2.3	3.2	3.2	2.3	2.93	4.98	1.99	2.52	2.04
Yb	2.3	2.97	3.0	2.26	3.1	5.4	1.8	2.4	2.05
Lu	0.35	0.46	0.45	0.31	0.51	0.75	0.25	0.35	0.30
Hf	4.3	4.4	4.96	4.0	9.1	6.42	3.66	5.2	5.19
Ta	1.71	1.66	1.87	2.1	2.75	3.29	1.68	1.18	1.13
Pb	4.3	3.8	3.8	100	4.7	6.82	2.9	17.2	13.3
Th	3.1	2.31	2.4	4	7.7	6.61	1.8	6.2	6.39
U	0.87	1.0	0.69	10	2.26	3.3	0.48	1.69	2.01

Elements that were measured with both LA-ICP-MS and XRF were used to construct a graph in which LA-ICP-MS data were divided over XRF data (Figure 28). This graph illustrates the measurement differences between the two techniques. It becomes apparent that LA-ICP-MS structurally overestimated Zr content compared to XRF, or conversely, XRF structurally underestimated Zr content compared to LA-ICP-MS, except for the analysis LB108B. Because XRF is a more precise technique compared to LA-ICP-MS, XRF data was used for Zr concentrations. Ti content also varied considerably within the three measurements per sample; Ti concentrations in LB106B varied the most, yielding a mean of 6872 ppm and a standard deviation of 227 ppm. Thence, XRF data was also used

for Ti concentrations. Ba and Sr content generally stayed within an acceptable error margin of 10%, except for Ba in LB107B and Sr in LB108B. LA-ICP-MS data was used for these elements.

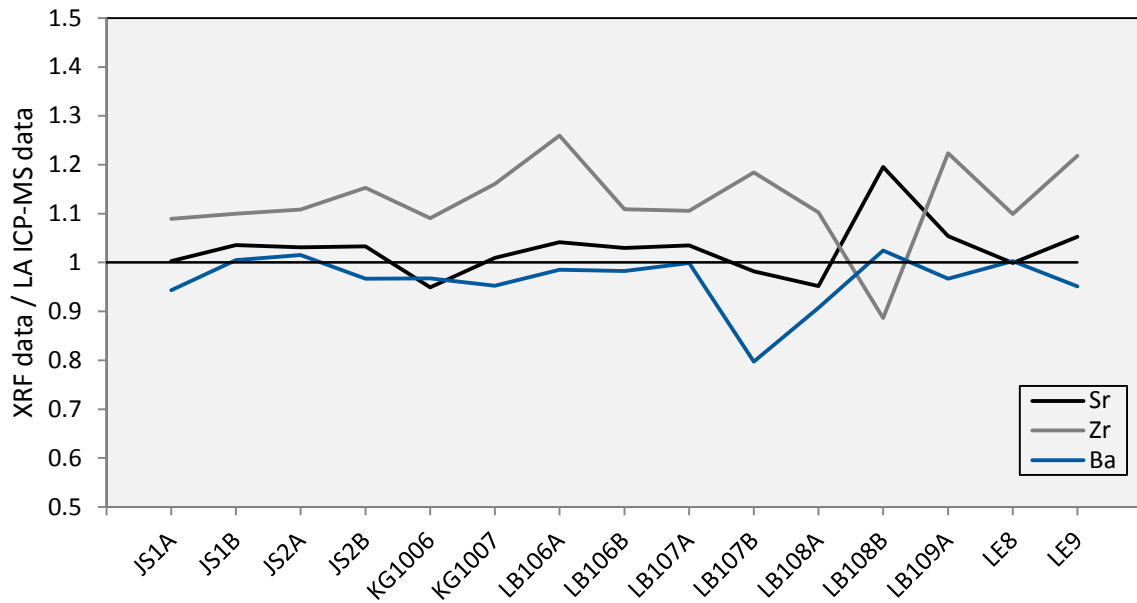


Figure 28 - Graph showing the deviation of LA-ICP-MS analysis for Sr, Zr and Ba compared to XRF.

For the different suites of the Sara's Lust Gneisses multiple-element diagrams and REE diagrams were constructed (Figures 29, 30, 31 and Figures 32, 33, 34, respectively).

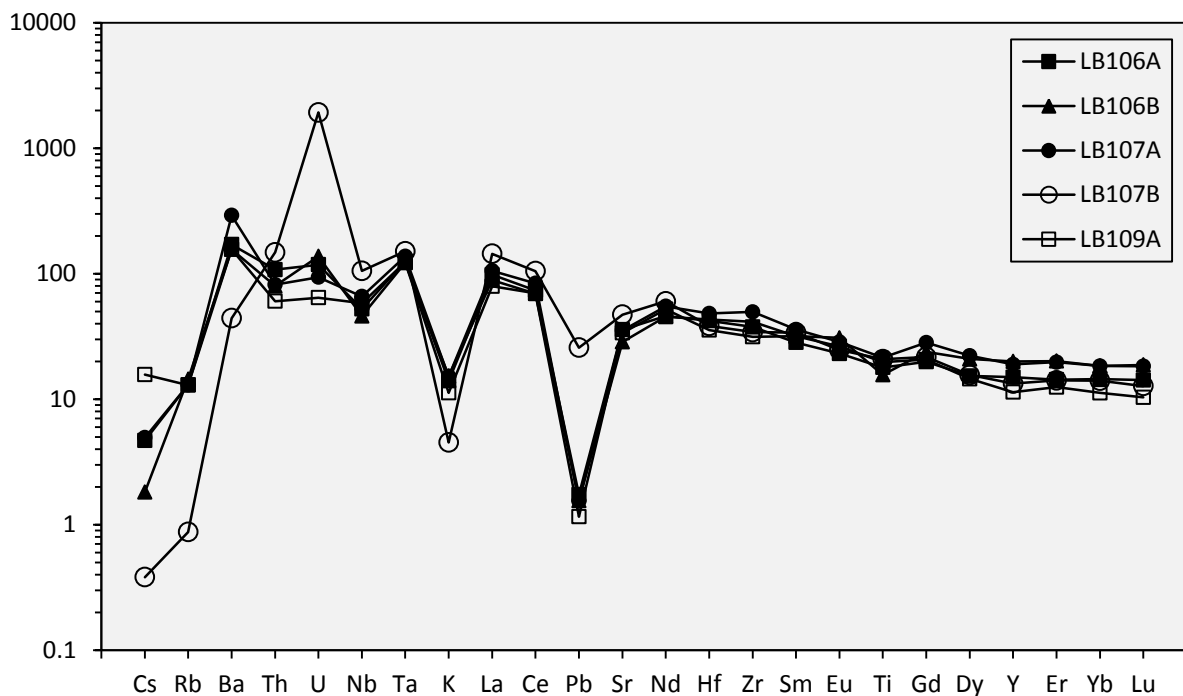


Figure 29- Multiple-element diagram of the mafic to intermediate suite of the Sara's Lust Gneisses. Normalised to chondritic values from McDonough & Sun (1995).

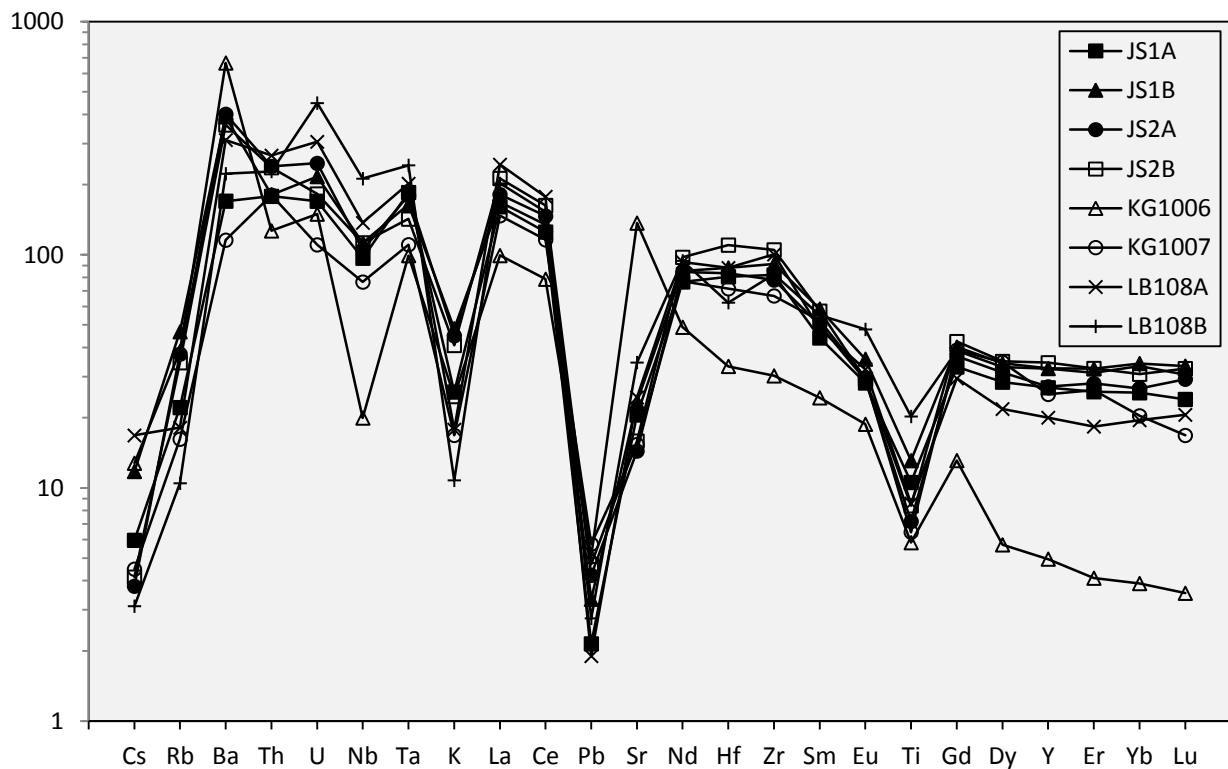


Figure 30 - Multiple-element diagram of the felsic suite of the Sara's Lust Gneisses. Normalised to chondritic values from Mcdonough & Sun (1995).

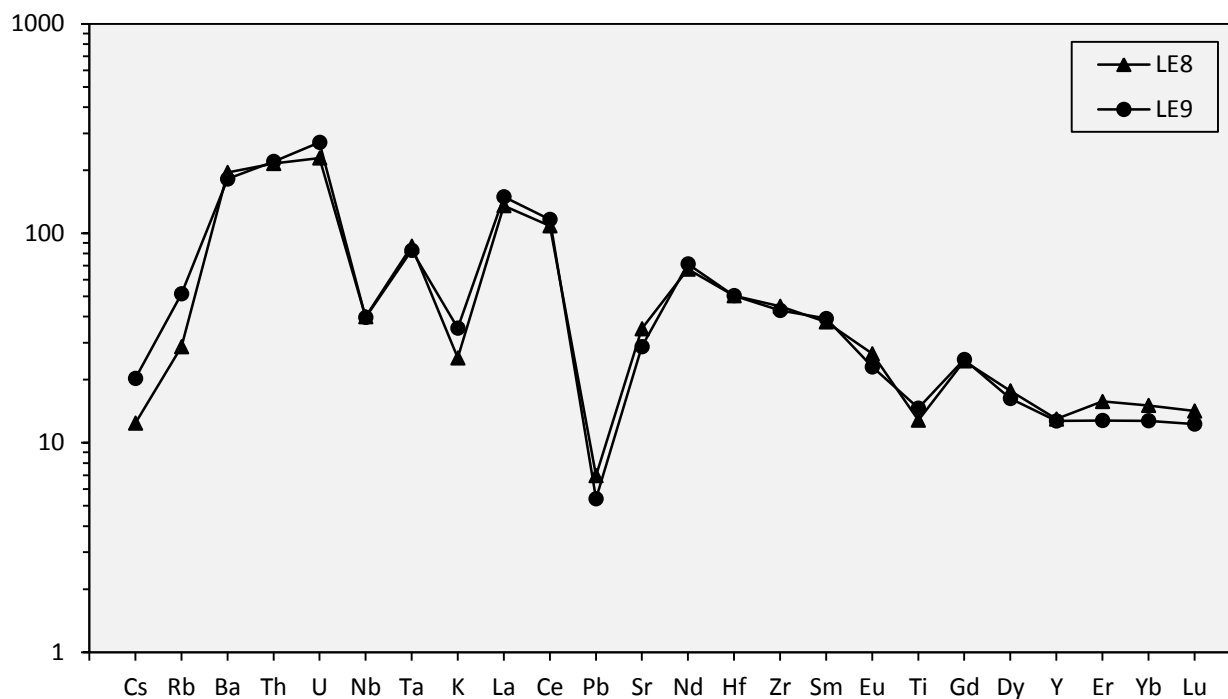
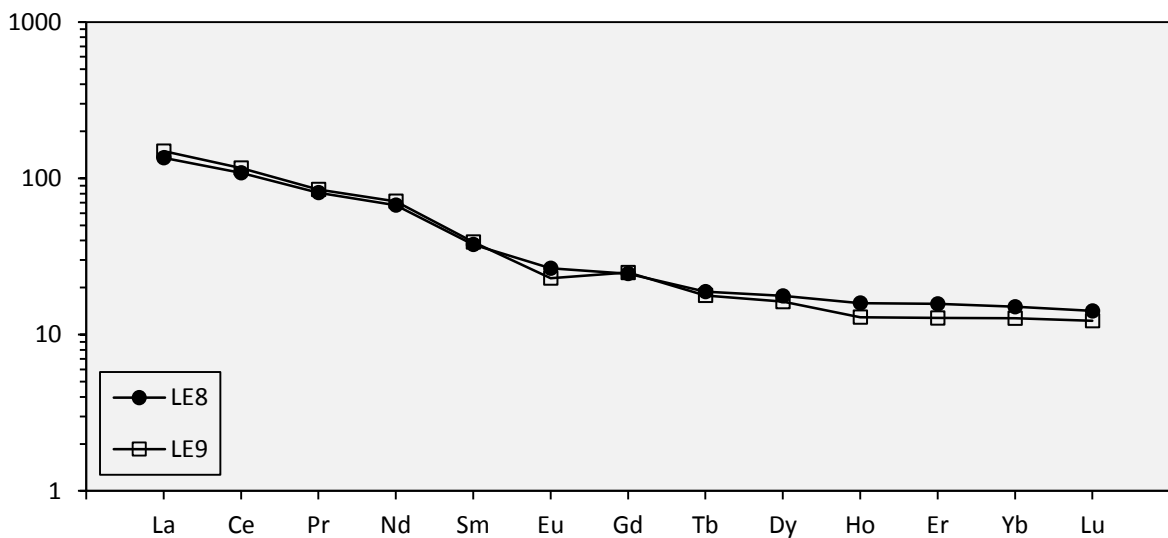
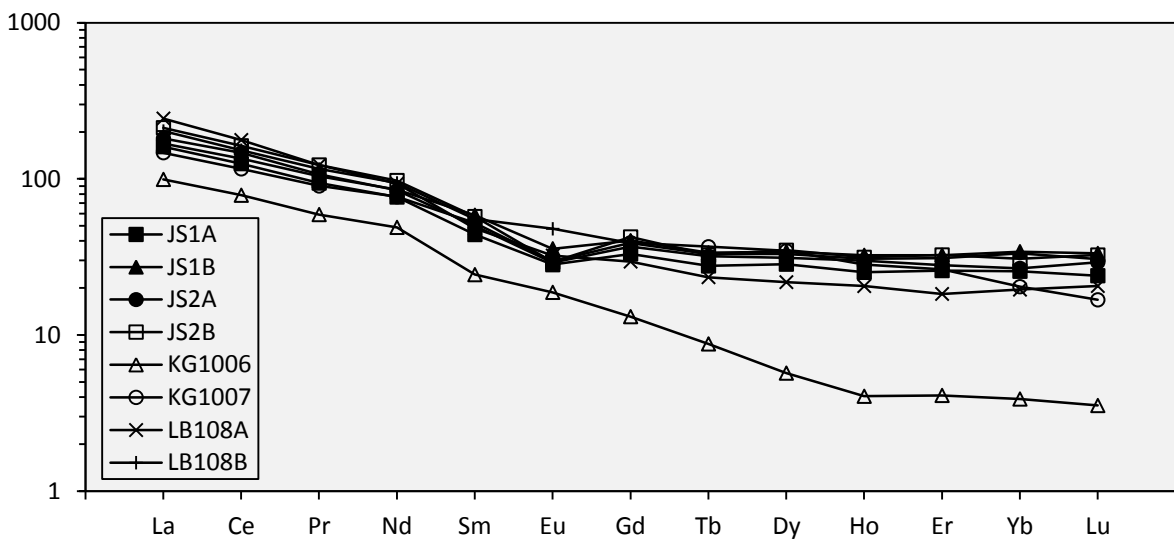
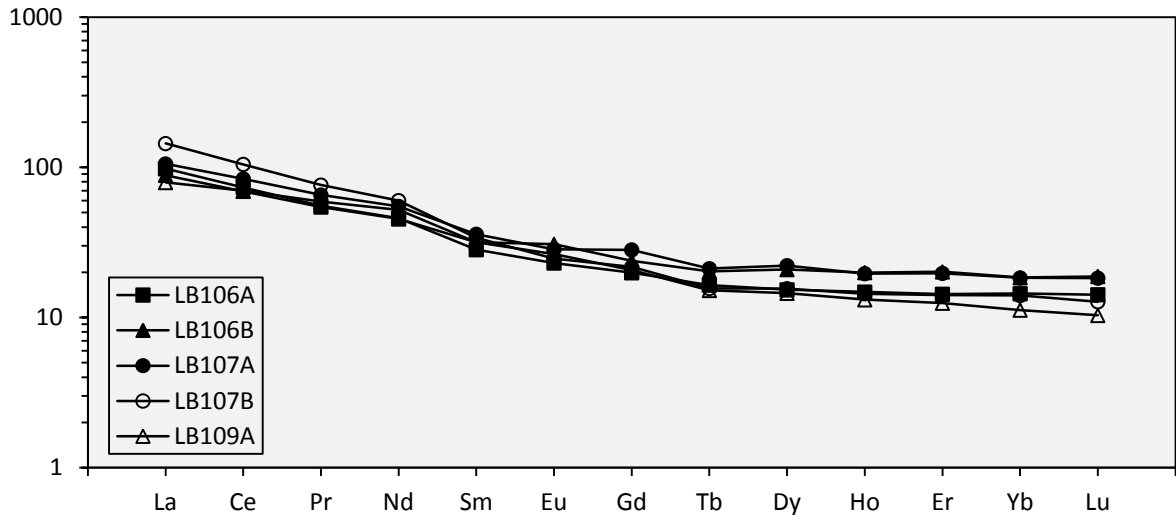


Figure 31 - Multiple-element diagram of the sedimentary suite of the Sara's Lust Gneisses. Normalised to chondritic values from Mcdonough & Sun (1995).



Top: Figure 32 - REE diagram of the mafic suite of the Sara's Lust Gneisses. Middle: Figure 33 - REE diagram of the felsic suite of the Sara's Lust Gneisses. Bottom: Figure 34 - REE diagram of the sedimentary suite of the Sara's Lust Gneisses. All concentrations were normalised to chondritic values from Mcdonough & Sun (1995).



#### ***5.4.1. General trace element trends in the Sara's Lust Gneisses***

All samples exhibit a negative anomaly in the large ion lithophile (LIL) elements K, Pb, Cs and Rb. A negative Sr anomaly is also generally present, with KG1006 being an exception for it exhibits a prominent positive Sr anomaly. To a certain extent, all samples possess negative Nb and Ti anomalies. Further, a positive Ba anomaly is present in the majority of the samples, except for JS1A, KG1007 and LB107B, which are, conversely, relatively depleted in Ba.

#### ***5.4.2. Trace element geochemistry of the mafic to intermediate suite***

Beside the general trends present in the mafic suite, the mafics all show an enrichment in incompatible elements (Figure 29). Further, all samples exhibit a slight Th depletion. LB107B is, moreover, most depleted in Cs, Ba and K, shows a prominent enrichment in U, and is less depleted in Pb. LB109A is less depleted in Cs and less enriched in U compared to other samples in the mafic suite. The REE pattern does not show prominent anomalies (Figure 32). LB109B exhibits the flattest REE pattern and LB107B exhibits the steepest REE pattern. Further, the mafic samples all possess a marginal positive Nd anomaly. A minor positive Eu anomaly is only present in LB106B. Furthermore, all mafics seem to display a slight relative depletion in Tb, though this is very minor. Lastly, LB109A and, to a lesser extent, LB106A are marginally lower in HREE.

#### ***5.4.3. Trace element geochemistry of the felsic suite***

The anomalies present in all suites of the Sara's Lust Gneisses are prominent in the felsic suite, especially the negative Ti anomaly. The multi-element diagram shows that LB108B is most enriched in incompatible elements, with slightly enriched in U and Ta and a smaller negative anomaly in Nb (Figure 30). It also possesses the lowest depletion in Ti. KG1006 exhibits the most deviating REE pattern. It is more depleted in Th, Nb and more enriched in Ba and Sr. The most notable difference is observable in the REE pattern of the felsic suite (Figure 33), as KG1006 exhibits a steeper REE graph for it is more depleted in HREE compared to LREE. All REEs are, withal, more depleted in KG1006. Further, all felsic samples exhibit a negative Eu anomaly, except for LB108B and KG1006. This depletion in Eu is not always clearly visible due to the prominent negative Ti anomaly. Further, KG1007 is lower in Yb and Lu content.

KG1006 possesses a REE pattern reminiscent to TTGs. For validation, the granitoids are plotted in the TTG discrimination diagram of Martin (1986) (Figure 35). KG1006 has significantly lower La / Yb. It is, as a result, plotted in the 'Archean TTG' field. For this reason, KG1006 is compared with TTGs for other TTG major and trace element signatures, using Moyen's (2011) TTG database (Figure 36). It becomes apparent that KG1006 generally follows the geochemical trends of TTGs, with one exception being the Sr content of KG1006 as it contains, compared to other TTGs, anomalously high Sr.

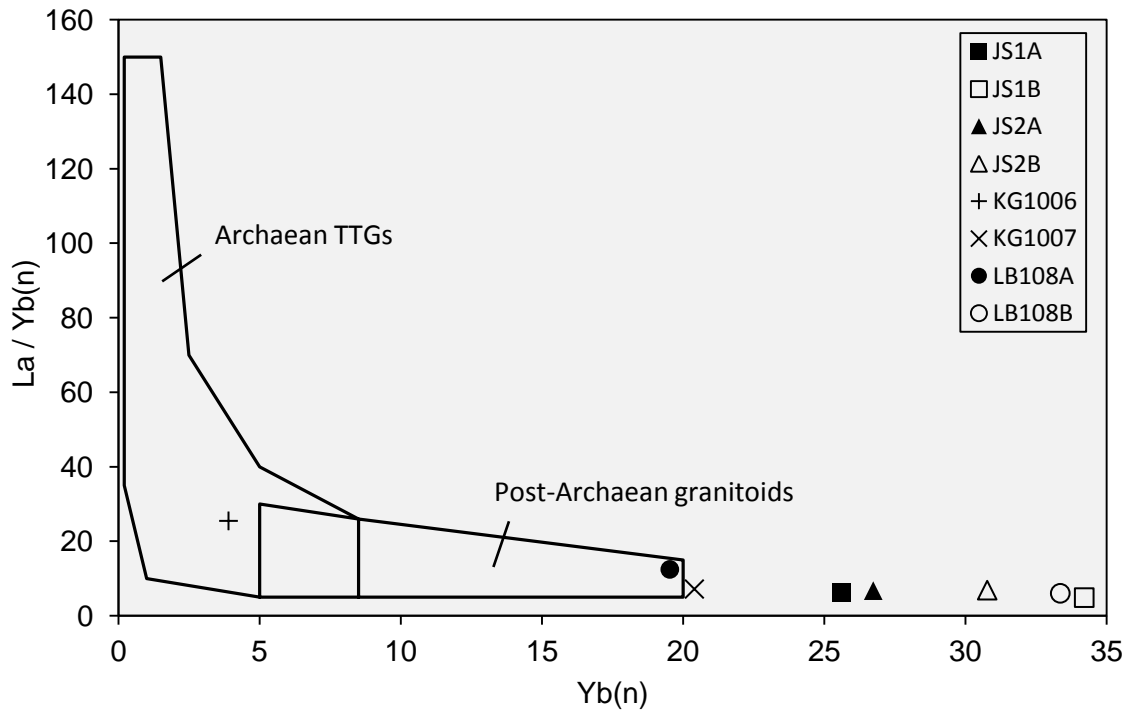


Figure 35 - Martin's (1986) discrimination diagram between TTGs and granitoids, based on La and Yb content.

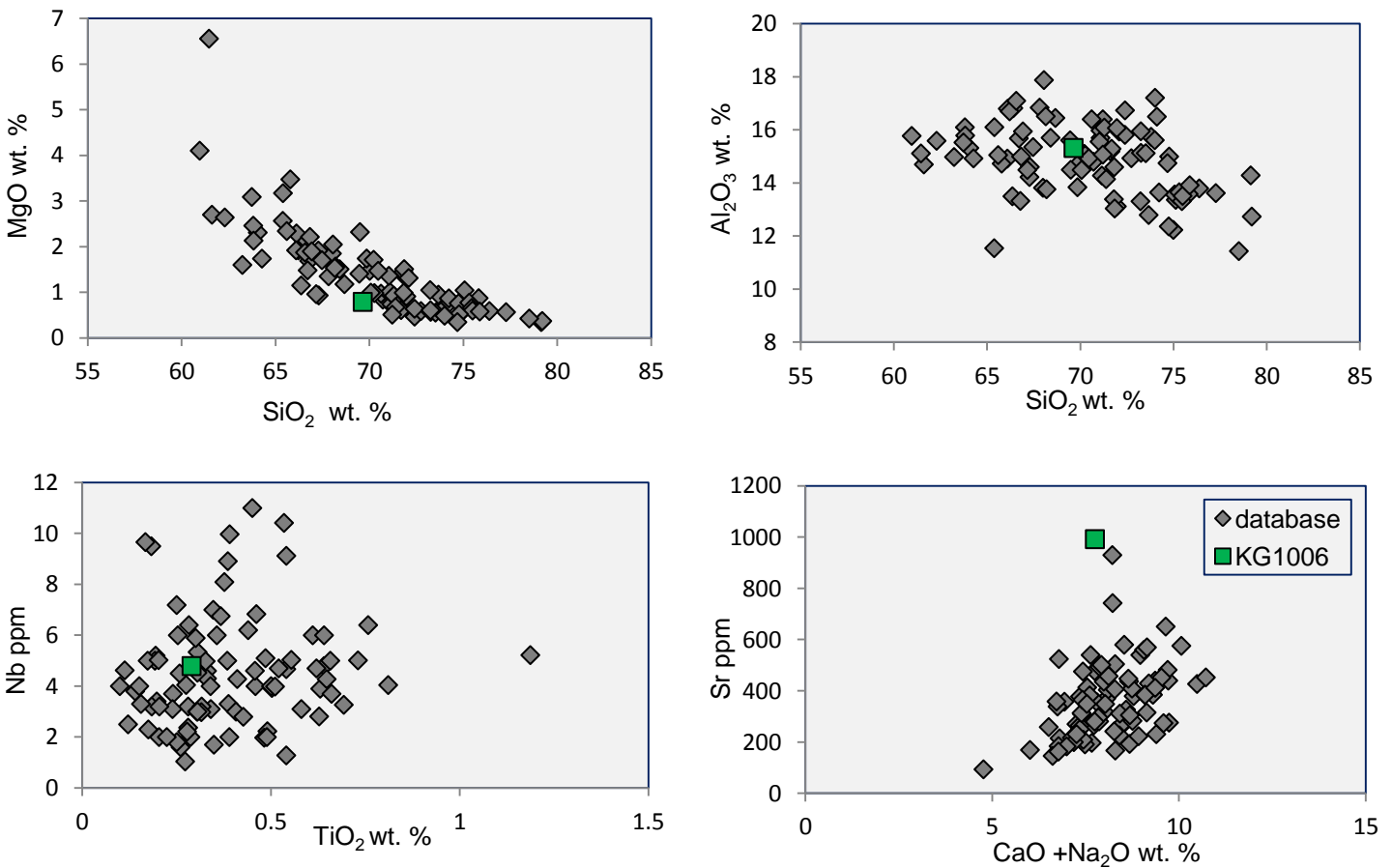


Figure 36 - Four diagrams illustrating the geochemical similarity between KG1006 and TTGs. Geochemical data of the TTGs if from Moyen (2011).

Table 22 shows several geochemical signatures for granodiorite, trondhjemite and tonalite. Signature values for granodiorite, trondhjemite and tonalite are taken from Moyen & Martin (2012). Table 22 demonstrates that KG1006 is best called a trondhjemite. Mineralogically, trondhjemites only contain biotite as mafic mineral, whereas tonalities contain hornblende and biotite. The mineralogy of KG1006 is, hence, also consistent with a trondhjemitic composition (Table 6).

*Table 22 - Several characteristic geochemical concentrations for TTGs. The dark grey cells exhibit what rock type the concentrations of KG1006 are the closest to per oxide / element. Characteristic data for TTGs is from Moyen & Martin (2012).*

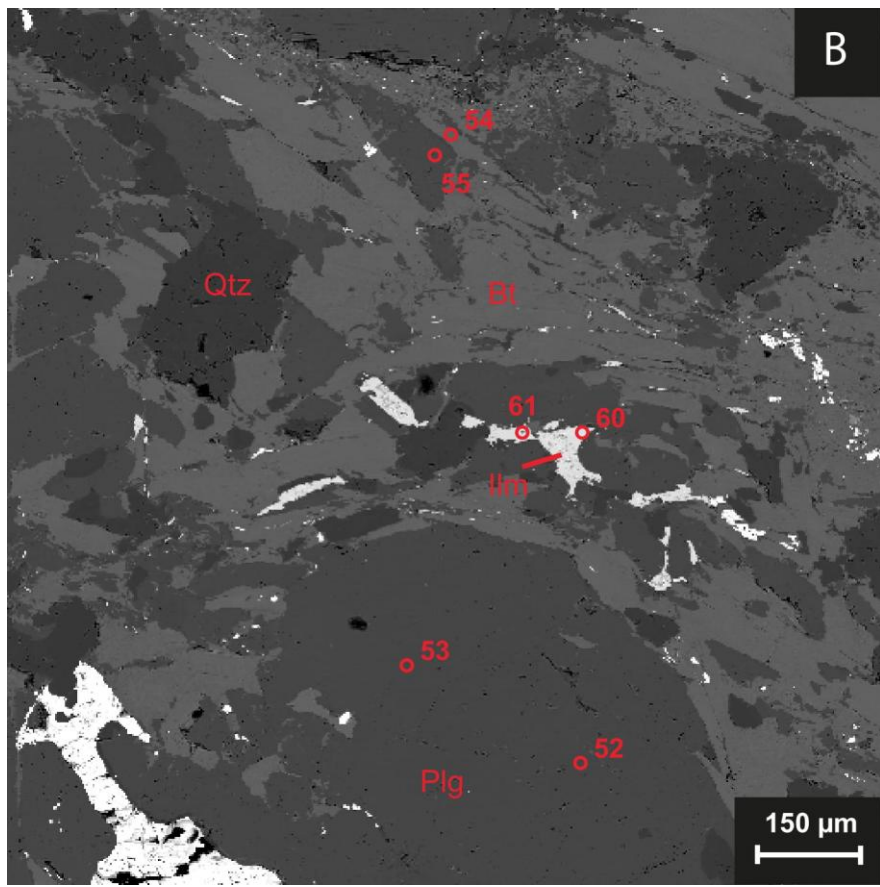
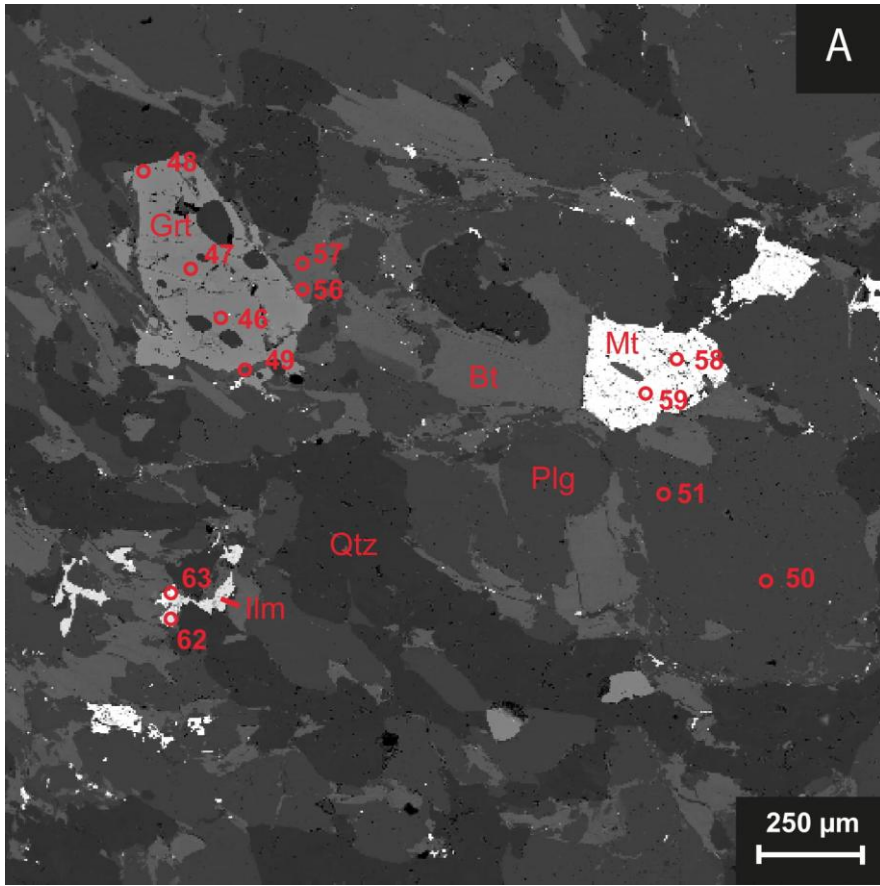
Oxide / element	Granodiorite	Trondhjemite	Tonalite	KG1006
SiO <sub>2</sub>	70-75 wt. %	70-75 wt. %	65-70 wt. %	69.63 wt. %
Fe <sub>2</sub> O <sub>3</sub> + MgO + MnO + TiO <sub>2</sub>	<4 wt. %	<5 wt. %	<5 wt. %	2.94 wt. %
K <sub>2</sub> O	~3 wt. %	0.5-2.0 wt. %	0.5-2.0 wt. %	1.63 wt. %
Na <sub>2</sub> O	3-5 wt. %	>5 wt. %	>6 wt. %	5.38 wt. %
K <sub>2</sub> O / Na <sub>2</sub> O	0.8-1	0.3-0.6	0.3-0.6	0.30
Al <sub>2</sub> O <sub>3</sub>	~14 wt. %	~16 wt. %	~14 wt. %	15.32 wt. %
Yb	<4 ppm	<1 ppm	<2 ppm	0.63 ppm
La	>25 ppm	>10 ppm	>10 ppm	23.53 ppm
Sr / Y	5-40	50-500	10-50	127.54

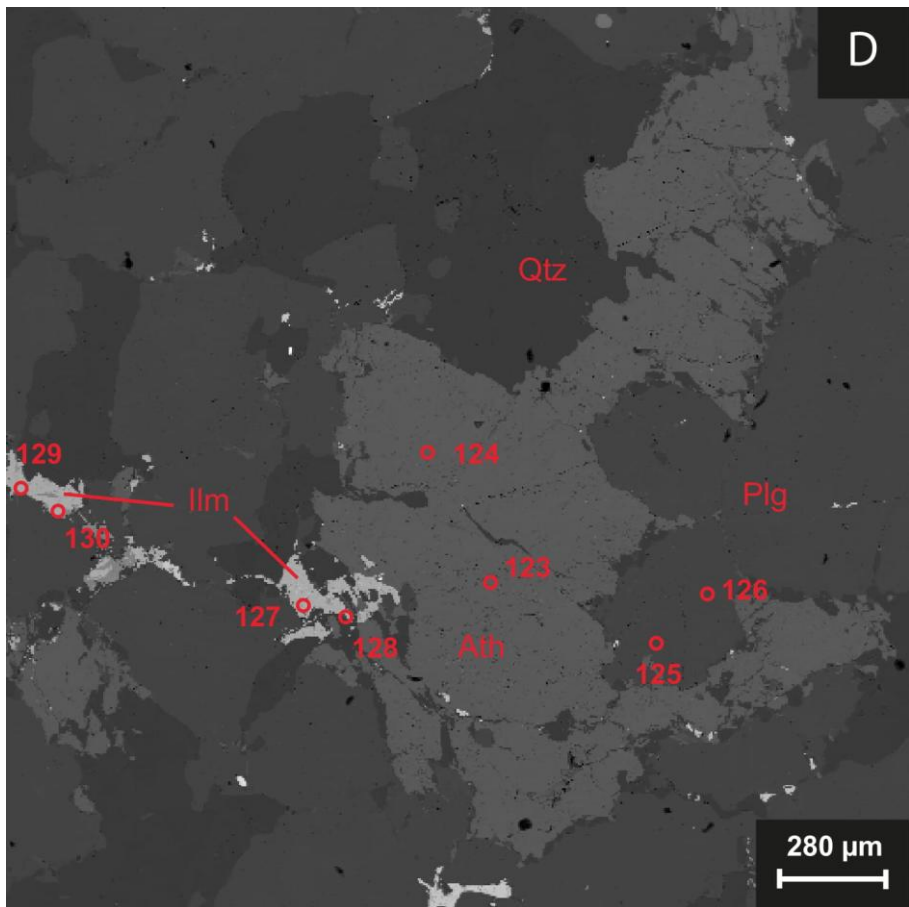
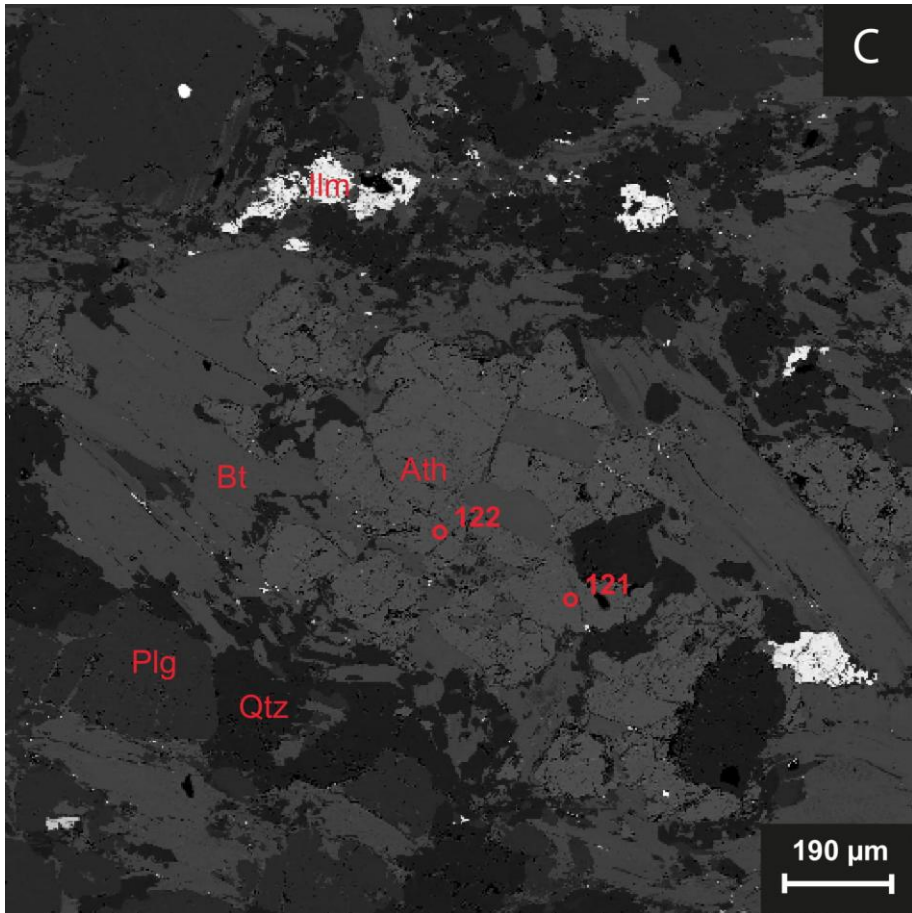
#### **5.4.4. Trace element geochemistry of the sedimentary suite**

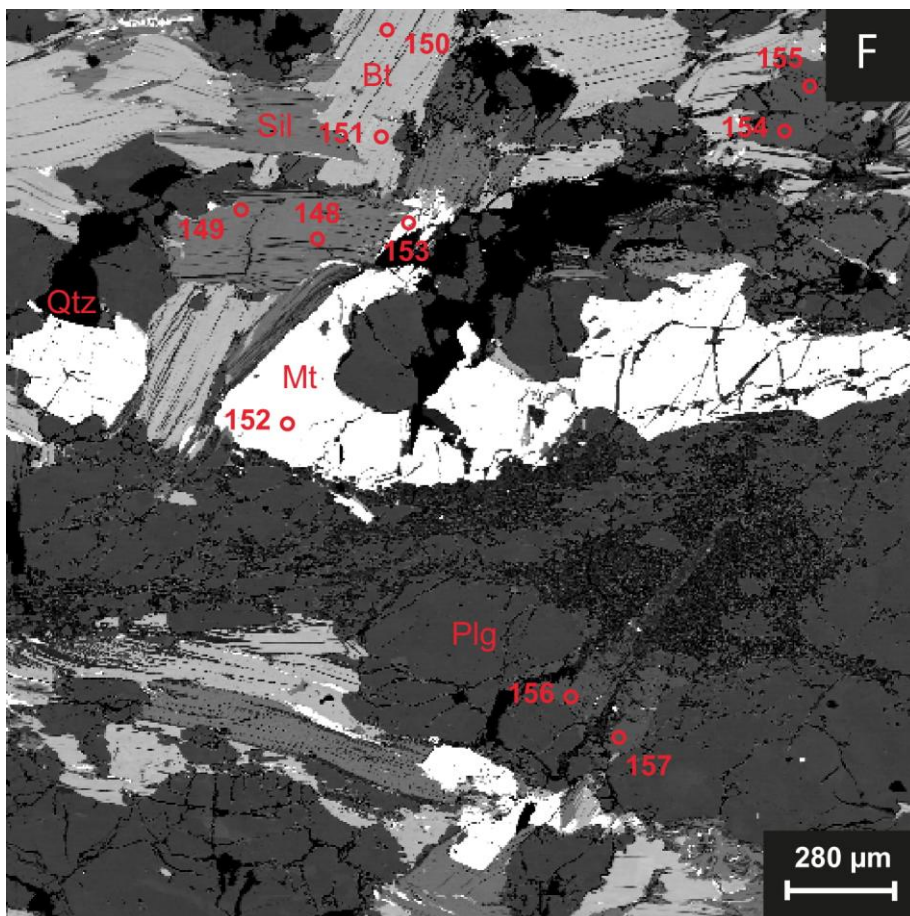
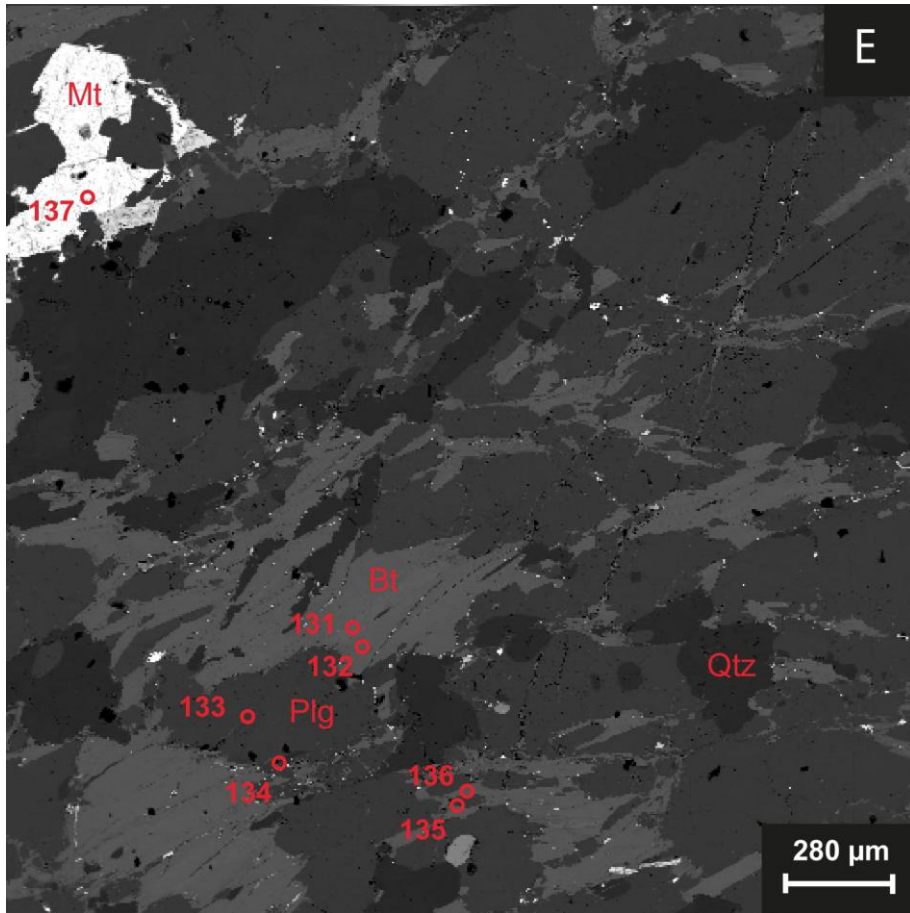
LE8 and LE9 possess very similar multi-element and REE abundances. LE8 is more depleted in Cs, Rb and K (Figure 31). LE9 is slightly higher in LREE and lower in HREE content (Figure 34). LE9 exhibits, furthermore, a small negative Eu anomaly.

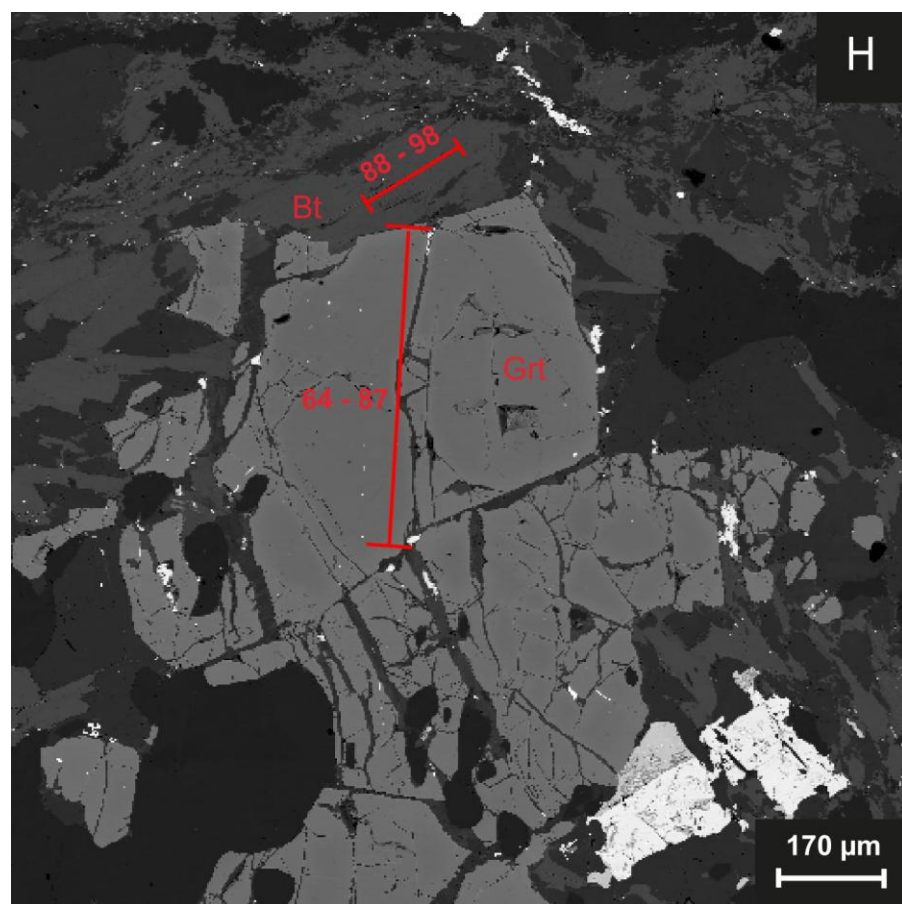
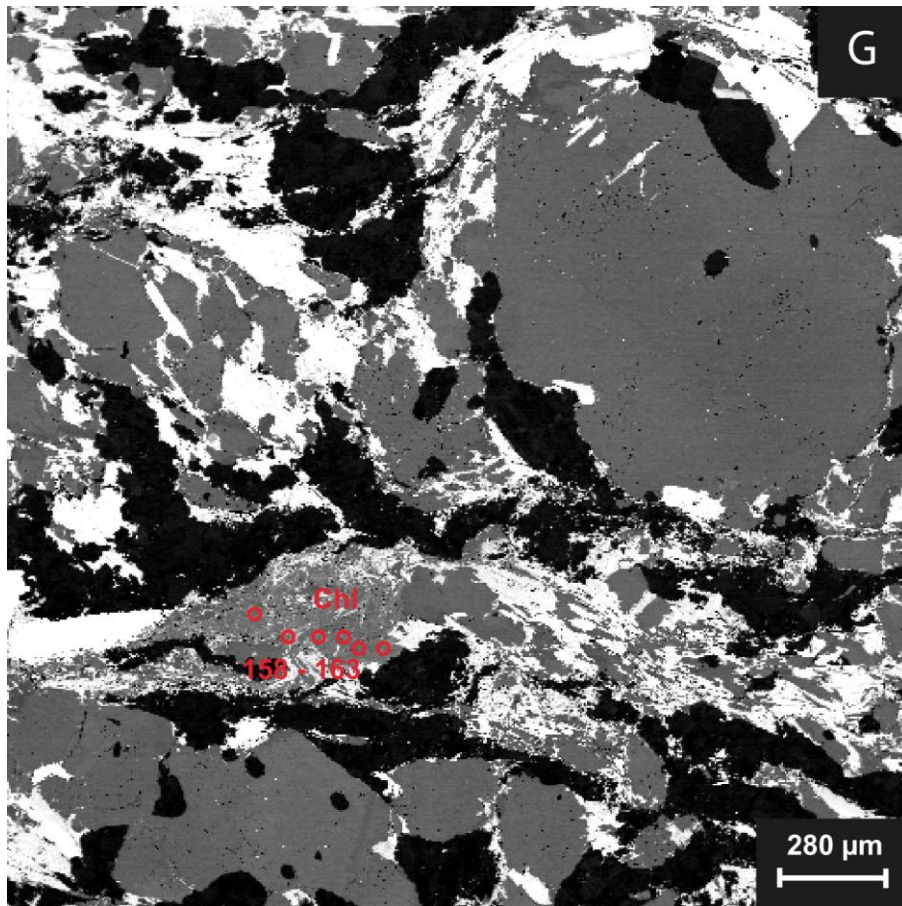
#### **5.5. Electron Microprobe Analysis**

LB106A, LB106B and LE9 were selected for EPM analysis. Biotite, chlorite, amphibole, feldspar, garnet, opaque minerals and sillimanite were chemically analysed. Mineral formulas were deduced from EPM data based on stoichiometric ratios using the ideal amount of oxygen atoms and cations. For hydrated minerals the ideal amount of OH-groups was added. Fe(III) content was calculated by continuously adding Fe(III) until the optimal ratio between Fe(II) and Fe(III) was reached with respect to the charge balance of the mineral formulae. Figure 37 comprises the WDS images and Tables 23 - 31 cover the corresponding chemical data sorted by mineral phase.









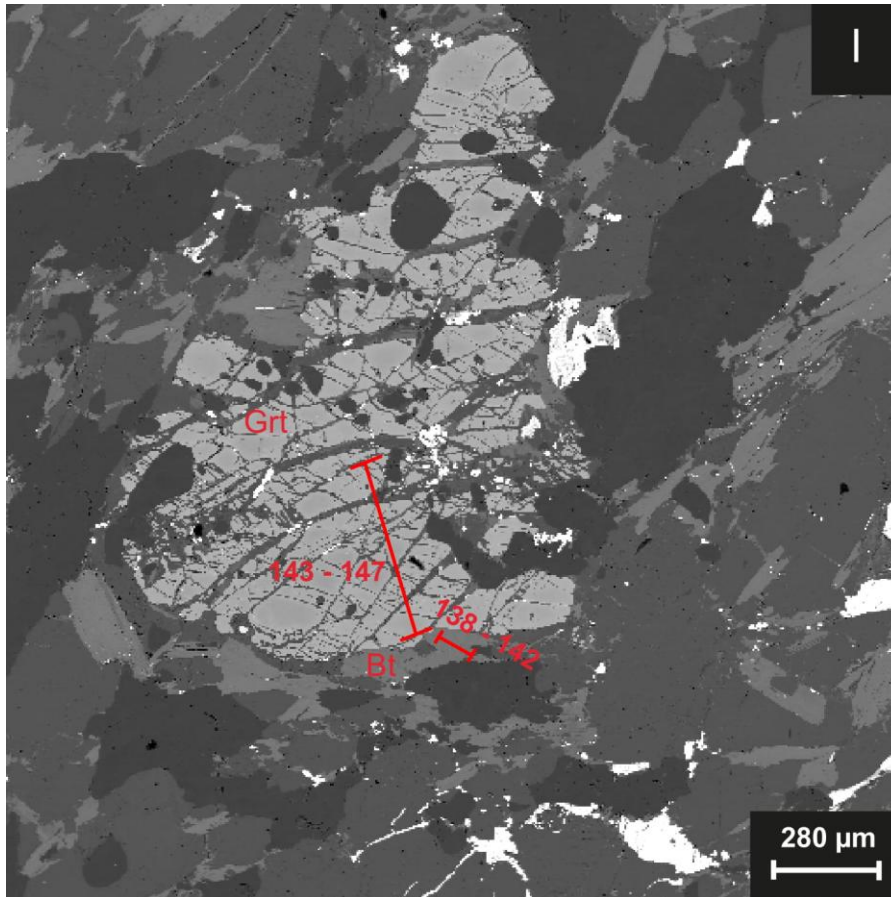


Figure 37 - WDS images of the Sara's Lust Gneisses. Phase names are indicated in red. The numbers in red are the measurement numbers and cohere to '#' in Tables 23 - 31. Image a, b, c, g & h are from LB106A, image c, d, e & i are from LB106B and image f is from LE9.

### 5.5.1. Biotite

Table 23 covers the chemical data of the analysed biotites. Chemical data of the biotites used for geothermometry are reported in Appendix B. The chemical formula of biotite can be derived with 4 OH-groups, an ideal amount of 22 oxides and 16 cations. However, the analysed biotites have high Ti content. In biotite, Ti often substitutes for two bivalent cations. Additionally, K and Na are solely present in the A-site, thus they have to be excluded from the M-sites. Hence, the ideal total cations are assumed to add up to  $14 + K + Na - Ti$ . Ferric iron was calculated with charge balances. The chemical formulae of the biotites (Table 24) show that the A-site is not completely filled. Furthermore, the biotites from LB106A and LB106B differ significantly in composition compared to the biotites from LE9. The latter are higher in K, Fe, Ti and Al and lower in Na, Mg and Si.



Table 23 - EPM chemical data of the analysed biotites. All concentrations are in wt. %. Bt = biotite.

Sample	Mineral	#	Si	Ti	K	Ca	Mg	Fe	Mn	Na	Cr	Al	O	Total
LB106A	Bt	56	17.62	0.85	6.90	0.02	9.57	9.43	0.04	0.19	b.d.	9.08	39.21	92.90
LB106A	Bt	57	17.55	0.94	6.86	0.01	9.45	9.46	0.06	0.18	0.00	8.91	38.97	92.39
LB106A	Bt	88	17.88	0.86	6.74	0.04	9.97	9.28	0.05	0.21	0.02	9.11	39.77	93.95
LB106B	Bt	131	17.66	1.15	6.75	b.d.	9.20	10.29	0.05	0.19	0.00	8.98	39.34	93.61
LB106B	Bt	132	17.47	1.10	6.55	0.01	9.37	10.37	0.06	0.19	b.d.	9.05	39.25	93.41
LE9	Bt	150	16.70	1.64	7.55	b.d.	6.75	12.56	0.25	0.06	0.03	9.96	38.68	94.17
LE9	Bt	151	16.68	1.67	7.49	b.d.	6.60	12.89	0.23	0.02	0.03	9.78	38.48	93.88

Table 24 - Chemical formulae of the analysed biotites.

Sample	#	Mineral formula
LB106A	56-57	$(K_{0.79}Na_{0.03})(Mg_{1.75}Fe_{0.76}Ti_{0.09}Al_{0.31})(Al_{1.18}Si_{2.82})O_{10}(OH_2)$
LB106B	131-132	$(K_{0.76}Na_{0.04})(Mg_{1.70}Fe_{0.83}Ti_{0.10}Al_{0.26})(Al_{1.22}Si_{2.78})O_{10}(OH_2)$
LE9	150-151	$(K_{0.88}Na_{0.01})(Mg_{1.25}Fe_{1.04}Ti_{0.16}Al_{0.38})(Al_{1.29}Si_{2.71})O_{10}(OH_2)$

### 5.5.2. Amphibole

Table 25 contains the chemical data of all the analysed amphiboles. Amphiboles have a rather complex mineral structure. Therefore, several assumptions must be made to infer the chemical formula out of EPMA data. A formulation that works well for orthoamphiboles and cummingtonite is to normalise the total cations to 15 + Na + K. This way Na and K are only placed in the A site and Fe, Mg and Mn are maximally included into the M4 site (Veblen and Ribbe, 1982). There are, moreover, several substitutions that are possible in amphiboles that had to be taken into consideration. The chemical formulas (Table 26) show that edenite substitution occurred and replaced 0,35 (moles/unit) Si with Al in the T-site and additional Na in the A-site. The A-site is, moreover, is always less than 25% filled. Al is, beside the T-site, also substituted into the M-site, which is the result of Tschermak substitution ( $Al_2Mg_1Si_1$ ). The analysed orthoamphiboles classify within the anthophyllite-gedrite series. They are compositionally closer to anthophyllite as  $Fe > Al$ .

Table 25 - EPM chemical data of the analysed amphiboles. All concentrations are in wt. %. Ath = anthophyllite.

Sample	Mineral	#	Si	Ti	K	Ca	Mg	Fe	Mn	Na	Cr	Al	O	Total
LB106A	Ath	121	24.73	0.05	0.00	0.24	11.14	15.42	1.20	0.32	b.d.	2.08	42.36	97.54
LB106A	Ath	122	23.77	0.10	0.01	0.32	10.56	15.27	1.29	0.51	0.02	3.47	42.26	97.59
LB106B	Ath	123	23.20	0.14	0.00	0.41	10.28	15.55	0.73	0.69	b.d.	4.27	42.16	97.44
LB106B	Ath	124	23.25	0.14	b.d.	0.42	10.40	15.78	0.69	0.65	b.d.	4.19	42.27	97.78

Table 26 - Chemical formulae of the analysed amphiboles.

Sample	#	Mineral formula
LB106A	121-122	$(\text{Na}_{0.05})(\text{Na}_{0.08}\text{Ca}_{0.05}\text{Mn}_{0.20}\text{Fe}_{1.67})(\text{Fe}_{0.72}\text{Mg}_{3.88}\text{Al}_{0.40})(\text{Si}_{7.51}\text{Al}_{0.49})\text{O}_{22}(\text{OH})_2$
LB106B	123-124	$(\text{Na}_{0.19})(\text{Na}_{0.06}\text{Ca}_{0.09}\text{Mn}_{0.11}\text{Fe}_{1.74})(\text{Fe}_{0.71}\text{Mg}_{3.71}\text{Al}_{0.58})(\text{Si}_{7.21}\text{Al}_{0.79})\text{O}_{22}(\text{OH})_2$

### 5.5.3. Feldspar

Different feldspar grains were analysed in LB106A, LB106B and LE9 (Table 27). The chemical data was normalised to the ideal 5 cations to infer mineral formulae. All feldspars are plagioclases, for the K content of these feldspars is negligibly low. The plagioclases in LB106A and LB106B have 0.56 - 0.61 Na and 0.43 - 0.46 Ca per chemical formula unit, whereas LE9 possesses higher Na content, with 0.80 - 0.83 Na and 0.22 Ca per chemical formula unit. The feldspars in LB106A and LB106B are andesine and in LE9 classify as oligoclase (Figure 38). In all feldspar analyses Si and Al added up was lower than 3, which is the ideal stoichiometric situation for feldspars. This is possibly due to Si being measured slightly too low.

Table 27 - EPM chemical data of the analysed feldspars. All concentrations are in wt. %. Andes = andesine, Olg = oligoclase.

Sample	Mineral	#	Si	Ti	K	Ca	Mg	Fe	Mn	Na	Cr	Al	O	Total
LB106A	Andes	50	26.89	0.01	0.02	6.43	b.d.	0.03	0.01	5.12	b.d.	13.95	47.42	99.88
LB106A	Andes	51	26.88	0.00	0.02	6.51	b.d.	0.03	0.01	5.12	b.d.	14.05	47.51	100.12
LB106A	Andes	52	26.89	b.d.	0.03	6.36	0.00	0.05	b.d.	5.16	b.d.	13.99	47.43	99.89
LB106A	Andes	53	26.83	b.d.	0.03	6.48	0.00	0.03	0.01	5.04	b.d.	14.06	47.43	99.91
LB106A	Andes	54	26.68	0.00	0.02	6.47	0.00	0.04	0.00	5.15	b.d.	14.01	47.25	99.61
LB106A	Andes	55	26.83	b.d.	0.02	6.45	0.01	0.03	b.d.	5.11	b.d.	14.05	47.43	99.92
LB106B	Andes	125	26.48	b.d.	0.03	6.85	b.d.	0.05	b.d.	4.89	0.01	14.37	47.42	100.09
LB106B	Andes	126	26.65	b.d.	0.02	6.92	b.d.	0.05	b.d.	4.66	0.00	14.43	47.59	100.30
LB106B	Andes	133	26.52	b.d.	0.02	6.94	0.00	0.04	b.d.	4.78	0.01	14.45	47.52	100.27
LB106B	Andes	134	26.75	b.d.	0.02	6.58	b.d.	0.06	0.01	5.02	b.d.	14.17	47.48	100.08
LB106B	Andes	135	26.95	b.d.	0.06	6.49	b.d.	0.10	b.d.	5.02	b.d.	14.19	47.69	100.48
LB106B	Andes	136	26.69	b.d.	0.03	6.81	0.00	0.17	0.01	4.92	b.d.	14.24	47.56	100.42
LE9	Olg	154	29.56	b.d.	0.07	3.31	b.d.	0.05	b.d.	6.91	0.01	12.22	48.29	100.39
LE9	Olg	155	29.63	0.01	0.04	3.33	b.d.	0.05	b.d.	6.99	b.d.	12.29	48.46	100.77
LE9	Olg	156	29.52	b.d.	0.07	3.27	b.d.	0.02	0.01	7.20	b.d.	12.15	48.26	100.47
LE9	Olg	157	29.68	b.d.	0.07	3.28	0.00	0.02	0.00	6.99	0.01	12.22	48.45	100.72

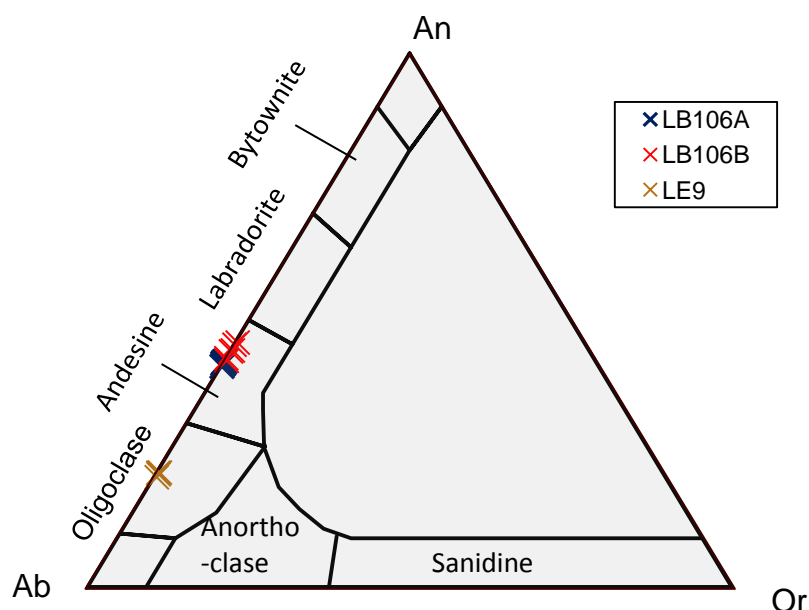


Figure 38 - Feldspar plot showing the composition of the analysed feldspars, Ab = albite, An = anorthite, Or = orthoclase.

#### 5.5.4. Garnet

The EPM data were normalised to 8 cations. The Fe-Mg-Ca-Mn content of the garnets (Table 28) implies that all garnets are classified as almandine. Stoichiometric ratios were checked to analyse the accuracy of the data. Si and Al should ideally add up to 5. All the garnets exhibit a slightly lower Al + Si, however. A likely explanation for this deviation is that Si was measured slightly lower than present in the minerals. Nonetheless, all garnets yield almandine composition with elevated Mg and Mn content. Chemical data of the garnets used for geothermometry are reported in Appendix B.

Table 28 - EPM chemical data of the analysed garnets. All concentrations are in wt. %. Alm = almandine.

Sample	Mineral	#	Si	Ti	K	Ca	Mg	Fe	Mn	Na	Cr	Al	O	Total
LB106A	Alm	46	17.75	0.01	b.d.	2.06	3.78	22.14	3.02	0.03	0.00	11.24	40.77	100.79
LB106A	Alm	47	17.87	0.01	0.00	1.84	3.88	22.02	2.99	0.01	0.01	11.31	40.91	100.86
LB106A	Alm	48	17.49	b.d.	0.00	1.72	2.45	22.05	5.71	0.01	b.d.	11.15	40.12	100.70
LB106A	Alm	49	17.45	0.00	b.d.	1.78	2.23	22.70	5.57	b.d.	b.d.	11.07	40.03	100.82
LB106B	Alm	143	17.81	b.d.	b.d.	1.84	3.40	22.81	3.39	b.d.	b.d.	11.22	40.77	101.24
LB106B	Alm	144	17.69	0.01	b.d.	2.00	2.82	24.09	3.28	b.d.	b.d.	11.16	40.60	101.65

#### 5.5.5. Fibrolite

The analysed fibrolites of LE9 are not purely composed of  $Al_2SiO_5$ . Instead, additional K, Mg, Fe and Ti are present (Table 29). The total weight percentage is 95.26%, indicating the presence of elements that are unable to be measured with EPM, such as OH-groups. Fibrolite intergrown with biotite

explains the described composition and is a commonly found intergrowth (Tozer, 1955; Woodland, 1963; Best & Weiss, 1964; Grambling, 1981). Ratio calculations with the average composition of biotite in LE9 and ideal sillimanite composition result in the ratio sillimanite / (biotite + sillimanite) = 0.24.

*Table 29 - EPM chemical data of the analysed fibrolites. All concentrations are in wt. %. Sil = sillimanite, Bt = biotite.*

Sample	Mineral	#	Si	Ti	K	Ca	Mg	Fe	Mn	Na	Cr	Al	O	Total
LE9	Sil (+Bt)	148	21.23	0.70	7.86	b.d.	0.47	2.50	0.02	0.26	0.03	18.41	43.78	95.26
LE9	Sil (+Bt)	149	21.25	0.66	7.79	b.d.	0.49	2.41	0.02	0.23	0.02	18.45	43.77	95.08

### 5.5.6. Opaques

The measured opaques in LB106A and LB106B are magnetite and ilmenite. The analysed opaques in LE9 are both magnetite (Table 30).

*Table 30 - EPM chemical data of the analysed fibrolites. All concentrations are in wt. %. Ilm = ilmenite, Mt = magnetite.*

Sample	Mineral	#	Si	Ti	K	Ca	Mg	Fe	Mn	Na	Cr	Al	O	Total
LB106A	Ilm	60	0.00	30.54	0.00	0.04	0.18	36.79	1.59	0.00	b.d.	0.01	31.56	100.72
LB106A	Ilm	61	0.02	30.29	0.00	0.06	0.15	37.11	1.69	b.d.	0.01	0.02	31.53	100.88
LB106A	Ilm	62	0.02	30.01	0.02	0.02	0.06	37.08	1.52	0.01	b.d.	0.02	31.20	99.95
LB106B	Ilm	127	0.01	30.73	b.d.	0.01	0.32	37.42	0.87	b.d.	0.04	0.02	31.77	101.18
LB106B	Ilm	128	0.02	30.46	0.01	0.00	0.36	37.69	0.79	b.d.	0.02	0.02	31.66	101.01
LB106B	Ilm	129	0.01	30.88	0.00	0.02	0.36	36.84	0.98	b.d.	0.05	0.02	31.76	100.92
LB106B	Ilm	130	0.00	30.95	0.00	0.01	0.32	37.07	1.02	b.d.	0.03	0.01	31.84	101.25
LB106A	Mt	58	0.02	0.01	0.01	0.01	b.d.	72.42	0.03	0.02	0.03	0.09	20.88	93.51
LB106A	Mt	59	0.00	0.02	0.00	0.00	0.00	72.65	0.02	0.02	0.03	0.09	20.94	93.77
LB106A	Mt	63	0.01	0.56	0.02	0.02	0.02	72.31	0.02	0.01	0.14	0.04	21.23	94.37
LB106B	Mt	137	0.01	0.02	b.d.	0.00	b.d.	72.25	0.01	b.d.	0.03	0.07	20.80	93.18
LE9	Mt	152	0.01	0.00	b.d.	b.d.	0.00	72.64	0.04	b.d.	0.23	0.09	21.02	94.02
LE9	Mt	153	b.d.	0.01	0.01	0.00	b.d.	72.39	0.03	b.d.	0.21	0.08	20.92	93.64

### 5.5.7. Chlorite

In LB106A 6 spots of a potential cordierite grain are measured. This particular grain turned out to be chlorite (Table 31). Chl = chlorite.

Table 31 - EPM chemical data of the analysed chlorite. All concentrations are in wt. %.

Sample	Mineral	#	Si	Ti	K	Ca	Mg	Fe	Mn	Na	Cr	Al	O	Total
LB106A	Chl	158	12.87	0.02	0.00	0.01	13.74	10.61	0.14	0.01	0.01	11.64	37.17	86.23
LB106A	Chl	159	12.78	0.03	0.00	0.01	13.59	10.69	0.13	b.d.	0.00	11.46	36.82	85.50
LB106A	Chl	160	12.61	0.03	0.02	0.03	13.70	10.55	0.08	0.01	0.02	11.92	37.09	86.06
LB106A	Chl	161	12.53	0.01	0.01	0.01	13.62	10.77	0.13	0.00	0.02	11.83	36.91	85.85
LB106A	Chl	162	12.86	0.03	0.26	0.03	13.00	10.70	0.10	0.01	0.01	12.04	37.10	86.13
LB106A	Chl	163	12.53	0.03	0.03	0.02	13.37	10.62	0.10	b.d.	0.00	12.09	36.94	85.74

## 6. Discussion

### 6.1. Peak metamorphic conditions

#### 6.1.1. Pseudosections

The program *Perple\_X* was used for the computation of pseudosections. These pseudosections contribute in the determination of the peak pressure and temperature during the metamorphism of the Sara's Lust Gneisses. In the *Perple\_X* modelling, phosphorous was excluded. As a consequence, apatite was not incorporated in the computation of the pseudosections. Bulk rock calcium content was corrected for every sample due to absent apatite in the model. For the other samples, saturated H<sub>2</sub>O and SiO<sub>2</sub> was assumed, the former because hydrated minerals are present in all samples, the latter because quartz is present in all samples. Because LE9 is a metasediment, a solution model for melt was included, for metasediments have a lower melting temperature. Specifying H<sub>2</sub>O as a saturated phase in a model including a melt phase is not possible in the used *Perple\_X* version. For this reason, the H<sub>2</sub>O content of LE9 was estimated on 7 wt. %. Carbonate fluids were excluded for they were assumed to only play a minor role in the metamorphic evolution; carbonate minerals are only present as secondary phases. Further, Fe(III) content was calculated for each sample based on mineral compositions and the abundances of Fe(II)- and Fe(III)-bearing minerals. The eventual pseudosection computations were conducted with the following percentages of Fe(III) out of total iron content: 15% for LB106A, 15% for LB106B, 19% for LB106B1, 11% for LB106B2 and 29% for LE9. Mn content was modified for anthophyllite because EPM data revealed that anthophyllite contains some Mn (Table 25), whereas the solution model for orthoamphibole does not include Mn. The corrections in Mn concentrations were based on the estimated volume percentage of orthoamphibole and Mn content of anthophyllite. For LB106B, two pseudosections were computed as two significantly different lithologies were present (Figures 41 and 42). The bulk rock composition was split based on estimated volume percentage, EPM data on mineral compositions and bulk rock chemistry (Table 32).

*Table 32 - Calculation of the major element composition of the two different lithologies of LB106B. A ratio between the lithologies is estimated on a 35 / 65 ration basis. The calculated composition is normalised to the XRF data of LB106B to analyse the deviation of the calculated composition. The red values in the last column show the deviating calculated composition values.*

Oxide	Calculated composition	Bulk rock chemistry (XRF)	Calculated compositions / XRF data
Al <sub>2</sub> O <sub>3</sub>	14.41	15.17	0.95
CaO	4.59	6.23	0.74
FeO	8.44	7.41	1.14
K <sub>2</sub> O	0.98	1.01	0.97
MgO	4.44	4.27	1.04
MnO	0.20	0.18	1.13
Na <sub>2</sub> O	1.80	1.40	1.29
SiO <sub>2</sub>	64.19	61.02	1.05
TiO <sub>2</sub>	0.94	0.85	1.11

Using a ratio of 65 / 35 between the two lithologies, based on petrographic estimations, all oxides of the combined lithologies are close to the bulk rock chemistry (all within a range of 14%), except for CaO and Na<sub>2</sub>O. These deviations can be explained with three theories: 1) The calculated composition in these oxides differ from XRF data due to alteration. The presence of secondary carbonates could cause an increase in measured CaO content and K<sub>2</sub>O. The lower Na<sub>2</sub>O content could be caused by the loss of mobile elements during fluid interactions. However, other mobile elements such as K<sub>2</sub>O would also be expected to be lost, which is not the case according to the calculated composition. 2) Plagioclase differ in composition. If a substantial amount of plagioclases are more anorthitic than the plagioclase composition used in the calculation, CaO content would be higher and Na<sub>2</sub>O would be lower, which is in better agreement with the XRF data. Yet, the plagioclase grains analysed with EPM in LB106B all yielded similar CaO and Na<sub>2</sub>O content (Figure 38). 3) The XRF data is inaccurate. Possibly, an interplay of some of the named theories caused the slightly differing recalculated CaO and Na<sub>2</sub>O composition. This might cause the computation of unrepresentative pseudosections. Consequently, an additional bulk rock pseudosection was computed for LB106B (Figure 40). This pseudosection assumes equilibrium on bulk rock scale with sufficing diffusion rates.

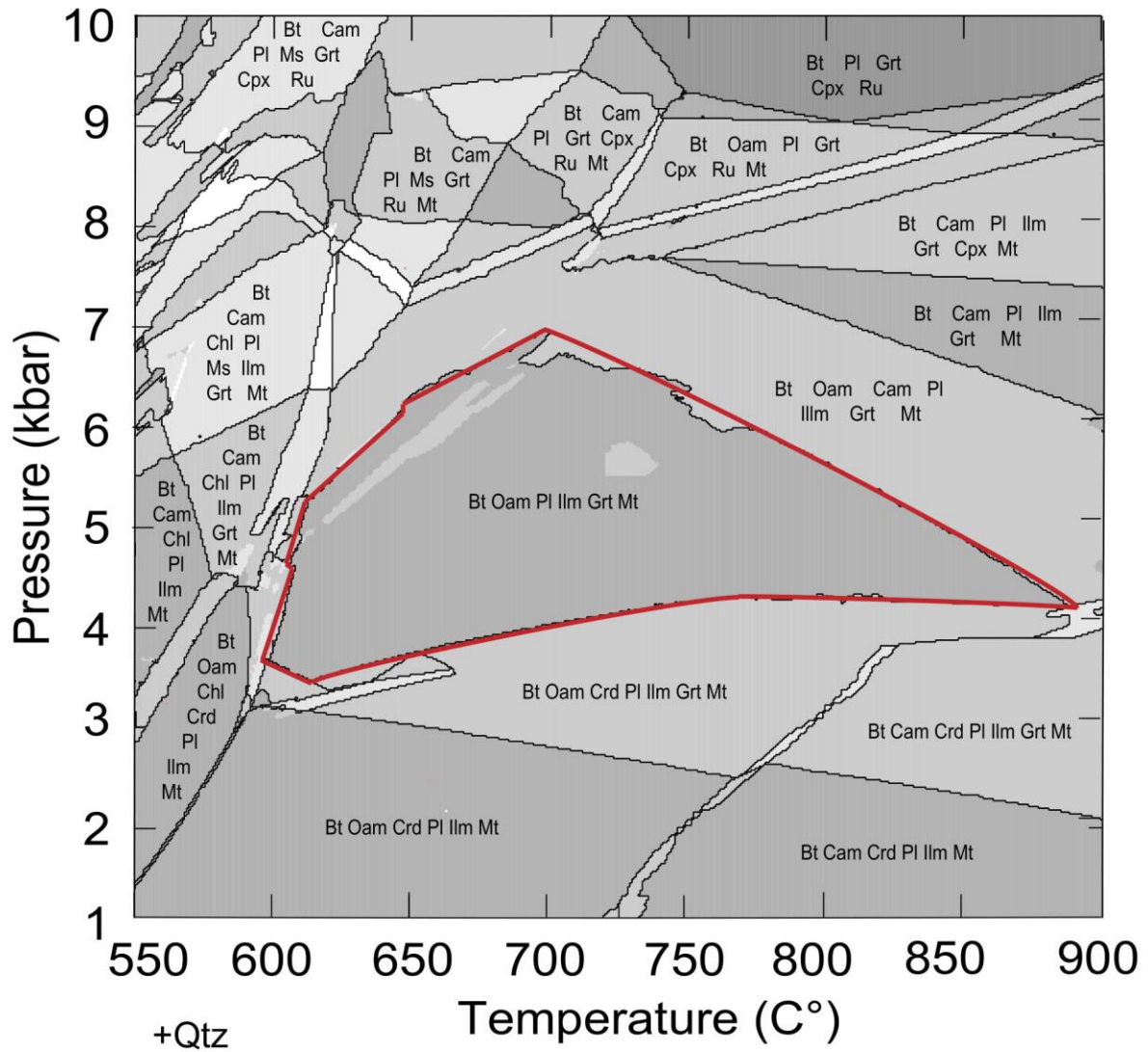


Figure 39 - Pseudosection for LB106A. The stable mineral assemblage is highlighted with a red outline. Mineral abbreviations: Bt = biotite, Cam = clinoamphibole, Chl = chlorite, Cpx = clinopyroxene, Crd = cordierite, Grt = garnet, Ilm = ilmenite, Ms = muscovite, Oam = orthoamphibole, Pl = plagioclase, Qtz = quartz, Ru = rutile.

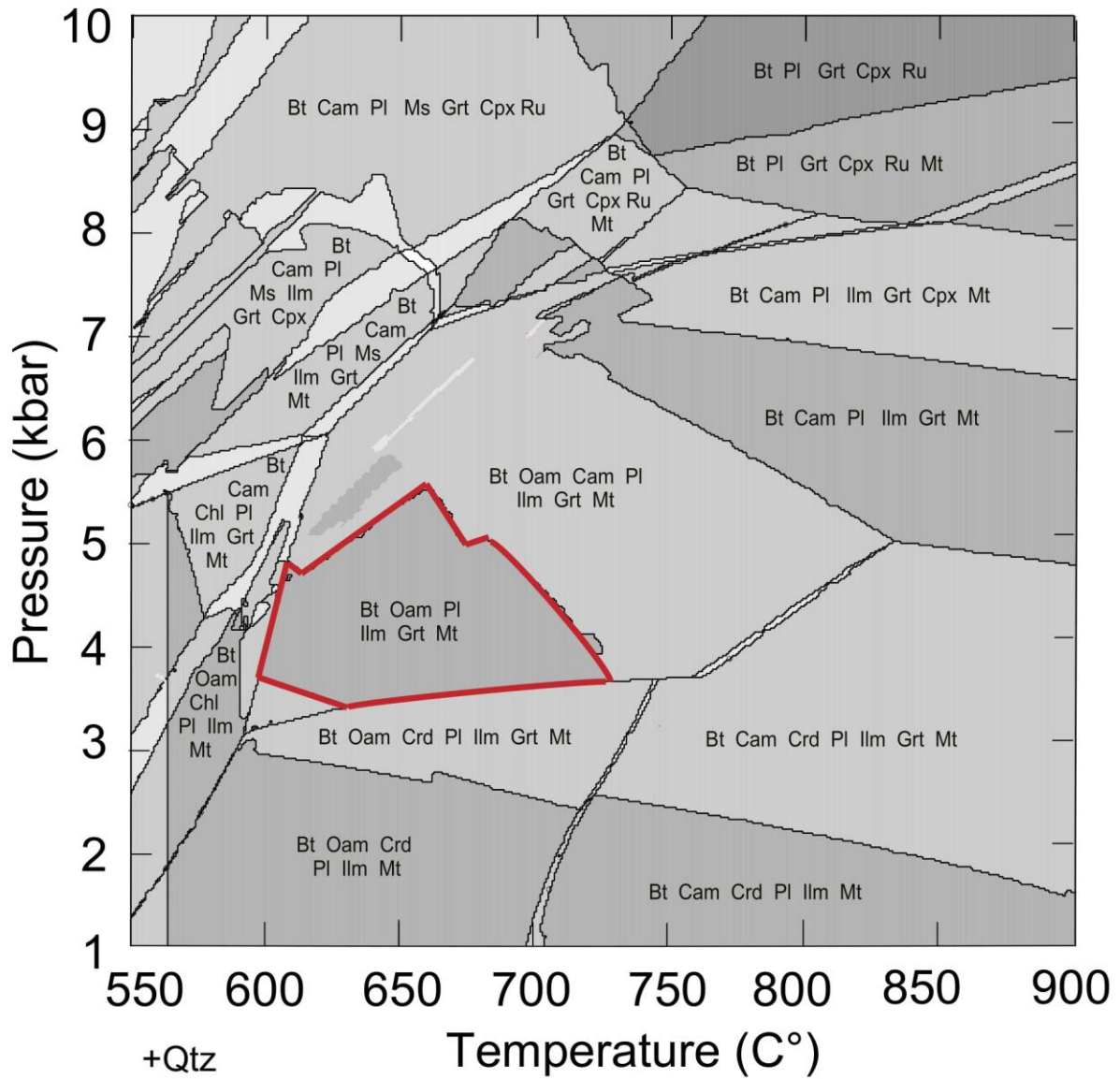


Figure 40 - Pseudosection for LB106B. The stable mineral assemblage is highlighted with a red outline. Mineral abbreviations: Bt = biotite, Cam = clinoamphibole, Chl = chlorite, Cpx = clinopyroxene, Crd = cordierite, Grt = garnet, Ilm = ilmenite, Ms = muscovite, Oam = orthoamphibole, Pl = plagioclase, Qtz = quartz, Ru = rutile.



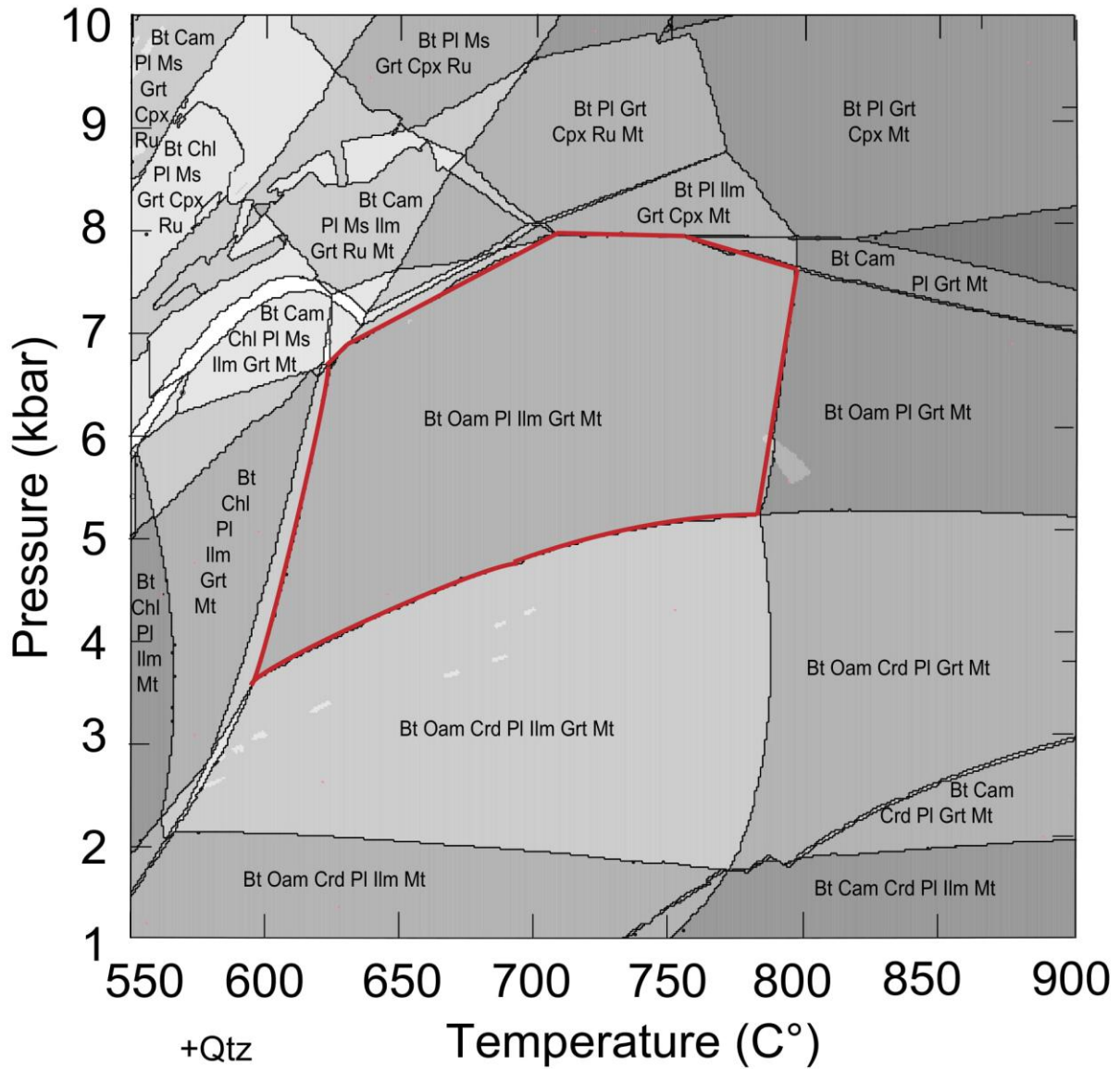


Figure 41 - Pseudosection for LB106B1. The stable mineral assemblage is highlighted with a red outline. Mineral abbreviations: *Bt* = biotite, *Cam* = clinoamphibole, *Chl* = chlorite, *Cpx* = clinopyroxene, *Crd* = cordierite, *Grt* = garnet, *Ilm* = ilmenite, *Ms* = muscovite, *Oam* = orthoamphibole, *Pl* = plagioclase, *Qtz* = quartz, *Ru* = rutile.

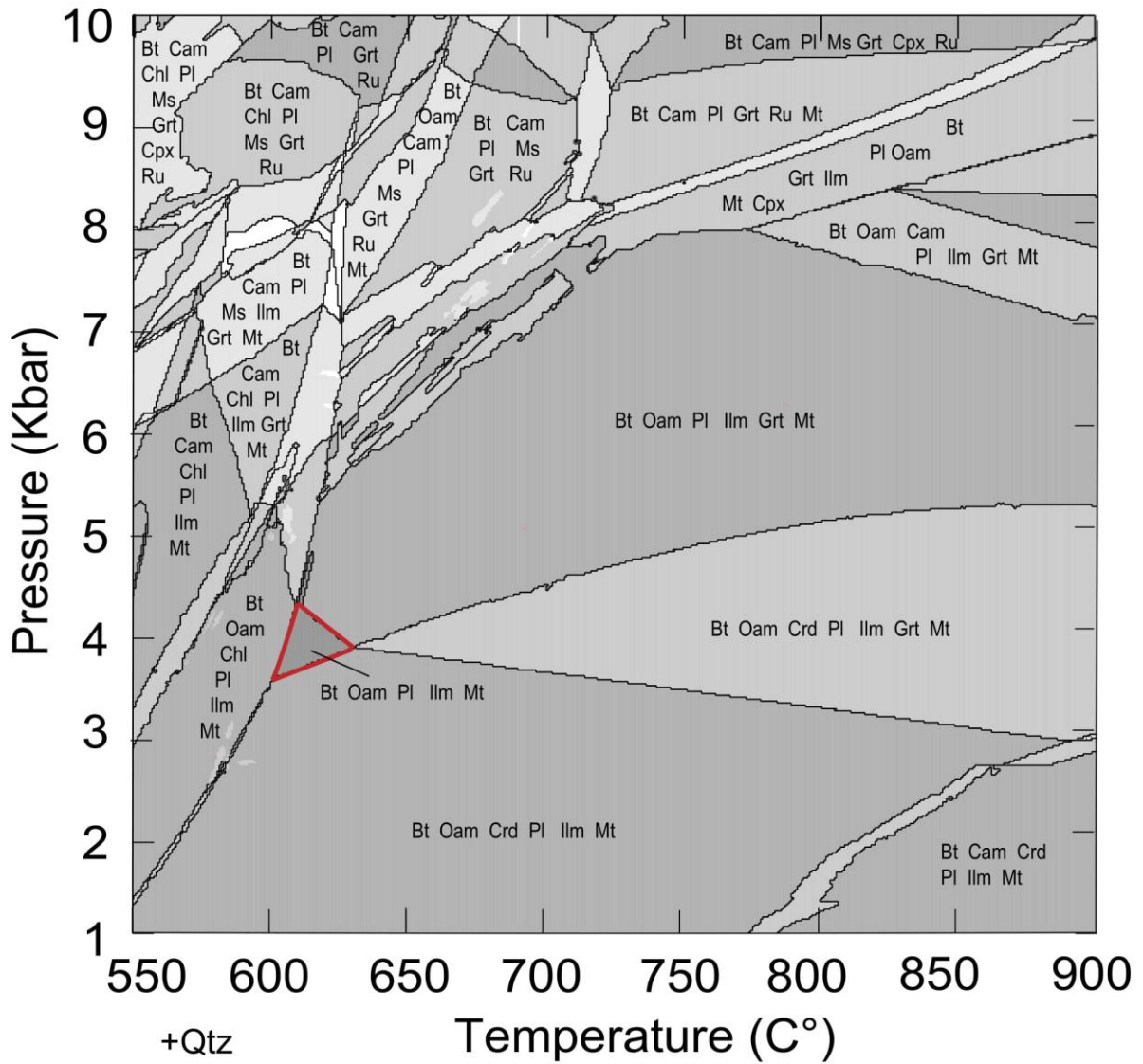


Figure 42 - Pseudosection for LB106B2. The stable mineral assemblage is highlighted with a red outline. Mineral abbreviations: Bt = biotite, Cam = clinoamphibole, Chl = chlorite, Cpx = clinopyroxene, Crd = cordierite, Grt = garnet, Ilm = ilmenite, Ms = muscovite, Oam = orthoamphibole, Pl = plagioclase, Qtz = quartz, Ru = rutile.

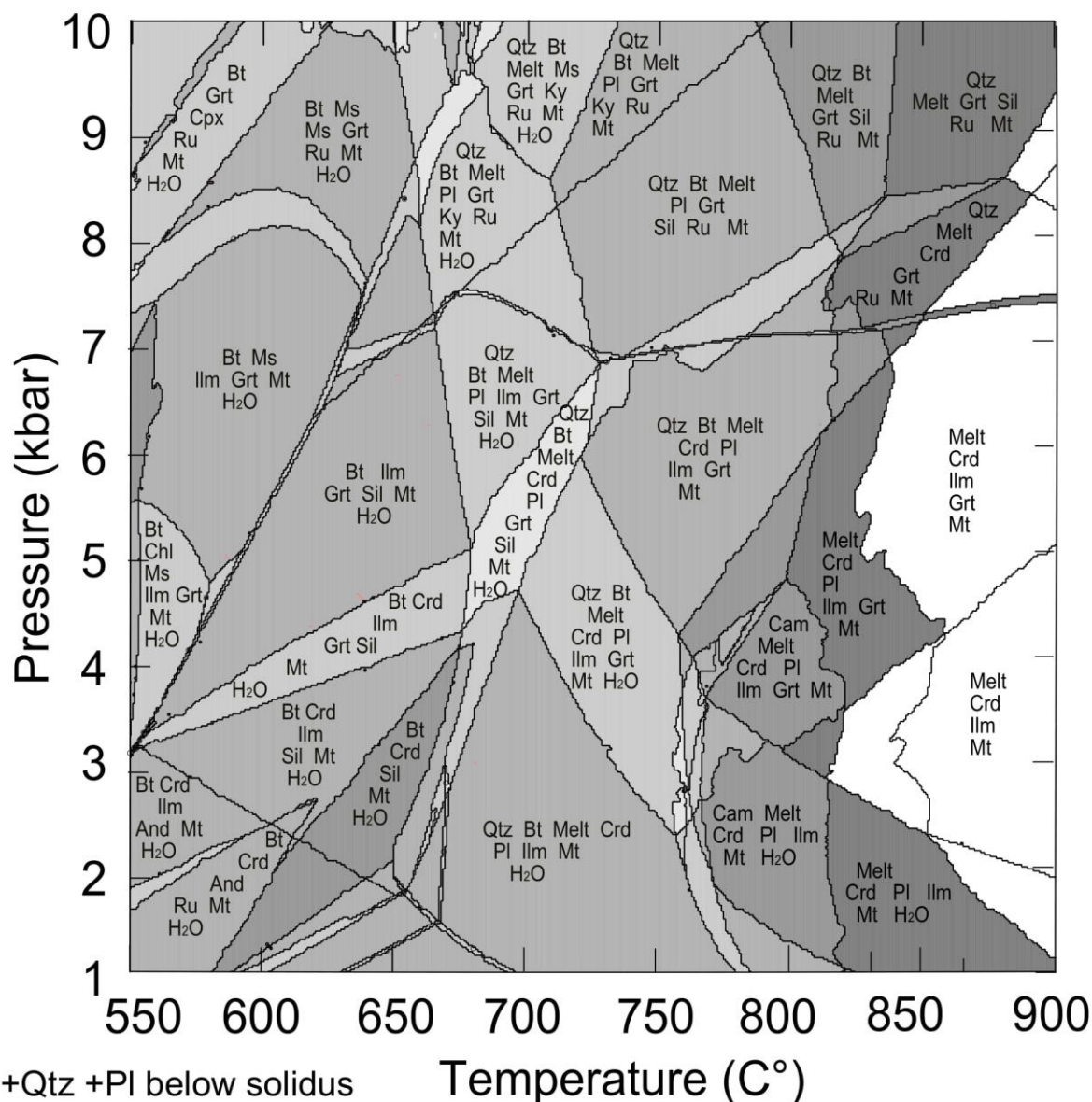


Figure 43 - Pseudosection for LE9. The stable mineral assemblage is highlighted with a red outline. Mineral abbreviations: Bt = biotite, Cam = clinoamphibole, Chl = chlorite, Cpx = clinopyroxene, Crd = cordierite, Grt = garnet, Ky = kyanite, Ilm = ilmenite, Ms = muscovite, Oam = orthoamphibole, Pl = plagioclase, Qtz = quartz, Ru = rutile, Sil = sillimanite.

The mineral assemblages of LB106A, LB106B, LB106B1 and LB10B2 are present in a stability field in their corresponding pseudosection (Figures 39 - 43). The mineral assemblage of LE9, with both garnet and cordierite excluded, is not present in the computed pseudosection (Figure 43). Garnet becomes stable towards higher pressures as soon as cordierite becomes unstable, leaving no area in PT-space where both minerals are absent. For this reason, isopleths for garnet and cordierite abundances were computed in which 1 wt. % of garnet and cordierite was allowed (Figure 49). This resulted in the deduction of a peak pressure of  $5.5 \pm 1$  kbar and a peak temperature of  $688 \pm 50$  °C (see

Section 6.1.3 for further elaboration). These metamorphic conditions correlate with the stability field of Qtz, Bt, Melt, Crd, Pl, Grt, Sil, Mt. In the thin section of LE9, no indications for melting were observed. However, migmatization in the Sara's Lust Gneisses had been observed in the field (Bosma et al., 1983, 1984). Possibly, LE9 underwent metamorphism with conditions up to the solidus, where other Sara's Lust metasediments, as observed in the field, reached pressures and temperatures taking these rocks beyond the solidus leading to migmatization. Thence, the abovementioned derived mineral assemblage, with the marginal allowance of cordierite, garnet and melt, is most representative for LE9.

### 6.1.2. Geothermometry

For further constraints on peak pressures and temperatures the garnet-biotite exchange geothermometer of Ferry & Spear (1978) was used. This thermometer uses the exchange reaction of iron and magnesium between almandine and phlogopite and between pyrope and annite. The first thermometer from the abovementioned authors assumed ideal mixing and did not incorporate the effect of Ca and Mn content in garnet and Al(VI) and Ti content in biotite. Kleemann and Reinhardt (1994) proposed that the effect of Al(VI) and Ti content in biotite is significant on Fe and Mg exchange, and thus the outcome of the garnet-biotite thermometer, and construed a new thermometer. They furthermore included Margule mixing parameters for garnets to encompass the non-ideal effect of Ca and Mn abundances in garnet for their geothermometer. This resulted in the following formula:

$$T [C^{\circ}] = \frac{20253 + \Delta W_H^{Grt} + 77785 X_{Al}^{Bt} - 18138 X_{Ti}^{Bt} + (\Delta V^0 + \Delta W_V^{Grt}) P}{10.66 - R \ln K_D + \Delta W_S^{Grt} + 94.1 X_{Al}^{Bt} - 11.7 X_{Ti}^{Bt}} - 273$$

$\Delta W_H$ ,  $\Delta W_V$  and  $\Delta W_S$  are the Margule mixing parameters for garnet,  $X^{Bt}$  is the concentration of a particular element in biotite, with Al only including octahedral Al,  $\Delta V^0$  is the standard molar volume change, P is the pressure in bar, R is the gas constant and  $K_D$  is the distribution coefficient of Mg and Fe in garnet and biotite. The  $2\sigma$  deviation of this geothermometer is  $\pm 28$  °C. The usage of this thermometer shows several complications, as discussed in the next sections.

#### 6.1.2.1 Biotite complications for geothermometry

The Fe and Mg content of biotite and garnet can be affected by retrograde re-equilibration. Especially biotite is prone to retrograde re-equilibration for diffusion rates are high in biotite. Spear (1993) states that biotite grains in contact with garnets can change most in composition during retrogradation. Retrograde re-equilibrium is, however, more significant in high-grade metamorphic rocks. Retrograde diffusion in medium-grade rocks, such as the Sara's Lust Gneisses, is substantially slower because temperatures were lower during metamorphism and diffusion is temperature-dependent. Selecting a biotite in contact with a garnet gives a higher certainty of the two minerals having chemically

equilibrated. Therefore, biotite grains in contact with garnets were selected for geothermometric calculations.

Additionally, retrograde biotite grains were not affected by Fe and Mg exchange reactions during peak metamorphic conditions. These are, therefore, preferably not used for the garnet-biotite thermometer. Instead, prograde biotite grains were selected for geothermometry.

#### *6.1.2.2. Garnet complications for geothermometry*

Regarding the composition of garnet, a garnet can display chemical zoning due to relatively slow diffusion rates in an individual grain. The question then arises whether to use the composition of the rim or the core of the garnet. Zoning in a garnet can occur due to two different processes: 1) garnet growth at relatively low pressure and temperature results in different compositions between core and newly grown rim material. As a consequence of slow diffusion rates, the garnet cannot homogenise and chemical zoning will occur. Rim compositions are preferably used for geothermometric calculations in this scenario. 2) Garnet growth at relatively high pressures and temperatures will result in a homogeneously composed garnet. Zoning can then form due to retrograde reactions altering the composition of the garnet rims. In this case, the composition of the garnet core is used for geothermometry. A distinction between the two different zoning processes can be made on the basis of a chemical profile through the garnets (Figure 44). The garnet from LB106A exhibits a chemical profile pattern where in the rim of the garnet Mg is slightly lower and Fe is slightly higher. The composition of garnet remains constant, except for an increase in Mn content in the rim. This indicates retrograde alteration of the rim and, therefore, the core composition was taken for geothermometric calculations. The garnet from LB106B exhibits a different chemical profile pattern, with Mn increasing and Fe decreasing gradually towards the core of the garnet. This pattern indicates prograde zoning and the rim composition was used for geothermometry.

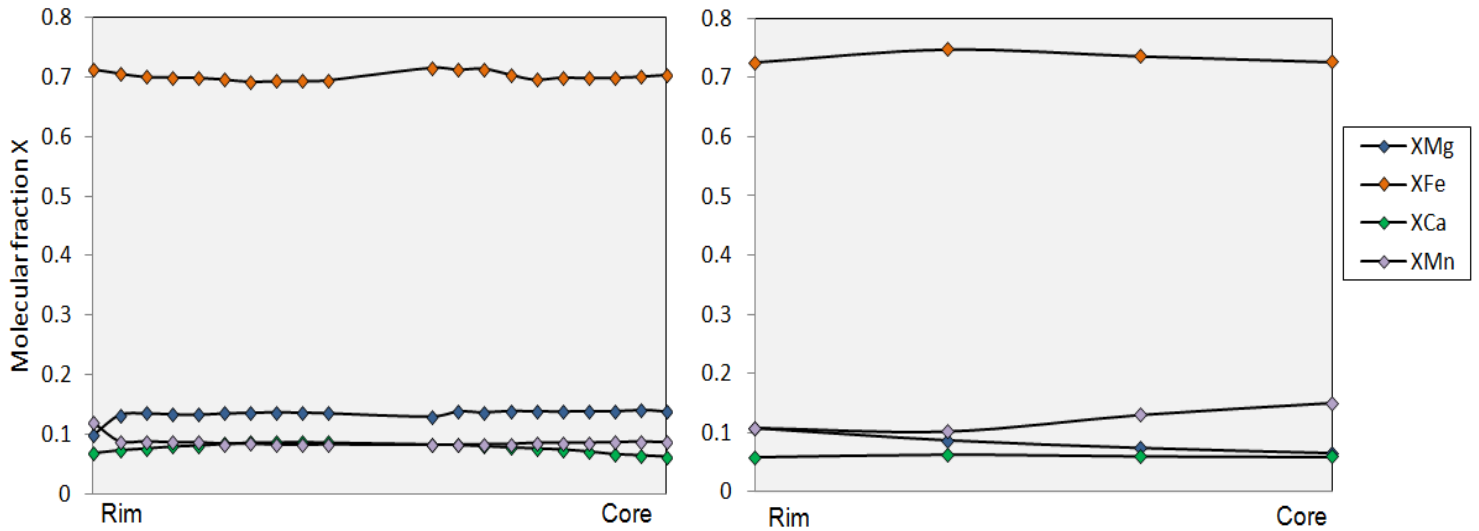


Figure 44 - Chemical cross profiles of a garnet from LB106A (left diagram) and from LB106B (right diagram).

### 6.1.2.3. Pressure-Temperature relationship

Berman's (1990) model for the mixing properties of garnet was used for the Margule parameters ( $W_H$ ,  $W_S$  and  $W_V$ ) for garnet. This model assumes near-ideal mixing for quaternary Fe-Mg-Ca-Mn garnets and is based on the interaction activities between these four cations. The garnets from LB106A and LB106B have lowest Ca content (Table 28), hence the corresponding Margule parameters for garnet are  $W_{HGt} = 1975$ ,  $W_{VGt} = 0.035$ ,  $W_{SGt} = 0$  (Berman, 1990). Moreover, according to Kleemann and Reinhardt (1994),  $\Delta V^0$  of a biotite from the pure annite-phlogopite series is between 0.100 - 0.108. An average of 0.104 was taken. This allows the calculation of a pressure-temperature relationship for the garnet-bearing samples LB106A and LB106B1, with pressure in kbar.

$$\text{LB106A: } T = 617 + 4.2 \cdot P (\pm 28 \text{ }^\circ\text{C})$$

$$\text{LB106B(1): } T = 572 + 4.3 \cdot P (\pm 28 \text{ }^\circ\text{C})$$

As illustrated in Figures 44 - 46 (Section 6.1.3.), the derived pressure-temperature relationships are in consistency with the metamorphic conditions derived from the pseudosections and isopleths of LB106A and LB106B(1).

### 6.1.3. Peak pressure and temperature

The abovementioned pressure-temperature relationships, together with the representative stability field obtained from the pseudosections are combined with abundance and composition isopleths of anthophyllite, biotite, cordierite, garnet and plagioclase to infer peak pressure and temperature (Figures 45 - 49). Only the relevant isopleths that give further implications for peak metamorphic conditions are displayed. The peak metamorphic conditions in the figures below were derived by

determining the overlapping area or point of the pseudosections, isopleths and the garnet-biotite geothermometer.

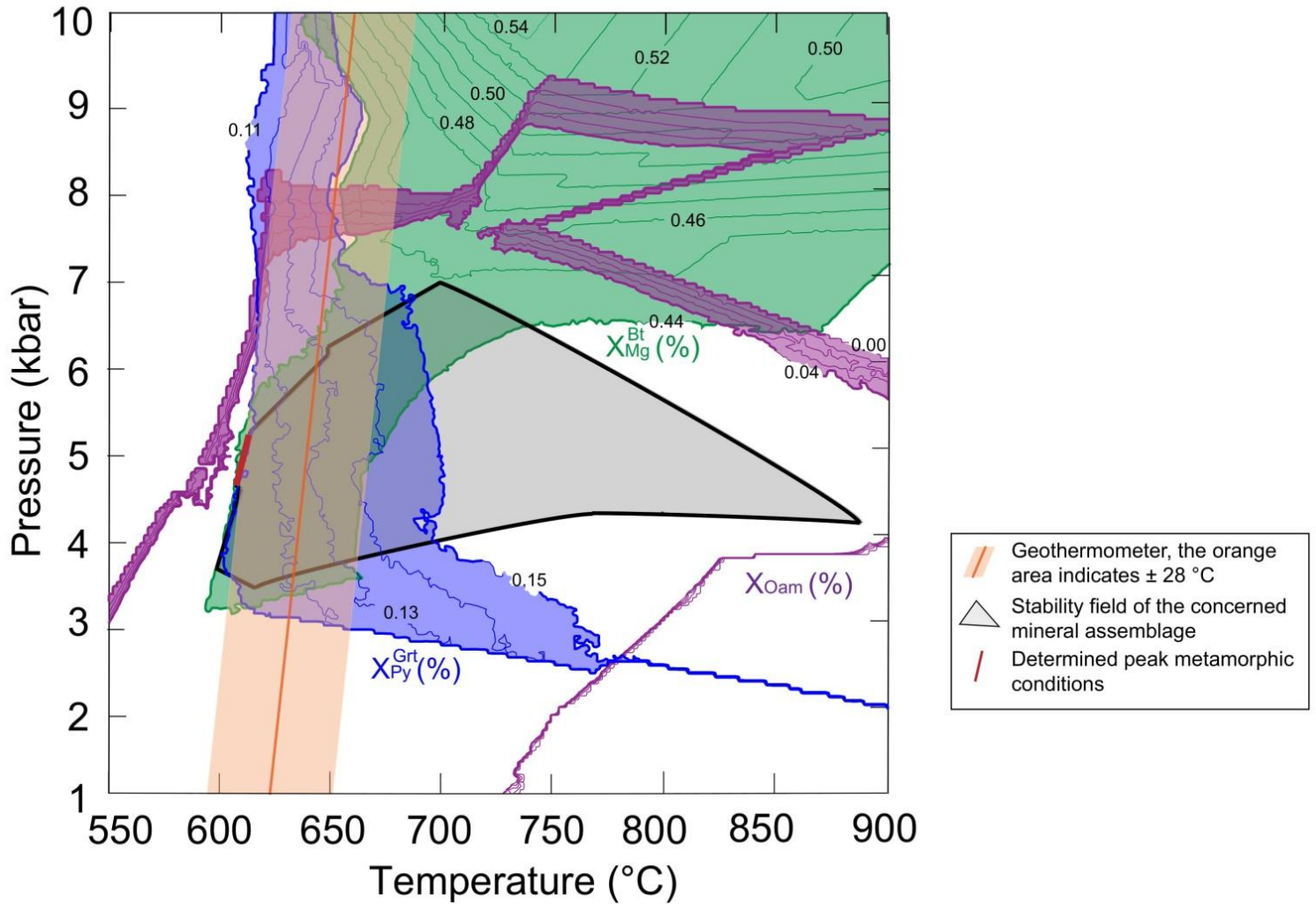


Figure 45 - Combined pseudosection, isopleths and garnet-biotite geothermometer information in PT-space for LB106A.

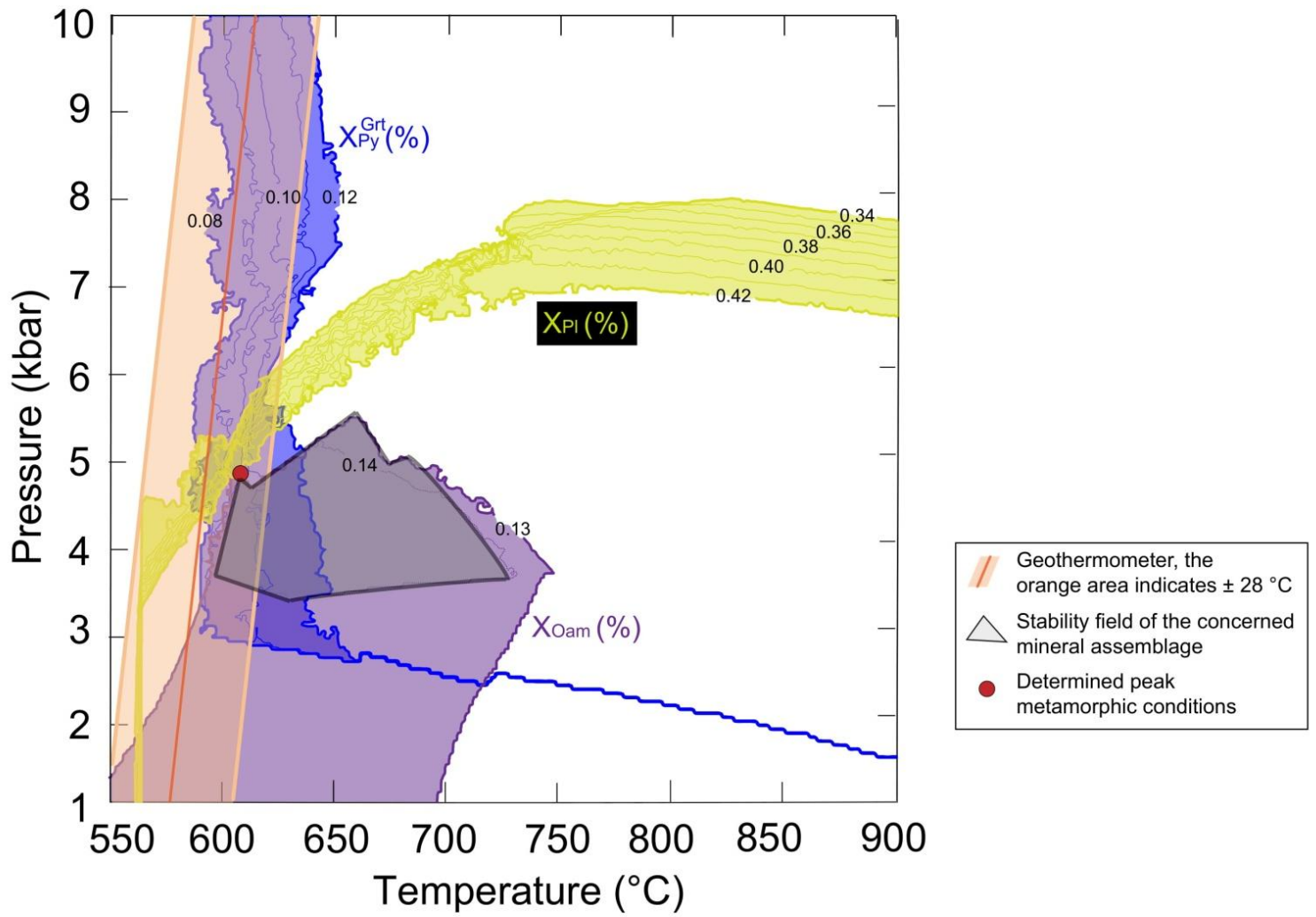
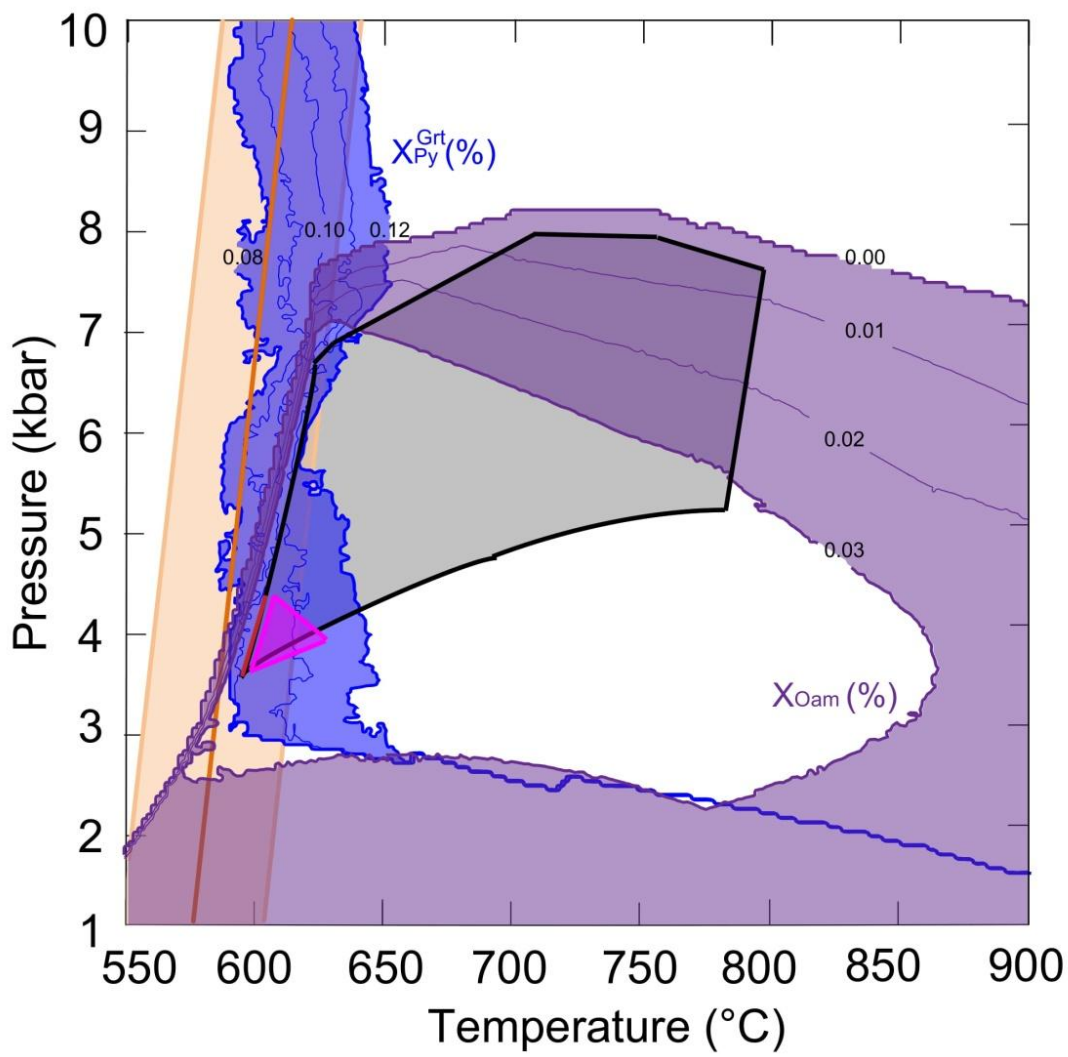


Figure 46 - Combined pseudosection, isopleths and garnet-biotite geothermometer information in PT-space for LB106B.









-  Geothermometer, the orange area indicates  $\pm 28^\circ\text{C}$
-  Stability field of the concerned mineral assemblage
-  Determined peak metamorphic conditions of LB106B2
-  Determined peak metamorphic conditions

Figure 47 - Combined pseudosection, isopleths and garnet-biotite geothermometer information in PT-space for LB106B1.

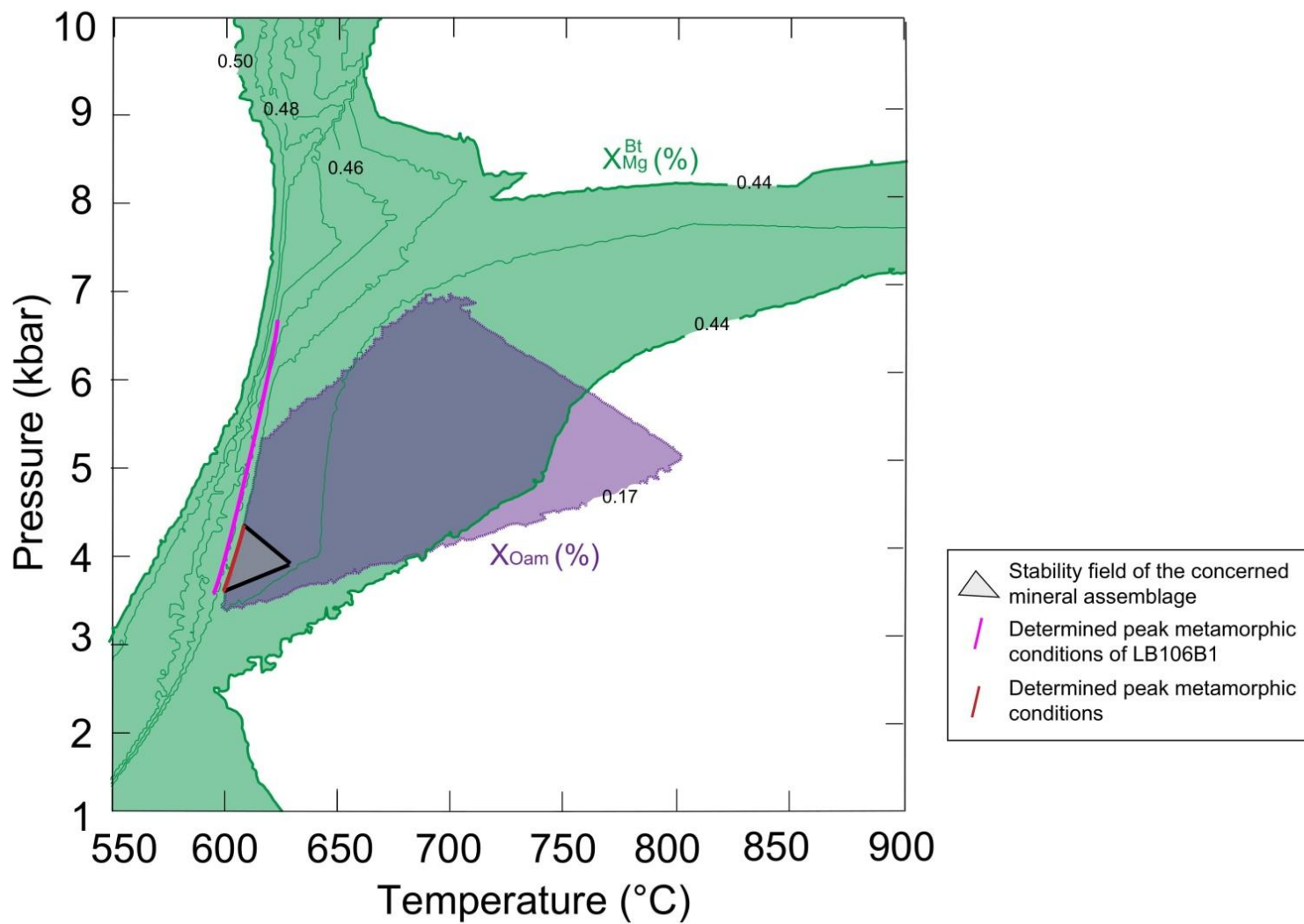


Figure 48 - Combined pseudosection and isopleths information in PT-space for LB106B2.

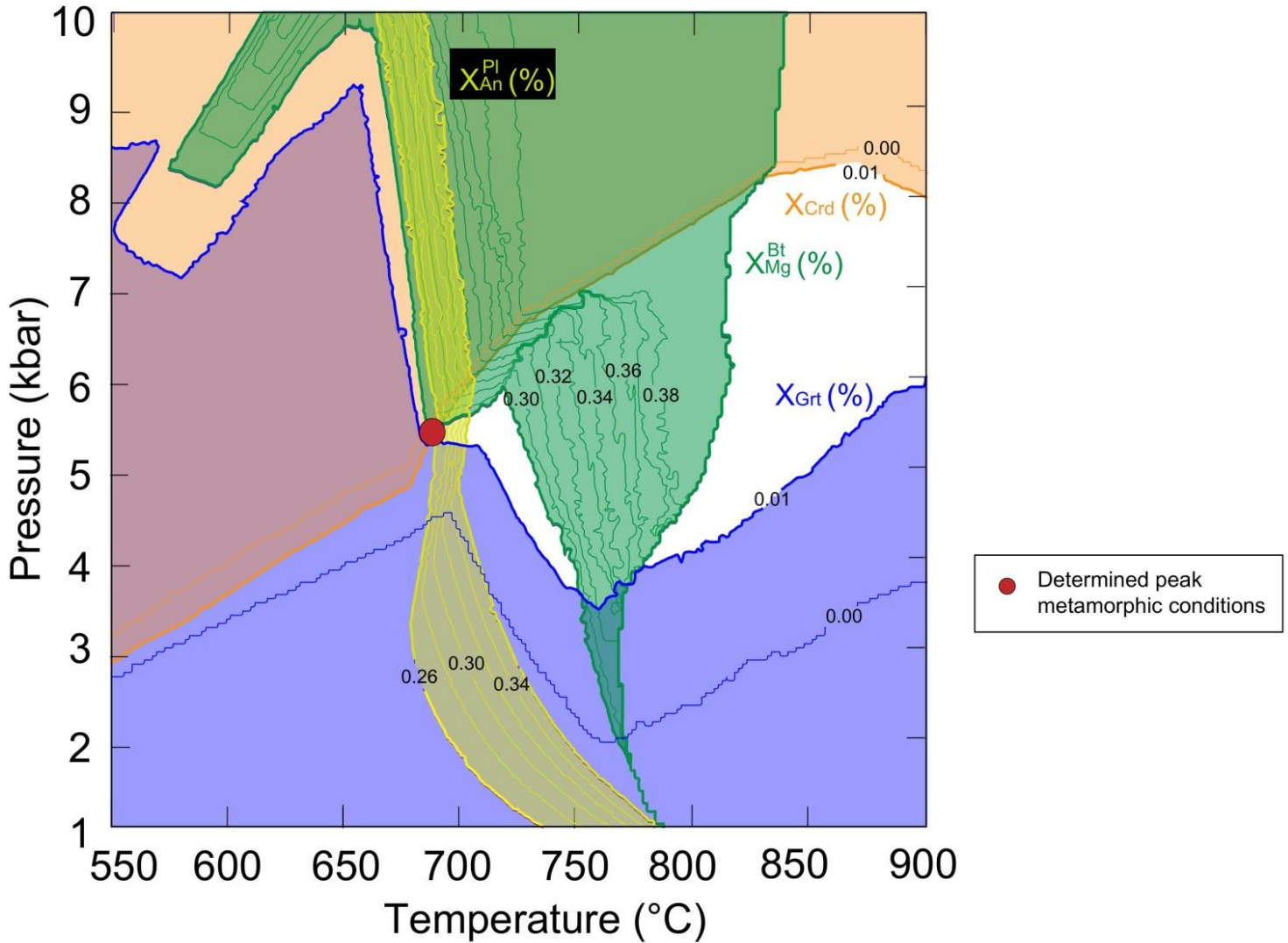


Figure 49 - Combined pseudosection and isopleths information in pressure-temperature space for LE9. The presence of up to 1 wt.% of garnet and cordierite was allowed in the construction of this figure.

A maximum deviation of 10% from the observed mineral abundances and measured element concentrations was allowed in Figure 45 - 49. Because the pseudosections and isopleths of LB106B1 and LB106B2 originate from the same rock, metamorphic conditions must have been the same. The overlap of both determined pressure and temperature conditions further restricts the possible metamorphic conditions for LB106B, as indicated in pink in Figures 47 and 48. The constraints of metamorphic conditions of LB106B1 and LB106B2 combined give a peak pressure of 3.6 - 4.4 ( $\pm 1$ ) kbar and peak temperature of 592 - 622 ( $\pm 50$ ) °C. For this derivation, isopleths for plagioclase composition and abundance were not used because they were inconsistent with the petrographic observations and analysed mineral chemistry. The calculated plagioclase was more albitic compared to the EPM data. Moreover, #Mg of biotite and anthophyllite were also deviant compared to the EPM

data. These dissimilarities may indicate that the calculation of the differing lithologies within LB106B is not entirely representative. In comparison with the bulk computation of LB106B, the deduced peak pressure is lower. In contrast, the isopleths and mineral stability field of LB106B were in agreement with the observed and analysed mineral abundances and compositions. Therefore, the bulk computation was preferred for the determination of peak metamorphic conditions for LB106B (Figure 46).

Withal, the determined peak metamorphic conditions of the Sara's Lust Gneisses show a range, with pressures of 4.6 - 5.5 ( $\pm 1$ ) kbar and temperatures of 617 - 688 ( $\pm 50$ ) °C. Pressure and temperature uncertainty ranges were based on Spear (1993). Table 33 below gives a summary on minimum and maximum peak pressure and temperature for each sample.

*Table33 - Summary of the determined peak pressure and temperature for LB106A, LB106B1, LB106B2 and LE9.*

Sample	Peak pressure in kbar ( $\pm 1$ kbar)	Peak temperature in °C ( $\pm 50$ °C)
LB106A	4.6 - 5.3	620 - 628
LB106B	4.9	617
LB106B1	3.6 - 4.4	598 - 637
LB106B2	3.6 - 6.7	592 - 622
LE9	5.5	688

In the northern section of the Sara's Lust Gneisses, metamorphic conditions have been reported to be up to upper amphibolite facies (Kroonenberg et al., 2016). The derived metamorphic conditions described above, however, shows that the Sara's Lust Gneisses underwent metamorphism in mid amphibolite facies to the utmost.

The range in peak metamorphic conditions may imply that the Sara's Lust Gneisses exhibit a metamorphic gradient. Mapping these gradients in the Sara's Lust Gneisses, although considered challenging, will potentially imply whether this can indeed be said for the Sara's Lust Gneisses. If this will appear so, the Sara's Lust Gneisses could represent the medium-grade metamorphic formation containing the metamorphic transition between the lower-grade metamorphic Marowijne Greenstone Belt and the high-grade metamorphic Bakhuis Granulite Belt and Cauarane Coeroeni Gneiss Belt.

## **6.2. Trace element geochemistry**

The multiple-element diagrams of the Sara's Lust Gneisses clearly illustrate the loss of mobile elements (Figures 29, 30, 31), implying that the Sara's Lust Gneisses have been subjected to weathering or metasomatism, before, during or after metamorphism. As a consequence, the spider

diagrams of the Sara's Lust Gneisses do not necessarily correspond to the original trace element content of the protoliths. A distinction must, therefore, carefully be made between anomalies caused by metamorphic, metasomatic and weathering processes and anomalies already exhibited by the protolith.

### **6.2.1. General anomalies**

#### *6.2.1.1. Large ionic lithophile elements*

Distinct negative anomalies in Cs, Rb, K, Pb and Sr (except for KG1006, which does not possess a negative Sr anomaly) are present in all the samples from the Sara's Lust Gneisses. These LILEs are relatively mobile in fluids. Thence, these anomalies are attributed to fluid interaction, either by weathering or metasomatism. During fluid interaction, mobile elements such as Cs, Rb, K, Pb and Sr could have been flushed away leaving the rock to be depleted in these elements. Strangely, Ba does not seem to show a significant loss, despite its relatively high mobility in fluids. Possibly, the metasomatic fluid was Ba-rich. Nonetheless, interpretations based on Ba content were still considered uncertain and were preferably avoided.

#### *6.2.1.2. Nb, Ta, Ti*

All the samples from the Sara's Lust gneisses possess negative anomalies in Ti and Nb, with the felsic rocks showing the largest depletion in Ti and Nb. Notably, Ta anomalies are absent in all samples. Negative anomalies in high field strength elements are often explained by metamorphism. These elements are immobile during metamorphism due to their high cationic charge (Nicollet and Andriambololona, 1980). All the other more mobile elements are enriched in newly formed minerals resulting in a relative depletion in Ti and Nb. It is likely that this was, to a certain extent, also the case for the Sara's Lust Gneisses. This explanation, however, does not completely justify why the felsic rocks exhibit the highest negative anomaly in Nb and Ti. The felsic rocks underwent the least metamorphic change so that a smaller depletion in Ti and Nb is expected compared to the mafic and sedimentary rocks. It is, therefore, assumed that the negative anomalies in Nb and Ti in the felsic rocks were already present prior to metamorphism. Further possible explanations for the negative anomalies in Nb and Ti in the felsic rocks are discussed in Section 6.2.3. The depletion in Ti and Nb of the metasediments likely reflects the composition of the source rocks, with possibly some depletion during metamorphism. Hence, the source material of the metasediments of the Sara's Lust Gneisses likely comprise a significant amount of felsic material.

### **6.2.2. Trace element geochemistry of the meta-mafic to intermediate rocks and tectonic implications**

LB107B is highly enriched in U. U behaves as an incompatible element and partitions in the melt phase. Therefore, generally, U enrichment indicates the presence of felsic material. LB107B contains,

however, a relatively low silica content of 54.62 wt.%, indicating only minor incorporation of felsic material. U is also enriched in clays, especially kaolinite, for U can readily adsorb to clay minerals (Bachmaf et al., 2011). It is possible that the protolith of LB107B contained a higher input of sediments with a higher clay amount compared to LB107A, causing it to be more enriched in U. Another possibility would be enrichment due to metasomatic processes. The positive U anomaly in LB107B also caused LB107B to be less depleted in lead because U radioactively decays to Pb. LB107B also differs in LILE abundance as it is much more depleted in Cs, Rb and K. This may indicate that LB107B was subjected to a higher grade of alteration due to fluid interaction.

For inferring the tectonic setting(s), different tectonic discrimination diagrams (Figures 50 - 53) were used so that tectonic interpretations were not based on a few elements. The discrimination diagrams of Meschede (1986) and Pearce and Cann (1973) are based on basalts with composition  $MgO + CaO = 12 - 20$  wt.%. LB106A and LB106B do not reach this  $MgO + CaO$  content for they are more intermediate in composition. This makes the tectonic implications for LB106A and LB106B questionable in these diagrams. Wood's discrimination diagram is, on the other hand, beside basalts, also applicable to intermediate and silicic lavas.

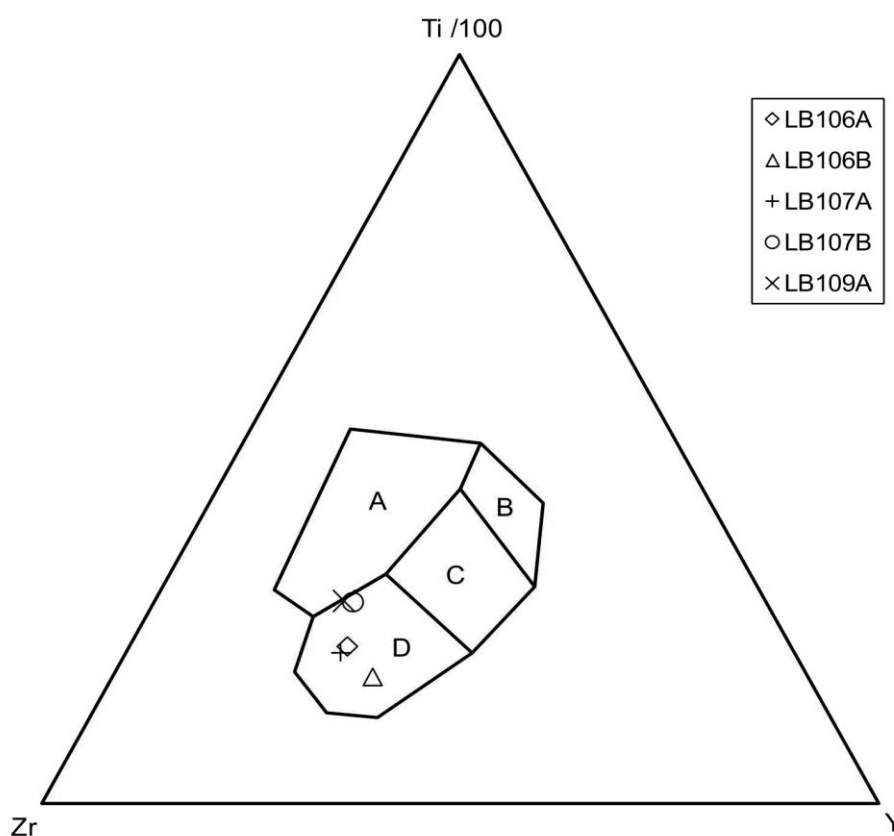


Figure 50 - Tectonic discrimination diagram for mafic rocks, based on Ti, Zr and Y content. Field A = within-plate basalts, field B = island arc basalts, field C = ocean floor, island arc and calc-alkali basalts, field D = calc-alkali basalts. The discrimination diagram is from Pearce & Cann (1973).

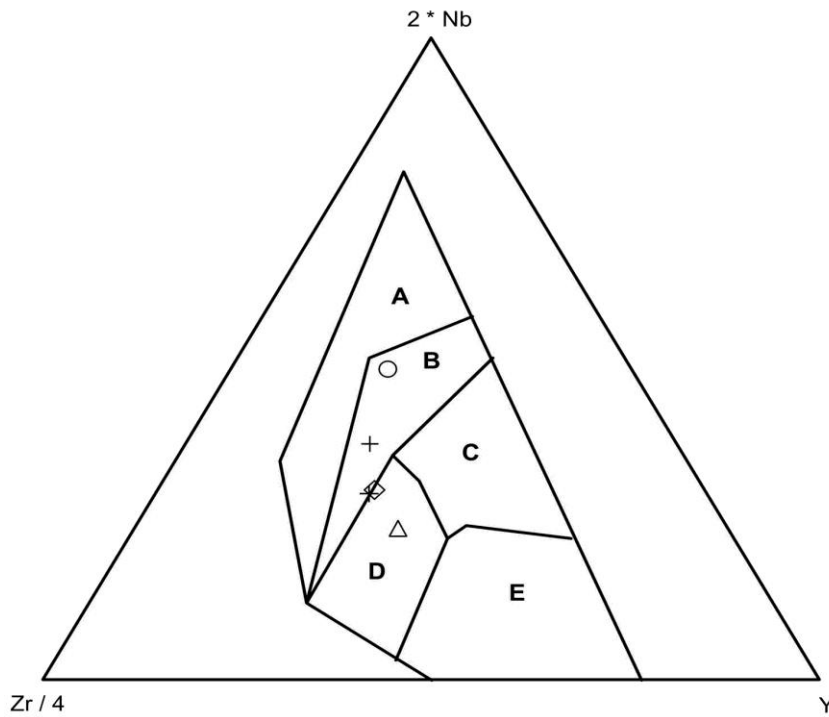


Figure 51 - Tectonic discrimination diagram for mafic rocks, based on Nb, Zr and Y content. Field A = within-plate alkali basalts, field B = within-plate alkali and tholeiite basalts, field C = E-MORB, field D = within-plate tholeiites, field E = N-MORB. The discrimination diagram is from Meschede (1986). The legend can be found in Figure 50.

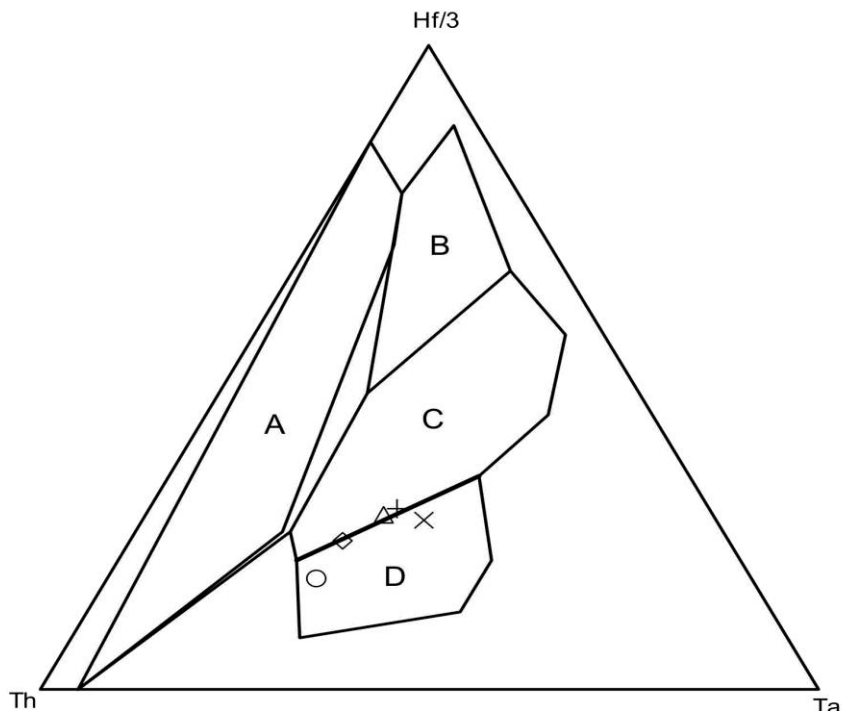


Figure 52 - Tectonic discrimination diagram for mafic rocks, based on Hf, Th and Ta content. Field A = calc-alkaline and primitive tholeiites, field B = N-MORB, field C = E-MORB and tholeiitic within-plate basalts, field D = Alkaline within-plate basalts. Discrimination diagram is from Wood (1980). The legend can be found in Figure 50.

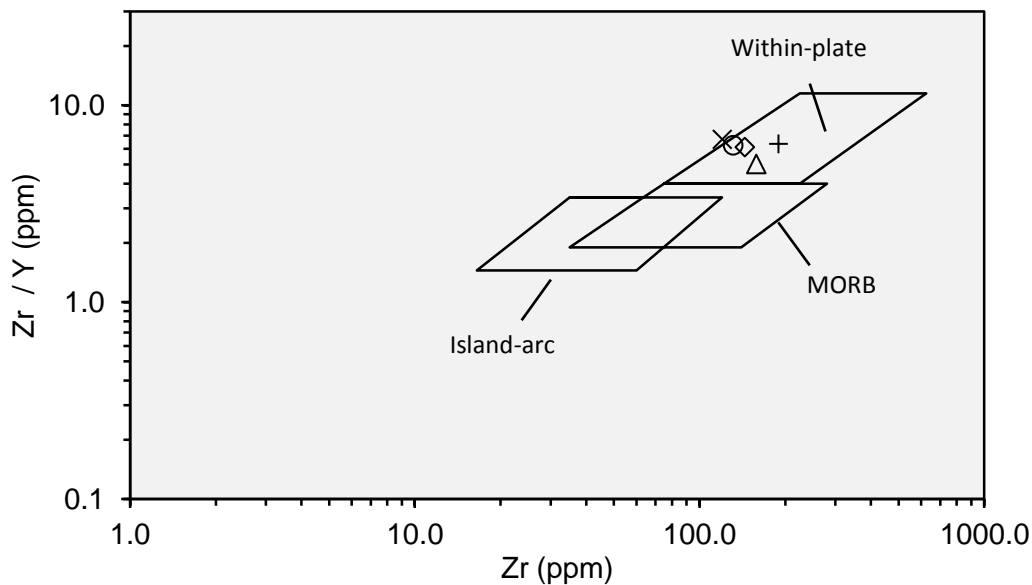


Figure 53 - Tectonic discrimination diagram for mafic rocks, based on Zr and Y content. The discrimination diagram is from Pearce & Norry (1979). The legend can be found in Figure 50.

Pearce et al. (1984) state that tectonic discrimination diagrams based on geochemistry must be used with care with 'old' rocks. During the earliest part of Earth history, the mantle was hotter which led to a higher amount of mantle melting. As a result, fractionation ratios between elements were different compared to the current-day situation. Nonetheless, the majority of the mafic rocks plot within the within-plate basalt field, either exhibiting a tholeiitic or a calc-alkaline composition. The only deviating tectonic implication comes from the diagram of Pearce & Cann (1973), in which all the mafics plot within the 'calc-alkali' field. Nevertheless, the tectonic discrimination diagrams are considered to yield consistent results, suggesting that interpretations on these diagrams are reliable. Thence, these diagrams illustrate that the mafic to intermediate suite of the Sara's Lust Gneisses represent within-plate derived mafics, suggesting a plume-like or oceanic plateau setting.

To elaborate on the proposed within-plate tectonic setting, trace element concentrations of the mafic rocks were normalised over N-MORB composition and plotted together with OIB composition (Figure 54). The geochemical composition for EM and HIMU are from the representative data from Sun and McDonough (1989) of St Helena and Gough Island, respectively and N-MORB composition was taken from Hofmann (1988).



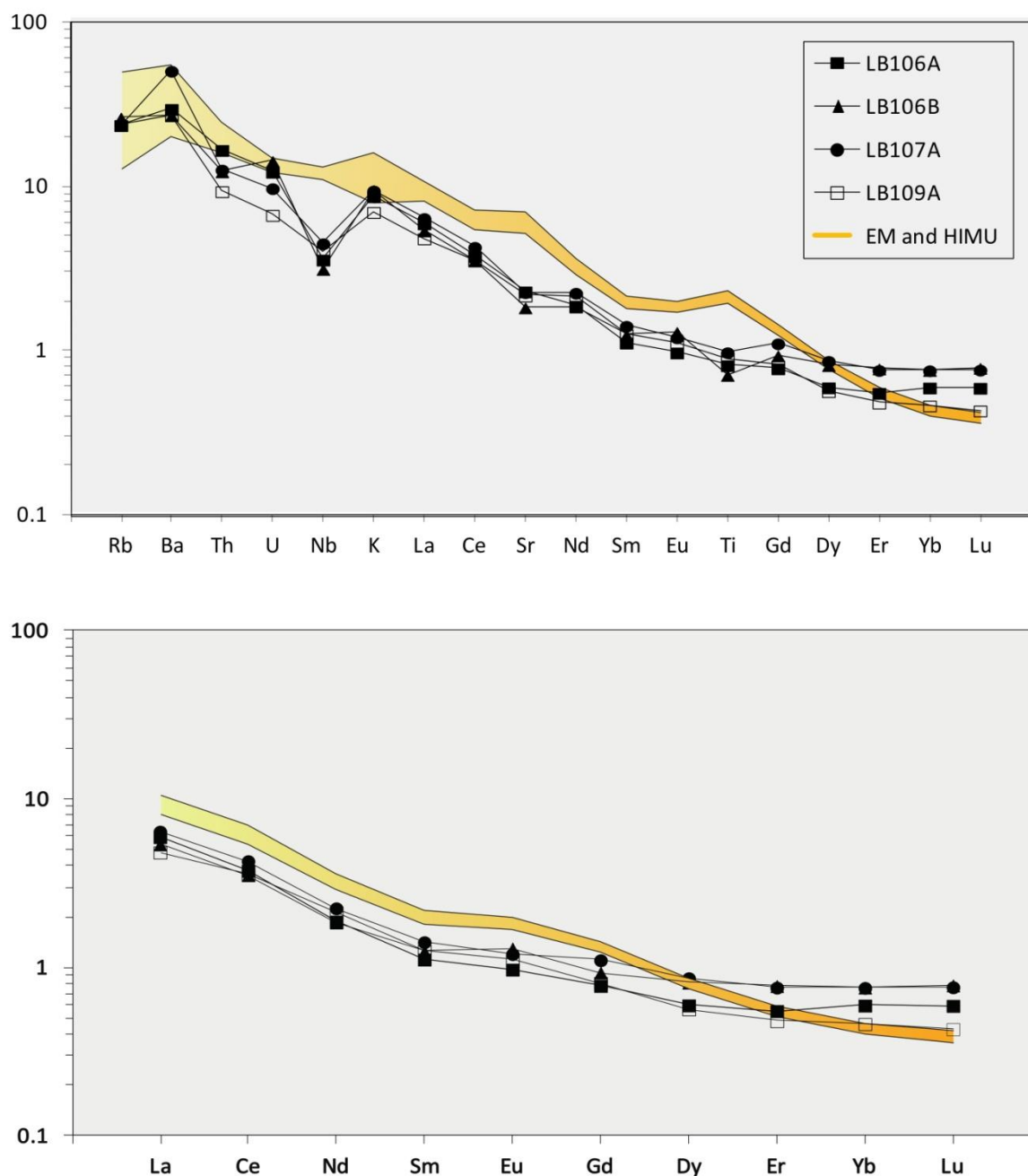


Figure 54 - Multiple-element diagram (top) and REE diagram (bottom) of the mafic suite of the Sara's Lust Gneisses plotted with HIMU and EM compositions in orange. Concentrations were normalised to N-MORB. Values for N-MORB were taken from Hofmann (1988), HIMU and EM composition were taken from Sun and McDonough (1989).

Compared to HIMU and EM composition, the Sara's Lust Gneisses exhibit anomalous abundances of the HREEs against a more depleted background of the other incompatible elements. The difference in age between the Sara's Lust Gneisses and the basalts of St Helena and Gough Island may clarify this difference. Melting products derived from Archean and Proterozoic plumes are less enriched compared to more recent mantle plume melting products. This compositional change is thought to be

caused by the onset of subduction (Campbell & Griffiths, 1992). Subducted material enters the mantle and enriches the mantle plume source. It takes time for subducted material to sink, heat up and ascend. As a consequence, enriched mantle plumes started to be generated after the onset of subduction, between 2.0 and 2.7 Ga (Campbell & Griffiths, 1992). Hence, despite the lower abundance in the LREEs to younger melts derived by a mantle plume, the mafic rocks of the Sara's Lust Gneisses are expected to represent plume-derived volcanics.

The mafic to intermediate rocks of the Sara's Lust Gneisses vary from tholeiitic to calc-alkaline composition (Figures 24, 51, 52). In an oceanic plateau or plume-like setting, both tholeiitic and calc-alkaline mafic rocks can supposedly originate from a single plume source. Bardintzeff et al. (1994) proposed that a gradual transition in tholeiitic to calc-alkaline composition can occur over time in the plume-derived melts.

### ***6.2.3. Trace element geochemistry of the felsic suite and tectonic implications***

The majority of the felsic rocks from the Sara's Lust Gneisses exhibits a small negative Eu anomaly, except for LB108B. A negative Eu anomaly is often attributed to early plagioclase fractionation. The absence of a negative Eu anomaly in LB108B may indicate that LB108B contains some cumulate plagioclase.

The REE pattern of KG1006 deviates most notably. As already mentioned, KG1006 is a trondhjemite. The source of trondhjemites is situated at such depths that garnet is a stable phase. Garnet retains the melt from HREEs resulting in the observed REE pattern of KG1006. Further, Sr is, compared to other samples, enriched in KG1006 (Figure 30). Carbonates, which can contain significant amounts of Sr, were not observed with the light microscope. It is, hence, considered that the high Sr content of KG1006 is a feature of the protolith. Despite the deviating Sr content compared to other TTGs (Figure 36) from Moyen's (2011) TTG database, Table 22 illustrates that, according to Moyen & Martin (2012), Sr content of KG1006 is still in agreement with the characteristic geochemical composition of trondhjemites.

For further elaboration on the tectonic setting of the felsic suites of the Sara's Lust Gneisses, two discrimination diagrams were used from Pearce et al. (1984) (Figures 55 and 56). The discrimination diagrams from Pearce et al. including Rb content as a factor are excluded as Rb was likely lost due to alteration.

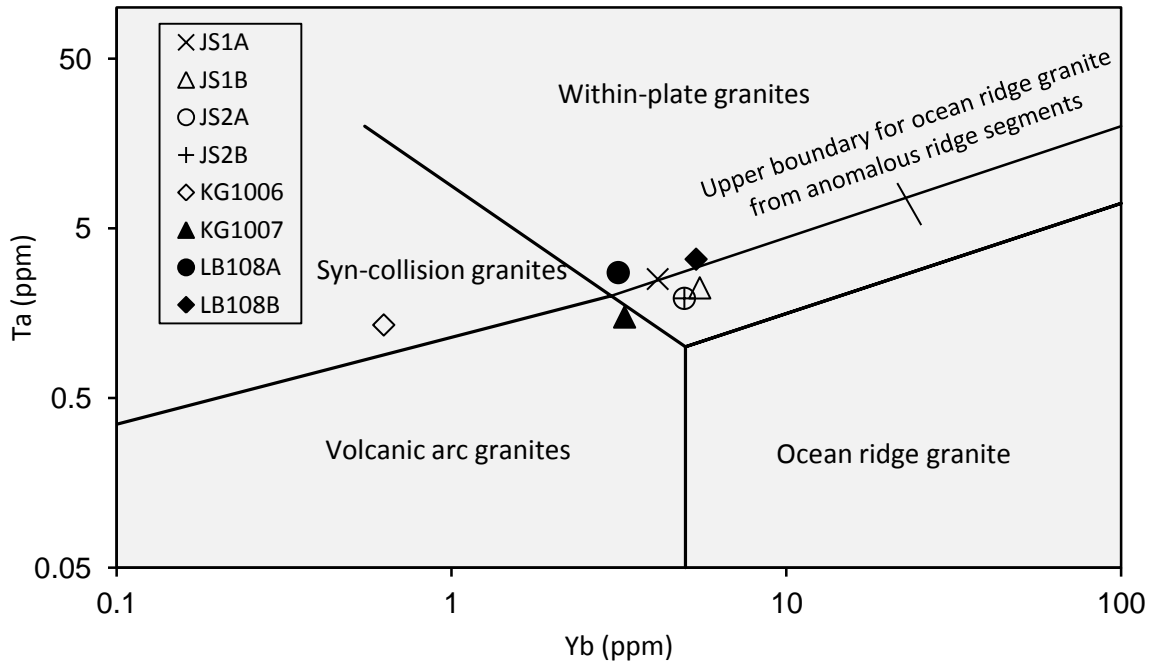


Figure 55 - Tectonic discrimination diagram for granitoids based on Ta and Yb content, from Pearce et al. (1984).

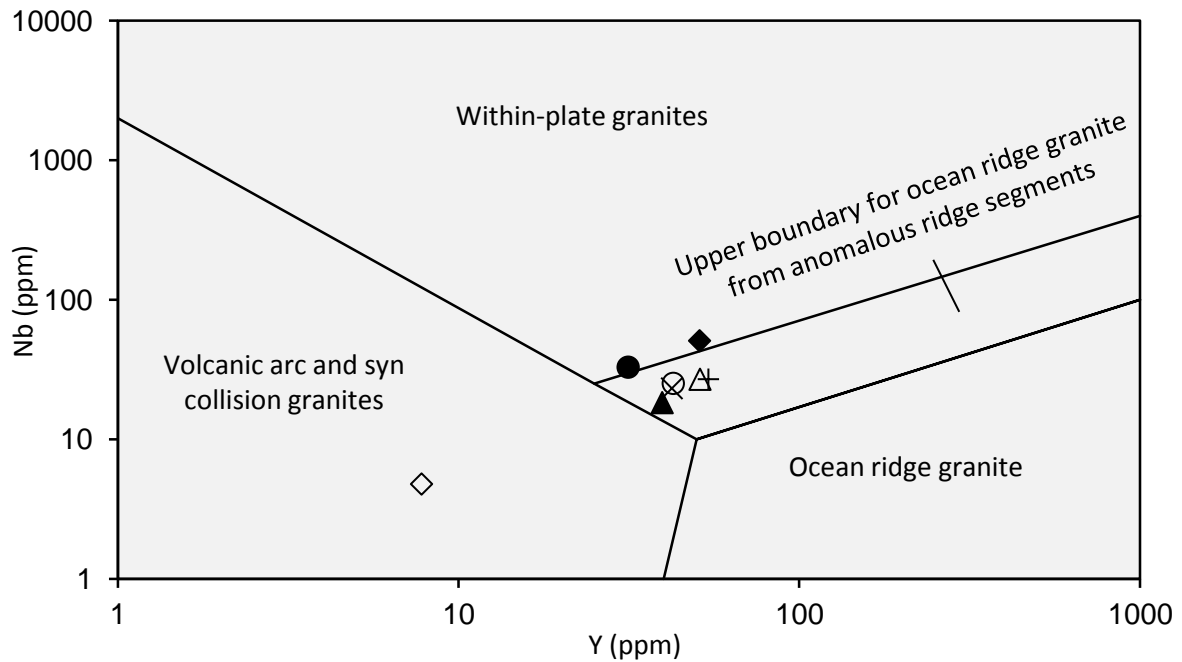


Figure 56 - Tectonic discrimination diagram for granitoids based on Nb and Yb content, from Pearce et al. (1984). The legend can be found in Figure 55.

In both Figures KG1006 plots within syn-collisional granites, whereby the Y-Nb plot also shows a petrogenesis associated with arc volcanism as a possibility. All other granitoids plot within 'upper boundary for ocean ridge granite from anomalous ridge segments', with KG1007, LB108A and

LB108B just outside this field. Ocean ridge granites can be found in mid-ocean ridges or in a back-arc setting. For further elaboration, see Section 6.3.1.2.

#### **6.2.4. Trace element geochemistry of the meta-sediments**

The trace element composition of the sediments chiefly reflects the composition of the source rocks. To elaborate on the source rocks of the metasediments, a multiple-element diagram was constructed normalised to PAAS (values after Hofmann, 2005). LE8 and LE9 exhibit conformable patterns, implying that these metagreywackes share the same source rocks and, thus, originate from the same basin. Furthermore, the multiple-element and REE diagrams for the metasediments closely resemble PAAS composition, but with some notable differences: LE8 and LE9 both are slightly more depleted in incompatible elements. A positive Eu anomaly is exhibited in both LE8 and LE9 compared to PAAS. The relative depletion in incompatible elements and a positive Eu anomaly both likely reflect that a substantial part of the source rock was mafic because 1) fractionation of plagioclase, and thus Eu fractionation, did not occur as much in the production of mafic rocks compared to felsic rocks, and 2) mafic rocks are less differentiated than felsic rocks with as a result a lower incompatible element content.

### **6.3. The Sara's Lust Gneisses within the context of the Transamazonian Orogeny**

As mentioned in the introduction, the higher grade metamorphic Sara's Lust Gneisses were thought to have one of the following geological relationship to the Marowijne Greenstone Belt: 1) they represent the lower crustal equivalent of the Marowijne Greenstone Belt. 2) They represent the basement onto which the volcanics and sediments of the Marowijne Greenstone Belt were deposited. Or, 3) the Marowijne Greenstone Belt thrusts onto the Sara's Lust Gneisses. To categorise the Sara's Lust Gneisses to either of these with respect to the Marowijne Greenstone Belt, geochemical and geochronological connections are sought between the two concerned formations.

#### **6.3.1. Relationships between the Sara's Lust Gneisses and the Marowijne Greenstone Belt**

##### **6.3.1.1. The mafic to intermediate suite**

The mafics of the Sara's Lust Gneisses are geochemically compared with the Paramaka Formation from the Marowijne Greenstone Belt (Figure 57), for they comprise similar lithologies. Geochemical data of the Paramaka andesites is from Daoust (2016), and of the Paramaka diorites, gabbros and amphibolites from Veenstra & De Vletter (1983).

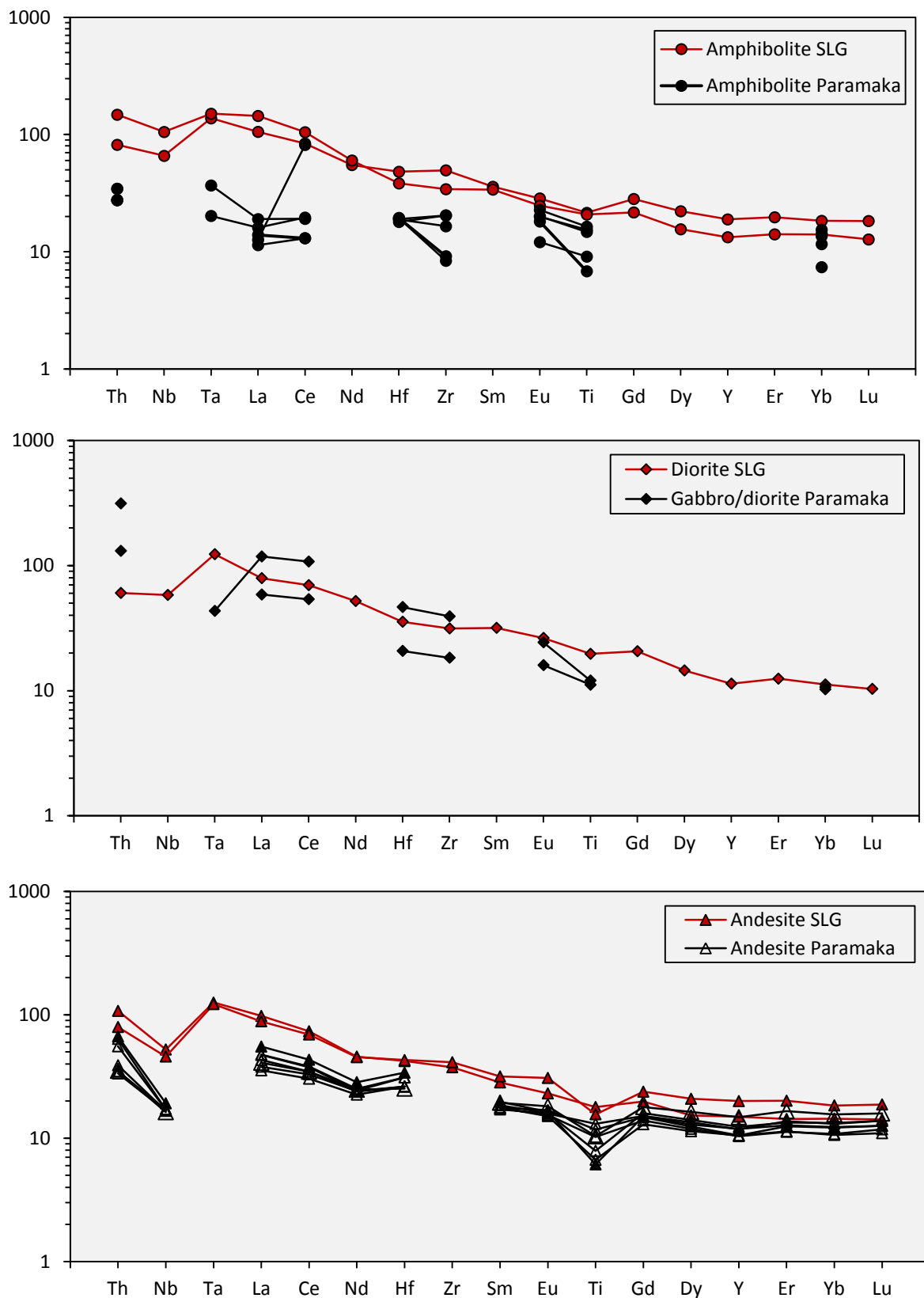


Figure 57 - Geochemical comparison of amphibolites (top diagram), diorites and gabbros (middle diagram), and andesites (bottom diagram) from the Sara's Lust Gneisses (SLG in the legend) and the Paramaka Formation. All concentrations are normalised to chondrite (Sun & McDonough, 1995). Elements that are likely altered due to fluid interactions or metamorphism are excluded.

The amphibolites, diorites and gabbros, and andesites of the Sara's Lust Gneisses are, compared to their lithological equivalent from the Paramaka Formation, generally more enriched. The spider-diagram trend, however, is fairly similar. For the comparison between different lithologies, trace element ratios are preferably used over single element concentrations because the partition coefficient of trace element is pressure and temperature dependent. This may cause an overall higher enrichment in trace elements but, in contrast, distribution ratios between trace elements will remain the same (White, 2013). Trace element ratios of the comparable lithologies between the Sara's Lust Gneisses and the Paramaka Formation are comparable (Table 34), except for the La / Yb<sub>n</sub> ratio of the amphibolites. Also, the multiple-element trend of the amphibolites differ the most. This could be a reflection of a difference in protoliths between the amphibolites from the Sara's Lust Gneisses and the Paramaka Formation. Possibly, the amphibolites from the Sara's Lust Gneisses comprised a higher sedimentary component potentially resulting in a higher LREE content, reflected by the higher La / Yb<sub>n</sub> content. Nonetheless, geochemical data of the amphibolites is scarce so that comparing the two based on geochemistry is challenging. Sm, Y and Nb content lack in the data from Veenstra & De Vletter (1983). Further, the andesites of the Sara's Lust Gneisses yield a slightly higher value for La / Yb<sub>n</sub>. The difference in this ratio is, however, marginal and can be explained in terms of compositional layering in a volcanic rock. Such layering is present already at thin section scale in LB106B. Sediment-rich layers will yield higher La / Yb<sub>n</sub> than layers composed of more volcanic material. Thus, based on trace element ratios, the mafics of the Sara's Lust Gneisses and the Paramaka Formation are geochemically similar, indicating that these likely represent the same unit.

*Table 34 - Comparison of trace element ratio values between different suites of the Sara's Lust Gneisses (SLG) and the Paramaka Formation (PF), Armina Formation (AF) and Rosebel Formation (RF).*

Trace element ratio	Andesite		Diorite / gabbro		Amphibolite		Greywacke		
	SLG	PF	SLG	PF	SLG	PF	SLG	AF	RF
La / Yb <sub>n</sub>	4.81-	2.63-	7.08	5.49-	5.75-	0.93-	8.99-	4.62-	7.67-
	6.79	4.49		11.53	10.28	1.54	11.73	13.53	11.27
La / Sm <sub>n</sub>	2.80-	2.06-	2.50	-	2.80-	-	3.59-	2.85-	3.31-
	3.46	2.80			2.94		3.82	3.10	3.87
Ti / Y <sub>n</sub>	0.78-	0.51-	1.73	-	1.14-	-	0.99-	0.68-	0.60-
	1.20	1.12			1.56		1.15	1.31	0.89
Nb / Th <sub>n</sub>	0.49-	0.27-	0.96	-	0.71-	-	0.18-	0.20-	0.10-
	0.58	0.50			0.81		0.19	0.36	0.17

The geochemistry of the mafic suite of the Sara's Lust Gneisses imply that these were generated in a plume-like setting. An oceanic plateau setting comprising a mantle plume was also postulated by Velásquez et al. (2011) for the formation of oceanic crust in the Guiana Shield. Moreover, this would

be in agreement with the oceanic plateau setting proposed for the Birimian terranes (Abouchami et al., 1990; Boher et al., 1992). The majority of the literature on the Transamazonian Orogeny, however, assumes that first oceanic crust was produced in a mid-ocean ridge or a back-arc setting (Vanderhaeghe et al., 1998; Delor et al., 2003a; Daoust et al., 2011; Kroonenberg et al., 2016). Back-arc basalts have similar chemical composition as MORB (Saunders & Tarney, 1984). Thus, to account for the high content in incompatible elements in the mafic suite in such a tectonic setting, extreme magmatic differentiation must have taken place, making an oceanic plateau-like setting more plausible.

### 6.3.1.2. *The felsic suite*

KG1007 contains zircon populations which furnished multiple U-Pb ages (unpublished data). These populations all yield different values for Th / U (Table 35). This ratio has been used to derive whether zircons are metamorphic or magmatic. Generally, a Th / U value of ~0.5 indicates a magmatic origin (e.g. Kirkland et al., 2015) and values of ~0.1 are characteristic for metamorphic zircons (Rubatto, 2002). The Table below gives the different populations with corresponding ages and Th / U values.

*Table 35 - Different zircon ages of KG1007 with corresponding Th / U values (unpublished data).*

U-Pb age	Th / U
2084 ± 18 Ma	0.15
2156 ± 12 Ma	0.41
2276 ± 31 Ma	0.56

Other granitic samples have not been dated due to time constraints. Therefore, the zircon ages of KG1007 are treated as representative for all granitoids in the Sara's Lust Gneisses as they all, except KG1006, yield a similar tectonic setting (Figure 47, 48). The oldest U-Pb age for a zircon furnished, being ~2276 (± 31 Ma), predates the Transamazonian Orogeny and is therefore likely inherited from older crust. The youngest zircon population yields a very low Th / U, implying a metamorphic origin. This metamorphic age and its implications will be discussed further in Section 6.3.2. The zircons of 2156 Ma (± 12 Ma) have a Th / U value resembling magmatic zircons. The magmatic crystallisation age falls within a period (2156 - 2137 ± 6 Ma) of extensive island arc-volcanism due to the subduction of oceanic crust (Vanderhaeghe et al., 1998; Delor et al., 2003a) and shows similar ages compared to the Tamouri Complex in French Guiana (Delor et al., 2003a). This complex is the continuation of the southwestern section of the Sara's Lust Gneisses inward French Guiana (Delor et al., 2003a). During subduction, large volumes of TTG plutons were generated, including the Brinck's Granite, Kabel Tonalite, Phedra Granite and Tibiti Granite, all situated in the Marowijne Greenstone Belt. The Brinck's Granite and Phedra Granite are likely formed as a result of continued differentiation of TTG magmas and are associated with arc-volcanism or syn-collisional volcanism, as is the Kabel Tonalite

(Kromopawiro et al., 2019). For this reason they cannot be correlated with the granitoids of the Sara's Lust Gneisses. In contrast, the Tibiti Granite is likely not associated with arc or syn-collisional volcanism as its geochemistry was explained in terms of a within-plate petrogenesis (Kromopawiro et al., 2019). Due to its anorogenic petrogenesis the Tibiti Granite is therefore potentially the granitoid formation in Suriname which is the most reminiscent to the granitoids of the Sara's Lust Gneisses. The magmatic age of the Tibiti Granite, being 2119 ( $\pm$  33) Ma (Kromopawiro et al., 2019), however, differs significantly with the magmatic zircon ages of the Sara's Lust granitoids. In addition, the deduced tectonic setting of the Tibiti Granite is, withal, different. As a consequence, the Tibiti Granite also unlikely shares a petrogenetic relationship with the Sara's Lust granitoids. Alternately, it is thought that the Sara's Lust granitoids do not have a distinct felsic plutonic equivalent in the Marowijne Greenstone Belt. This can, nonetheless, be explained in a subduction setting. The Brinck's Granite, Kabel Tonalite and Phedra Granite were generated in the volcanic-arc and in the subsequent collisional region. Contrastingly, the granitoids of the Sara's Lust Gneisses likely find their petrogenesis in an ocean ridge setting. This can be, with respect to the granitoids being generated contemporaneously with subduction, best interpreted as a back-arc setting.

In addition, the granitoids of the Sara's Lust Gneisses have an A-type affinity (Figure 58). A-type granites form from anhydrous high temperature parental magmas and can form in post-collisional, extensional or mantle-plume like settings (Loiselle, 1979; Whalen et al., 1987). In a back-arc setting, extension could enable A-type granite generation as extension leads to thinning of the crust with consequent anhydrous decompression melting of the mantle. This, in turn, causes the ascension of basaltic magmas into the lower crust causing a temperature rise. Eventually, the increased temperatures result in partial melting of the lower crust which compose the A-type granites (Whalen et al., 1987; Martin, 2006). A-type granites have been reported before in a back-arc (Jiang et al., 2006).

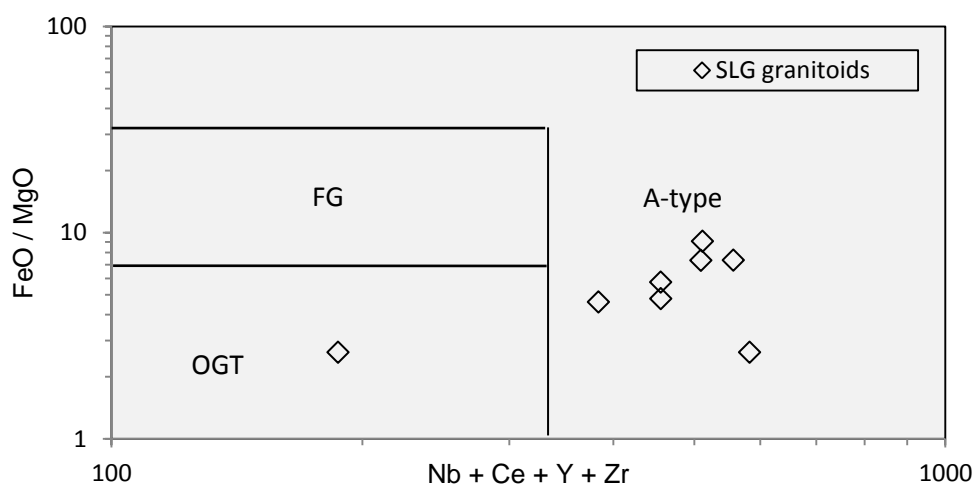


Figure 58 - Discrimination diagram for A-type granites, from Whalen et al. (1987). FG = fractionated granites, OGT = unfractionated granites comprising M-, I- and S-type granites. The OGT-granite is KG1006.



The A-type melt is mainly crust-derived (Martin, 2006). Consequently, for the generation of A-type granites in a back-arc scenario, the back-arc is required to be continental to provide the felsic material of the A-type granitoids. Partial melting of continental crust explains plagioclase fractionation with as a result the negative Eu anomaly in the granitoids. Moreover, the prominent Nb and Ti depletions in the felsic rocks of the Sara's Lust Gneisses are, in terms of crustal partial melting, explained in terms of fractionation. These HFSE elements have high partition coefficient between minerals and melt (Green & Pearson, 1986). As a consequence, the solid will retain the melt from Nb and Ti during partial melting. Possible retaining phases are pyroxene, ilmenite, amphibole or pyroxene. An anhydrous source implies that residual amphibole cannot account for the depletion in Ti and Nb. Instead, residual pyroxene can cause a Ti depletion in an A-type melt, as proposed by Chen et al. (2000), possibly retaining Nb from the melt as well.

The possible pyroxene remnants observed in the granitoids (see Table 5 in Section 5.1) could imply an anhydrous parental magma. Due to the anhydrous composition, amphiboles and biotite were unable to crystallise during the early magmatic history and consequently, pyroxene formed instead. Moreover, the late magmatic biotite crystallised around felsic materials observed in the majority of the felsic samples is also consistent with an initial dry magma. In this scenario, only after substantial crystallisation of anhydrous minerals did the melt become hydrous enough to crystallise biotite. The petrography of the Sara's Lust granitoids can, hence, also be justified by an A-type affinity.

The generation of A-type granites in an extensional regime necessitates invoking bimodal melting, whereby mantle material melts, giving rise to basaltic magmas. These basaltic magmas are not present among the 15 samples of this study, as the mafic suite comprises amphibolites, diorite and andesites (with a basaltic affinity). As the amount of samples of this study is little, more samples are required to investigate if these basalts are present in the Sara's Lust Gneisses.

#### *6.3.1.3. KG1006*

KG1006 is formed by syn-collisional or arc volcanism according to the tectonic discrimination diagrams (Figures 55 and 56). Other TTGs in the Guiana Shield are associated with subduction between 2.18 - 2.13 Ga (Delor et al., 2003a). Geochronological data will imply whether KG1006 can be correlated with the other TTGs in the Guiana Shield. As KG1006 is not an A-type granite, yields a different tectonic setting compared to the other granitoids of the Sara's Lust Gneisses, and is located at a different location, KG1006 is preferably excluded from the Sara's Lust Gneisses. The map illustrating the location of the samples of the Sara's Lust gneisses (Figure 2) shows that KG1006 is not located within the Sara's Lust Gneiss lithology.

#### 6.3.1.4. The sedimentary suite

The metagreywackes of the Sara's Lust Gneisses are lithologically comparable to two metasedimentary formations in the Marowijne Greenstone Belt: the Armina Formation and the Rosebel Formation. Distinguishing between these formations has proven difficult to date because field contacts are not well-exposed.

The Armina Formation and the Rosebel Formation exhibit a similar multi-element graph (Figure 59). The greywackes of the Sara's Lust Gneisses exhibit a somewhat steeper trend compared to the Armina Formation and is more reminiscent to the Rosebel Formation. The Rosebel Formation is more depleted in Ti compared to the Sara's Lust greywackes. Trace element ratios of the Sara's Lust, Armina and Rosebel greywackes are, nonetheless, all fairly similar (Table 34) so that a correlation based on geochemistry between the metagreywackes of the Sara's Lust Gneisses and from the Armina or Rosebel Formation could not be made.

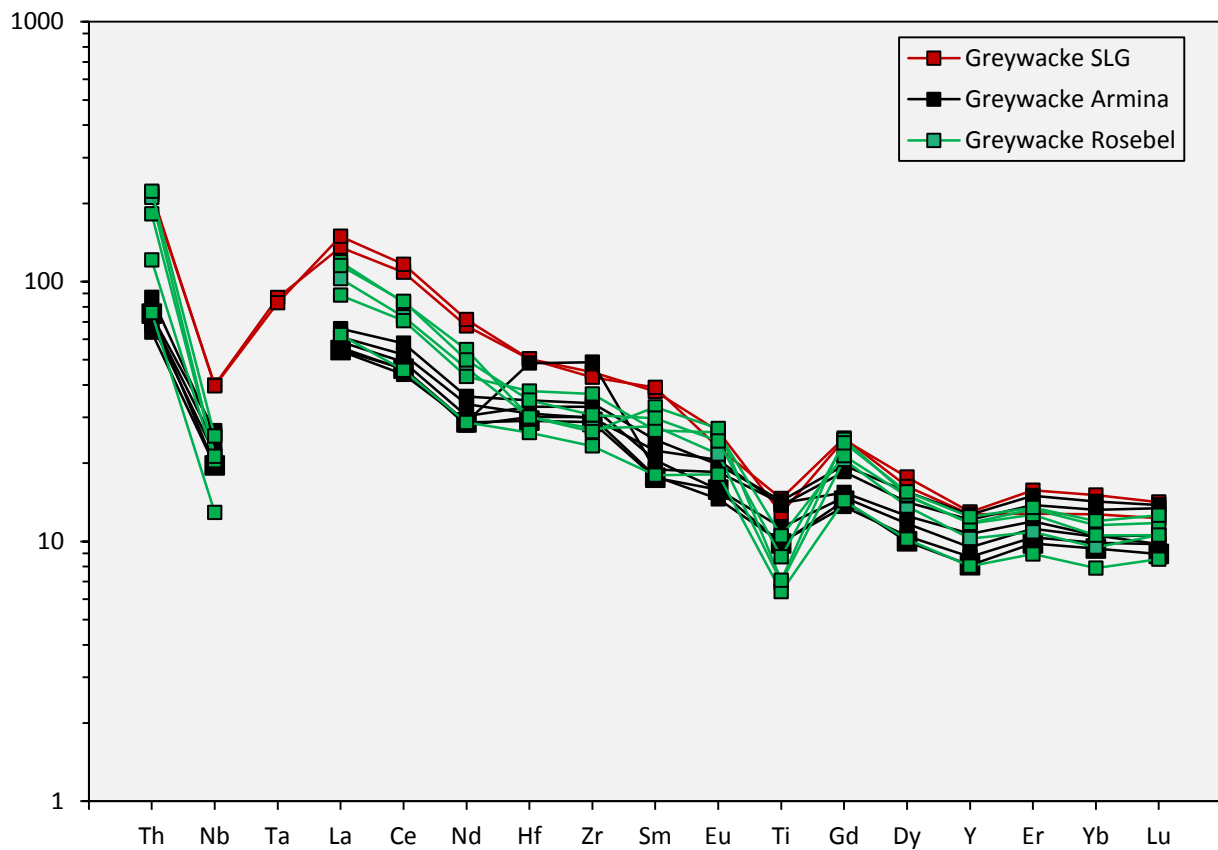


Figure 59 - Multiple-element diagram containing geochemical data of the Sara's Lust Gneisses, the Armina Formation and the Rosebel Formation. Geochemical data of the metasediments is from Daoust (2016), the classification between Rosebel and Armina metasediments is based on the work of Naipal & Kroonenberg (2016).

Naipal & Kroonenberg (2016) proposed that key differences between the Rosebel Formation and the Armina Formation are that the Rosebel Formation is more mature and lower in FeO, MgO and TiO<sub>2</sub> content and higher in SiO<sub>2</sub> content compared to Armina metasediments. This is the result of a different provenance, as the Armina Formation contains considerably more mafic volcanic lithic clasts whereas the Rosebel Formation mainly contain TTG clasts (Naipal & Kroonenberg, 2016).

Mixing calculations were applied here to derive the provenance of the metagreywackes. Fralick & Kronberg (1997) used Zr, Ti and Al<sub>2</sub>O<sub>3</sub> content for the source rock determination of metasandstones. These parameters were also used in the mixing calculation for the metagreywackes of the Sara's Lust Gneisses (Figure 60). Three compositional end-members were used: mafics, felsics and TTGs. The latter, however, seems to play a minor role in the mixing composition of the metagreywackes. A mixing ratio between only mafic and felsic composition was, therefore, calculated using the mixing calculations of Langmuir et al. (1978). The metasediments are slightly off the calculated mixing curve. Metamorphism likely affected original Ti content of the metagreywackes. As a consequence, the position of the metagreywackes in Figure 61 would be even more off the mixing curve. This can have two explanations: 1) a small TTG component was present in the source, 2) the metagreywackes were not solely derived from local Sara's Lust Gneiss protoliths. To investigate the latter theory, an average composition of the Paramaka mafics was taken as mafic end-member composition for a mixing curve (Figure 60). Geochemical data of the Paramaka Formation was attained from the geochemical data of Daoust (2016). Figure 61 illustrates that the greywackes of the Sara's Lust Gneisses can be composed of a mixture between Paramaka mafic rocks and felsic plutonic rocks. It, furthermore, shows that LE8 is a composite sediment of 1:1 felsics to mafic rocks whilst LE9 is composed of ~55% mafic rocks.

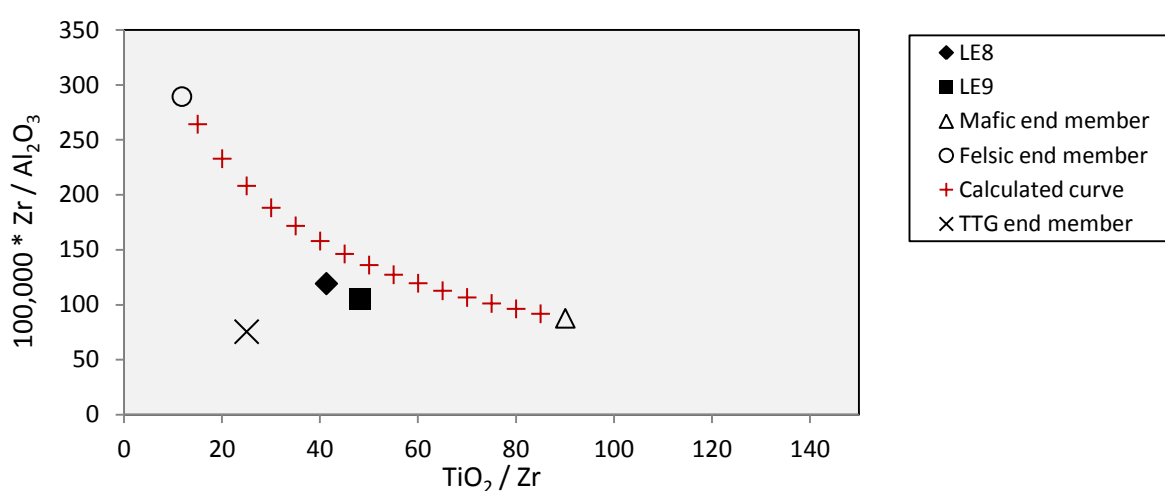


Figure 60 - Mafic, felsic and TTG end ember composition compared to LE8 and LE9. End-member composition are averages of different suites of the Sara's Lust Gneisses. The source of the metagreywackes only comprised little TTGs. Therefore, a mixing curve is plotted between the mafic and felsic end-member.

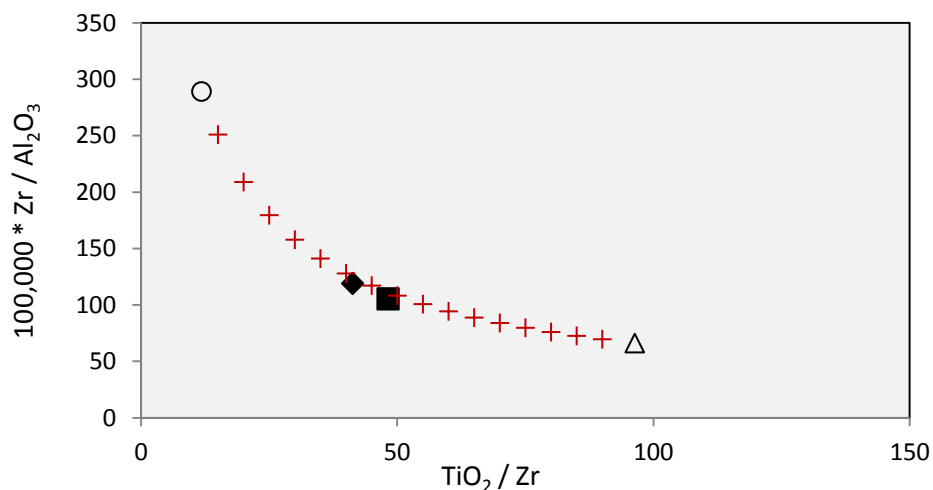


Figure 61 - Mixing curve calculation between the felsic end-member and a mafic end-member with Paramaka Formation composition. Geochemical data for the Paramaka mafic end-member is taken from Daoust (2016). The corresponding legend can be found in Figure 60.

Possibly, TTG material comprised a small portion of the source material of the Sara's Lust greywackes. Yet, Figure 60 shows that TTG material is not necessarily included in the provenance of the Sara's Lust greywackes. This may indicate that the Sara's Lust greywackes were deposited far enough from the out of mainly TTG material composed volcanic arc. As a result, the majority of eroded TTG material was deposited before reaching the provenance area of the Sara's Lust greywackes. A back-arc setting plausibly provides the necessary distance between the volcanic arc and the provenance area. In this scenario, the metagreywackes represent the sedimentary infill of the back-arc basin.

### 6.3.2. Metamorphism

Rosa-Costa et al. (2009) stated, based on  $^{40}\text{Ar} - ^{39}\text{Ar}$  data on amphiboles and biotites from Brazil, that the Guiana Shield was not metamorphically affected on regional scale after the Transamazonian Orogeny. This implies that the amphibolitic mineral assemblages observed in the Sara's Lust Gneisses can directly be linked to regional metamorphism attributed to the Transamazonian Orogeny. This is supported by the metamorphic U-Pb age from zircons from KG1007, being 2084 Ma ( $\pm 18$  Ma) (see Section 6.3.1.2.). This metamorphic age agrees with the D2 deformation phase (2.11 - 2.08 Ga) of Delor et al. (2003a) comprising the collisional stage of the Transamazonian Orogeny.

### 6.3.3. A tectonic relationship between the Sara's Lust Gneisses and the Marowijne Greenstone Belt

A chief part of the granitoids that intruded the Marowijne Greenstone Belt were generated coevally with the subduction event and are associated with arc volcanism (Kromopawiro et al, 2019). Hence,

during the subduction event of the Transamazonian Orogeny (2.18 - 2.13 Ga), the Marowijne Greenstone Belt was situated in or near the volcanic arc. Contrastingly, the granitoids in the Sara's Lust Gneisses are A-type and were most likely generated in the back-arc of the subduction zone. This gives a spatial difference in a subduction zone, implying that neither an upper-lower crustal relationship nor the Sara's Lust Gneisses representing the basement of the volcanics and sediments of the Marowijne Greenstone Belt is likely. Rather, a subduction zone was, prior to collision, interpreted to be present between the Marowijne Greenstone Belt and the Sara's Lust Gneisses. Because the Sara's Lust Gneisses and the Marowijne Greenstone Belt are currently adjacently situated on the surface, crustal shortening involving thrusting is proposed. Plausibly, during the collisional phase (2.11 - 2.08 Ga) of the Transamazonian Orogeny, the Marowijne Greenstone Belt thrust over the Sara's Lust Gneisses which led to metamorphism up to amphibolites facies in the Sara's Lust Gneisses. Thus, the Sara's Lust Gneisses likely shares a tectonic relationship with the Marowijne Greenstone Belt.

Large scale thrusting needs to have resulted in associated deformation. A majority of the samples exhibit small scale shear zones. These shear zones, however, are interpreted as post-metamorphic features (as explained in Section 5.1) and are therefore no indication for the proposed thrusting of the Marowijne Greenstone Belt onto the Sara's Lust Gneisses. Alternately, the presence of blastomylonites (sample LB109B) does indicate significant shearing prior to or during metamorphism. This is in agreement with the chronology of the postulated tectonic relationship between the Marowijne Greenstone Belt and the Sara's Lust Gneisses.

#### **6.4. Geodynamic model**

To explain the gathered data on the Sara's Lust Gneisses collectively, the following geodynamic model is proposed: mafic material in the Guiana Shield was likely produced in a plume-like setting, possibly resembling an oceanic plateau. The Paramaka Formation and the mafic to intermediate rocks of the Sara's Lust Gneisses were both produced during this event. After oceanic crust production, the West African Shield and the Guiana Shield started to converge. This was the onset of the Transamazonian Orogeny and led to subduction of oceanic crust below the Guiana Shield. This, in turn, resulted in TTG plutonism, materialising a subduction-associated volcanic arc. Possibly, KG1006 finds its petrogenesis in this event. Coevally, a back-arc basin formed, where A-type granites ( $2156 \pm 12$  Ma) were generated due to crustal thinning and mantle upwelling. The piece of crust composing the Sara's Lust Gneisses was situated in this back-arc basin. Thereafter, the Sara's Lust greywackes deposited in the back-arc basin. Convergence led to crustal shortening with, ultimately, collision of the West African Shield and the Guiana Shield. During this event, the Marowijne Greenstone Belt thrust over the Sara's Lust Gneisses. As a consequence, temperatures of 620-650 °C and pressures of

5.8 - 6.9 kbar were reached causing amphibolite facies metamorphism ( $2084 \pm 18$  Ma) of the Sara's Lust Gneisses with local migmatization.

A comparable model has been postulated for the El Callao Greenstone Belt, Venezuela (Hildebrand, 2005; Hildebrand et al., 2013). A large mylonitic shear zone was reported on the base of the Marowijne Greenstone Belt. In addition, volcanics in the greenstone belt were found to be older than the underlying quartzite. Both findings imply the tectonic emplacement of the greenstone belt atop other formations during the collisional stage of the Transamazonian Orogeny (Hildebrand et al., 2013).

### **6.5. Geometric implications for the Transamazonian subduction zone**

The proposed geodynamic model suggests that the back-arc, represented by the northern section of the Sara's Lust Gneisses, was situated to the north of the arc, which is represented by the Marowijne Greenstone Belt. This spatial distribution implies northward subduction during the Transamazonian Orogeny. The turbidites of the Armina Formation are, in this scenario, situated correctly, as these sediments are located on the north, thus on the continental margin, of the arc-associated TTGs in the Marowijne Greenstone Belt (Figure 2). Oppositely, Delor et al., (2003a) reported a southward younging direction in TTG plutons in South Guyana indicating subduction towards the south.

The proposed geometry of the subduction zone during the Transamazonian Orogeny is solely based on a limited collection of 16 samples of one formation, making an extrapolated interpretation on continental scale arguably precarious. Further investigation covering the entire Guiana Shield is, therefore, required to investigate what the polarity was of the subduction zone.

### **6.6. Comparison with the Birimian Terranes**

Because geological data on the Guiana Shield is limited, especially in Suriname, a comparison is drawn between the West African Shield and the Guiana Shield. The West African Shield and the Guiana Shield once constituted a supercontinent after collision during the Transamazonian Orogeny. Hence, the West African Shield and its petrogenesis is thought to be representative for the Guiana Shield. The Dabakalian gneisses are peripheral to the Birimian Greenstone Belt and comprise high-grade metamorphosed mafic volcanics, granitoids and sediments. They are believed to be reminiscent to the Sara's Lust Gneisses. The Dabakalian Gneisses have been interpreted as Archean basement (Tagini, 1971). Lemoine (1988), however, provided Dabakalian and Birimian ages and both were Proterozoic. As a consequence, the Dabakalian Gneisses were interpreted as the lower crustal equivalent of the Birimian Greenstone Belt (Abouchami et al., 1990). However, as the proposed petrogenesis of the Sara's Lust Gneisses demonstrates, gneisses and greenstone belts with a similar age could also possibly have a tectonic relationship. A comparable geodynamic model might also hold

for the geological relationship between the Dabakalian and Birimian rocks. This is, however, speculative and further testing of this geodynamic model is a necessity for affirmation.

## **7. Conclusion**

Due to the lack of field relationships of the Sara's Lust Gneisses, the tectonic setting of this unit and its geological relationship with the Marowijne Greenstone Belt are exclusively interpreted from the presented geochemical and petrological data. The samples from the Sara's Lust Gneisses are subdivided into three suites: felsic, mafic to intermediate, and sedimentary. The mafic suite is, normalised to N-MORB, enriched in incompatible elements, implying generation in a plume-like setting. Geochemically, the mafic suite is comparable to the Paramaka Formation, suggesting that they represent the same unit. The granitoids are all A-type, and have probably been generated in an extensional setting. The magmatic age of these granitoids is 2156 ( $\pm$  12) Ma and is contemporaneous with the subduction event during the Transamazonian Orogeny. Hence, the granitoids of the Sara's Lust Gneisses are likely to result from (decompressional) partial melting in a back-arc setting, which is in contrast with other coevally generated granites and TTGs in the Marowijne Greenstone Belt, for these are associated with either arc or syn-collisional volcanism. This could point to the presence of a subduction zone in between the granitoids of the Sara's Lust Gneisses and granitoids in the Marowijne Greenstone Belt during the Transamazonian Orogeny. This spatial difference during subduction between the two concerned formations implies that the Sara's Lust Gneisses neither represent the lower crustal equivalent, nor the basement of the Marowijne Greenstone Belt. Because the Sara's Lust Gneisses are now adjacently situated to the Marowijne Greenstone Belt, a tectonic relationship is proposed instead, wherein the Marowijne Greenstone Belt thrusts onto the Sara's Lust Gneisses during collision. Prior to this thrusting event, the greywackes of the Sara's Lust Gneisses were deposited. The source rocks of these sediments are ~1:1 felsic to mafic and comprise little TTG material. This may indicate that the provenance area of the Sara's Lust metasediments was located at a considerable distance from the volcanic arc, as the volcanic arc is mainly composed of TTG rocks. Sediment deposition in a back-arc basin may provide for this required distance. Due to ongoing convergence with eventually collision between the Guiana Shield and the West African Shield, the Marowijne Greenstone Belt may have been thrust on top of the Sara's Lust Gneisses, resulting in metamorphism up to amphibolite facies with peak metamorphic conditions of 4.6 - 5.5 ( $\pm$  1) kbar and 617 - 688 ( $\pm$  50) °C. Metamorphic zircons in the Sara's Lust Gneisses furnished an age of 2084 ( $\pm$  18) Ma, which is correlated with the peak metamorphic episode during the collision phase of the Transamazonian Orogeny (2.11 – 2.08 Ga), postulated by earlier workers (Vanderhaeghe et al., 1998; Delor et al., 2003a). Thus, the petrogenetic history of the Sara's Lust Gneisses, and on a larger scale the Guiana Shield, is consistent with a change in tectonic style from a mantle-plume upwelling style from the earliest part of Earth history, towards modern-day horizontal tectonics.

## 8. Acknowledgements

I thank my first supervisor Paul Mason for his support and guidance in the geochemical part of this project and for all the new and useful ideas for the discussion. Further, I thank Leo Kriegsman, my second supervisor, for his guidance in the petrography research and in the supervision during Perple\_X modelling. I am also grateful to Salomon Kroonenberg, as he acted as a third supervisor in this project and helped me a lot with familiarising with the geology of Suriname. Lastly, I thank Helen de Waard for her guidance during LA-ICP-MS analysis, Jan van Tongeren for the sample preparation for the XRF analysis and for carrying out this analysis, and Tilly Bouten for her supervision during the microprobe sessions.

## 9. References

- Abouchami, W., Boher, M., Michard, A., and Albarede, F. (1990). A major 2.1 Ga event of mafic magmatism in West Africa: an early stage of crustal accretion. *Journal of Geophysical Research: Solid Earth*, 95(B11):17605-17629.
- Althaus, E., Karotke, E., Nitsch, K., and Winkler, H. (1970). An experimental re-examination of the upper stability limit of muscovite plus quartz. *Neues Jahrb. Mineral. Monatsh*, 7:325-336.
- Anhaeusser, C. R. (2014). Archean greenstone belts and associated granitic rocks-a review. *Journal of African Earth Sciences*, 100:684-732.
- Anhaeusser, C. R., Mason, R., Viljoen, M. J., and Viljoen, R. P. (1969). A reappraisal of some aspects of Precambrian shield geology. *Geological Society of America Bulletin*, 80(11):2175-2200.
- Arndt, N. T. (2013). The formation and evolution of the continental crust. *Geochemical Perspectives*, 2(3):405-405.
- Bachmaf, S. and Merkel, B. J. (2011). Sorption of uranium (VI) at the clay mineral-water interface. *Environmental Earth Sciences*, 63(5):925-934.
- Bardintzeff, J.-M., Leyrit, H., Guillou, H., Guille, G., Bonin, B., Giret, A., and Brousse, R. (1994). Transition between tholeiitic and alkali basalts: Petrographical and geochemical evidence from Fangataufa, Pacific Ocean, and Kerguelen, Indian Ocean. *Geochemical Journal*, 28(6):489-515.
- Barink, H. (1975). Geology of the Gonini River area, SE Suriname. *Mededelingen Geologisch Mijnbouwkundige Dienst Suriname*, 23:155-164.
- Barnes, S.-J., Gorton, M., and Naldrett, A. (1983). A comparative study of olivine and clinopyroxene spinifex flows from Alexo, Abitibi greenstone belt, Ontario, Canada. *Contributions to Mineralogy and Petrology*, 83(3-4):293-308.
- le Bas, M. L., Maitre, R. L., Streckeisen, A., Zanettin, B. (1986). A chemical classification of volcanic rocks based on the total alkali-silica diagram. *Journal of petrology*, 27(3):745-750.
- Berman, R. (1990). Mixing properties of Ca-Mg-Fe-Mn garnets. *American Mineralogist*, 75:328-344.
- Best, M. G. and Weiss, L. E. (1964). Mineralogical relations in some pelitic hornfelses from the southern Sierra Nevada, California. *American Mineralogist: Journal of Earth and Planetary Materials*, 49(9-10):1240-1266.



- Bickle, M., Martin, A., and Nisbet, E. (1975). Basaltic and peridotitic komatiites and stromatolites above a basal unconformity in the Belingwe greenstone belt, Rhodesia. *Earth and Planetary Science Letters*, 27:155-162.
- Bleys, C. (1951). Kaartblad D7. *Jaarverslag van de Geologisch Mijnbouwkundige Dienst over het jaar, 1950*:34-49.
- Boher, M., Abouchami, W., Michard, A., Albarede, F., and Arndt, N. T. (1992). Crustal growth in west Africa at 2.1 Ga. *Journal of Geophysical Research: Solid Earth*, 97(B1):345-369.
- Bohlen, S. R., Montana, A., and Kerrick, D. M. (1991). Precise determinations of the equilibria kyanite $\leftrightarrow$  sillimanite and kyanite $\leftrightarrow$  andalusite and a revised triple point for Al<sub>2</sub>SiO<sub>5</sub> polymorphs. *American Mineralogist*, 76(3-4):677-680.
- Bosma, W. (1971). *Geological Reconnaissance in the Dalbana Creek Area: Corantijn, Western Suriname*. Gouvernement van Suriname, Ministerie van Opbouw, Geologisch Mijnbouwkundige dienst van Suriname.
- Bosma, W., Kroonenberg, S., Maas, K., and De Roever, E. (1983). Igneous and metamorphic complexes of the Guiana Shield in Surinam. *Netherlands journal of geosciences*, 62:241-245.
- Bosma, W., Kroonenberg, S., van Cissa, R., Maas, K., and De Roever, E. (1984). An explanation to the geological map of Suriname.
- Bouhallier, H., Chardon, D., and Choukroune, P. (1995). Strain patterns in Archean dome-and-basin structures: the Dharwar craton (Karnataka, South India). *Earth and Planetary Science Letters*, 135(1-4):57-75.
- Bowen, N. L. (1956). *The evolution of the igneous rocks*. Dover Publications.
- Calvert, A., Sawyer, E., Davis, W., and Ludden, J. (1995). Archean subduction inferred from seismic images of a mantle suture in the Superior Province. *Nature*, 375(6533):670-674.
- Campbell, I. and Griffiths, R. (1992). The changing nature of mantle hotspots through time: implications for the chemical evolution of the mantle. *The Journal of Geology*, 100(5):497-523.
- Chen, C.-H., Lin, W., Lu, H.-Y., Lee, C.-Y., Tien, J.-L., and Lai, Y.-H. (2000). Cretaceous fractionated I-type granitoids and metaluminous A-type granites in SE China: the Late Yanshanian post-orogenic magmatism. *Earth and Environmental Science Transactions of the Royal Society of Edinburgh*, 91(1-2):195-205.
- Condie, K. C. (1981). *Archean greenstone belts*, volume 3. Elsevier.
- da Rosa-Costa, L. T., Monié, P., Lafon, J., M., and Arnaud, N., O. (2009). <sup>40</sup>Ar-<sup>39</sup>Ar geochronology across Archean and Paleoproterozoic terranes from southeastern Guiana Shield (north of Amazonian Craton, Brazil): Evidence for contrasting cooling histories. *Journal of South American Earth Sciences*, 27(2-3):113-128.
- Daoust, C. (2016). *Caractérisation stratigraphique, structurale et géochimique du district min'eralis'é de Rosebel (Suriname) dans le cadre de l'évolution géodynamique du Bouclier Guyanais*. PhD thesis, Université du Québec à Montréal.
- Daoust, C., Voicu, G., Brisson, H., and Gauthier, M. (2011). Geological setting of the Paleoproterozoic Rosebel gold district, Guiana Shield, Suriname. *Journal of South American Earth Sciences*, 32(3):222-245.
- de Roever, E. d., Lafon, J., Delor, C., Rossi, P., Cocherie, A., Guerrot, C., and Potrel, A. (2003). The Bakhuis ultrahigh-temperature granulite belt: I. petrological and geochronological evidence for a counterclockwise PT path at 2.07-2.05 Ga. *Géologie de la France*, 1:175-205.

- de Wit, M. and Tinker, J. (2004). Crustal structures across the central Kaapvaal craton from deep-seismic reflection data. *South African Journal of Geology*, 107(1-2):185-206.
- de Wit, M. J., Armstrong, R., Hart, R. J., and Wilson, A. H. (1987). Felsic igneous rocks within the 3.3-to 3.5-Ga Barberton Greenstone belt: High crustal level equivalents of the surrounding Tonalite-Trondhjemite Terrain, emplaced during thrusting. *Tectonics*, 6(5):529-549.
- Delor, C., de Roeber, E. W. F., Lafon, J., M., Lahondère, D., Rossi, P., Cocherie, A., Guerrot, C., and Potrel, A. (2003a). The Bakhuis ultrahigh-temperature granulite belt (Suriname): II. implications for late Transamazonian crustal stretching in a revised Guiana Shield framework.
- Delor, C., Lahondère, D., Egal, E., Lafon, J.-M., Cocherie, A., Guerrot, C., Rossi, P., Truffert, C., Théveniaut, H., Phillips, D., and de Avelar, V. G. (2003b). Transamazonian crustal growth and reworking as revealed by the 1: 500,000-scale geological map of French Guiana.
- Diener, J., Powell, R., White, R., and Holland, T. (2007). A new thermodynamic model for clino- and orthoamphiboles in the system Na<sub>2</sub>O-CaO-FeO-MgO-Al<sub>2</sub>O<sub>3</sub>-SiO<sub>2</sub>-H<sub>2</sub>O-O. *Journal of Metamorphic Geology*, 25(6):631-656.
- Ferry, J. t. and Spear, F. (1978). Experimental calibration of the partitioning of Fe and Mg between biotite and garnet. *Contributions to mineralogy and petrology*, 66(2):113-117.
- Fralick, P. and Kronberg, B. (1997). Geochemical discrimination of clastic sedimentary rock sources. *Sedimentary Geology*, 113(1-2):111-124.
- Furnes, H., Dilek, Y., and De Wit, M. (2015). Precambrian greenstone sequences represent different ophiolite types. *Gondwana research*, 27(2):649-685.
- Fyfe, W. (1978). The evolution of the Earth's crust: modern plate tectonics to ancient hot spot tectonics? *Chemical Geology*, 23(1-4):89-114.
- Gorman, B., Pearce, T., and Birkett, T. (1978). On the structure of Archean greenstone belts. *Precambrian Research*, 6(1):23-41.
- Grambling, J. A. (1981). Kyanite, andalusite, sillimanite, and related mineral assemblages in the Truchas Peaks region, New Mexico. *American Mineralogist*, 66(7-8):702-722.
- Green, T. and Pearson, N. (1986). Ti-rich accessory phase saturation in hydrous mafic-felsic compositions at high P, T. *Chemical Geology*, 54(3-4):185-201.
- Hickman, A. (1984). Archean diapirism in the Pilbara block, Western Australia. *Precambrian Tectonics Illustrated*, pages 113-127.
- Hildebrand, R. S. (2005). Autochthonous and allochthonous strata of the El Callao greenstone belt: Implications for the nature of the Paleoproterozoic Trans-Amazonian orogeny and the origin of gold-bearing shear zones in the El Callao mining district, Guayana shield, Venezuela. *Precambrian Research*, 143(1-4):75-86.
- Hildebrand, R. S., Buchwaldt, R., and Bowring, S. A. (2014). On the allochthonous nature of auriferous greenstones, Guayana shield, Venezuela. *Gondwana Research*, 26(3-4):1129-1140.
- Hirde, W., Davis, D., Lüdtke, G., and Konan, G. (1996). Two generations of Birimian (Paleoproterozoic) volcanic belts in northeastern Côte d'Ivoire (West Africa): consequences for the 'Birimian controversy'. *Precambrian Research*, 80(3-4):173-191.
- Ho Len Fat, A. (1975). Geology of the Pikien Rio-Beneden Tapanahony area (E. Suriname). *Mededelingen Geologisch Mijnbouwkundige Dienst Suriname*, 23:165-175.
- Hofmann, A. (2005). The geochemistry of sedimentary rocks from the Fig Tree Group, Barberton greenstone belt: implications for tectonic, hydrothermal and surface processes during mid-Archean times. *Precambrian Research*, 143(1-4):23-49.

- Hofmann, A. W. (1988). Chemical differentiation of the Earth: the relationship between mantle, continental crust, and oceanic crust. *Earth and Planetary Science Letters*, 90(3):297-314.
- Holland, T., Baker, J., and Powell, R. (1998). Mixing properties and activity-composition relationships of chlorites in the system MgO-FeO-Al<sub>2</sub>O<sub>3</sub>-SiO<sub>2</sub>-H<sub>2</sub>O. *European Journal of Mineralogy*, pages 395-406.
- Holland, T. and Powell, R. (1996). Thermodynamics of order-disorder in minerals: II. Symmetric formalism applied to solid solutions. *American Mineralogist*, 81(11-12):1425-1437.
- Hu, S. (1994). Evolution and development of tectonics and magmatism at the active continental margin of the East China during Mesozoic and Cenozoic. *Acta Petrol. Sinica*, 10:370-381.
- Hurley, P. M., Rand, J., Pinson, W., Fairbairn, H., de Almeida, F., Melcher, G., Cordani, U., Kawashita, K., and Vandoros, P. (1967). Test of continental drift by comparison of radiometric ages: A pre-drift reconstruction shows matching geologic age provinces in West Africa and Northern Brazil. *Science*, 157(3788):495-500.
- Jackson, M., Kröner, A., and Greiling, R. (1984). Archaean structural styles in the Ancient Gneiss Complex of Swaziland, southern Africa. *Precambrian Tectonics Illustrated*, pages 1-18.
- Jiang, Y.-H., Jiang, S.-Y., Zhao, K.-D., and Ling, H.-F. (2006). Petrogenesis of Late Jurassic Qianlishan granites and mafic dykes, Southeast China: implications for a back-arc extension setting. *Geological Magazine*, 143(4):457-474.
- Jiao, W., Wu, Y., Yang, S., Peng, M., and Wang, J. (2009). The oldest basement rock in the Yangtze Craton revealed by zircon U-Pb age and Hf isotope composition. *Science in China Series D: Earth Sciences*, 52(9):1393-1399.
- Kirkland, C., Smithies, R., Taylor, R., Evans, N., and McDonald, B. (2015). Zircon Th / U ratios in magmatic environments. *Lithos*, 212:397-414.
- Klaver, M., de Roever, E. W., Nanne, J. A., Mason, P. R., and Davies, G. R. (2015). Charnockites and UHT metamorphism in the Bakhuis Granulite Belt, western Suriname: Evidence for two separate UHT events. *Precambrian Research*, 262:1-19.
- Kleemann, U. and Reinhardt, J. (1994). Garnet-biotite thermometry revisited: The effect of AlVI and Ti in biotite. *European Journal of Mineralogy*, pages 925-942.
- Kromopawiro, S. C., Kroonenberg, S., Kriegsman, L., and Mason, P. R. (2019). 2.12-2.08 Ga Late- to post-collisional peraluminous granitoid magmatism in the Marowijne Greenstone Belt of Suriname.
- Kroonenberg, S. (1975). Geology of the Sisa creek area, SW Suriname. *Mededelingen Geologisch Dienst Suriname*, 23:102-125.
- Kroonenberg, S., De Roever, E., Fraga, L., Reis, N., Faraco, T., Lafon, J.-M., Cordani, U., and Wong, T. E. (2016). Paleoproterozoic evolution of the Guiana Shield in Suriname: A revised model. *Netherlands Journal of Geosciences*, 95(4):491-522.
- Labrosse, S. and Jaupart, C. (2007). Thermal evolution of the Earth: Secular changes and fluctuations of plate characteristics. *Earth and Planetary Science Letters*, 260(3-4):465-481.
- Langmuir, C. H., Vocke Jr, R. D., Hanson, G. N., and Hart, S. R. (1978). A general mixing equation with applications to Icelandic basalts. *Earth and Planetary Science Letters*, 37(3):380-392.
- Lemoine, S. (1988). *Evolution géologique de la région de Dabakala (NE de la Côte d'Ivoire) au Protérozoïque inférieur: possibilités d'extension au reste de la Côte d'Ivoire et au Burkina Faso*. PhD thesis, ANRT.

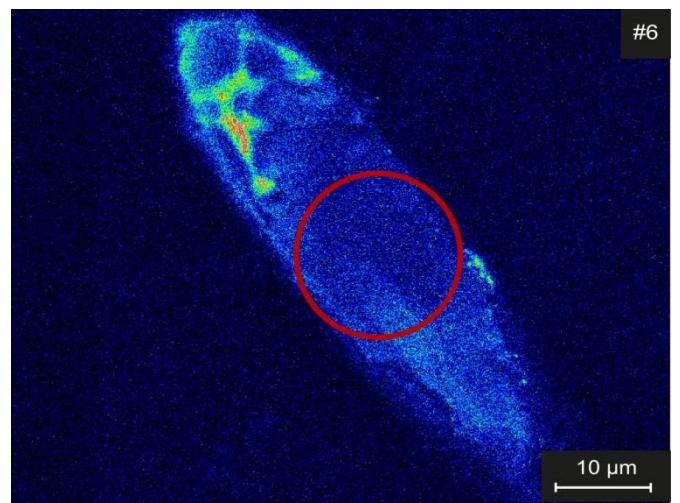
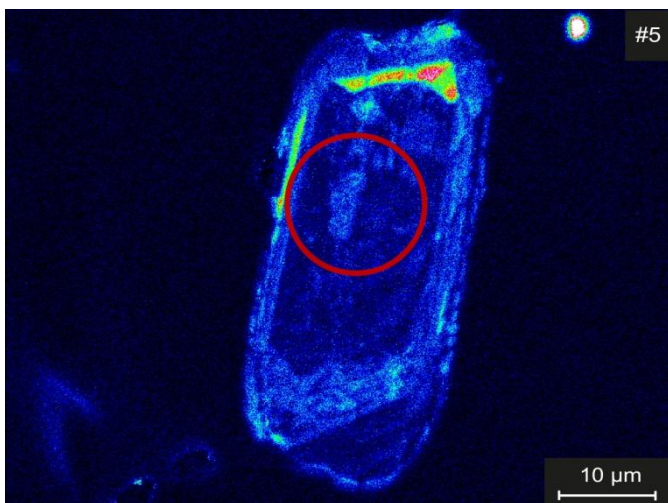
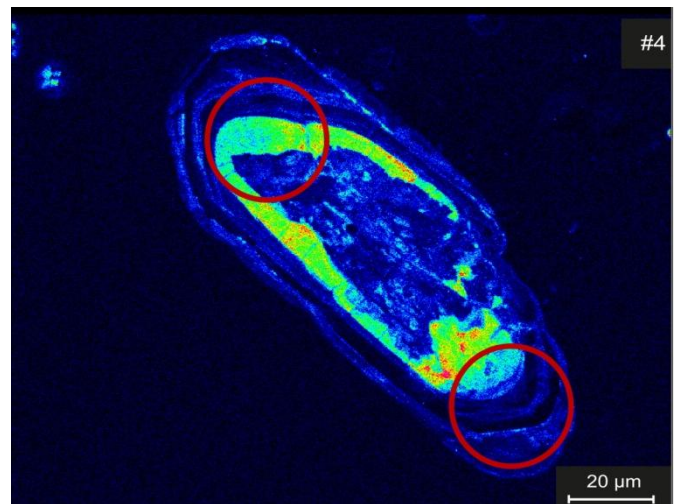
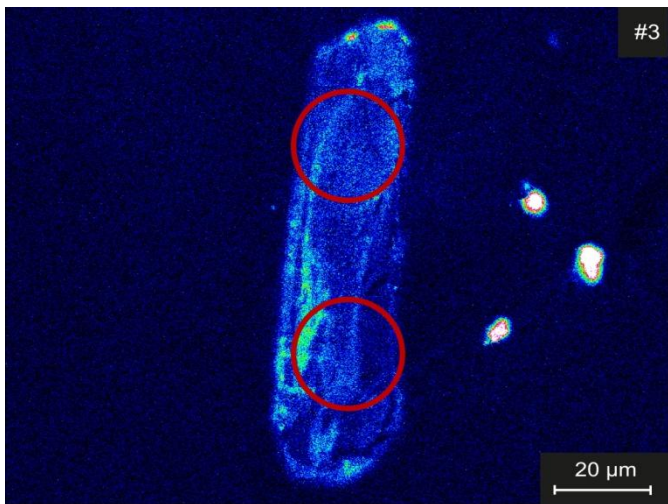
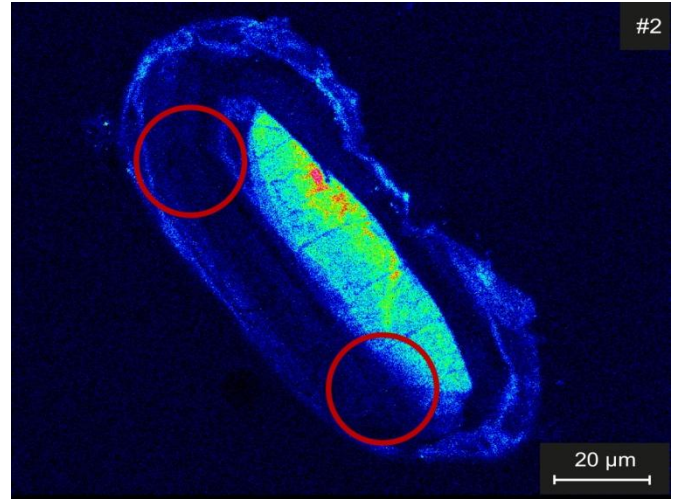
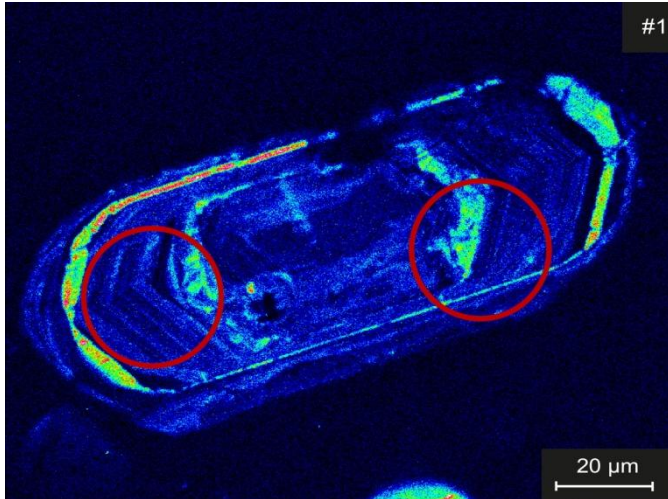
- Logan, W. et al. (1863). Report on the geology of Canada. *Geological Survey of Canada, Progress Report, 983p.*
- Loiselle, M. (1979). Characteristics and origin of anorogenic granites. In *Geological Society of America Abstracts with Programs*, volume 11, page 468.
- Mackenzie, F. T. and Garrels, R. (1971). *Evolution of sedimentary rocks*. Norton New York.
- Marshall, D. (1996). Ternplot: an excel spreadsheet for ternary diagrams. *Computers & Geosciences*, 22(6):697-699.
- Martin, E., Martin, H., and Sigmarsson, O. (2008). Could Iceland be a modern analogue for the Earth's early continental crust? *Terra Nova*, 20(6):463-468.
- Martin, H. (1986). Effect of steeper Archean geothermal gradient on geochemistry of subduction-zone magmas. *Geology*, 14(9):753-756.
- Martin, H. (1987). Petrogenesis of Archean trondhjemites, tonalites, and granodiorites from eastern Finland: major and trace element geochemistry. *Journal of Petrology*, 28(5):921-953.
- Martin, H. (1999). Adakitic magmas: modern analogues of Archean granitoids. *Lithos*, 46(3):411-429.
- Martin, R. F. (2006). A-type granites of crustal origin ultimately result from open-system fenitization-type reactions in an extensional environment. *Lithos*, 91(1-4):125-136.
- McDonough, W. F. and Sun, S.-S. (1995). The composition of the Earth. *Chemical geology*, 120(3-4):223-253.
- Meschede, M. (1986). A method of discriminating between different types of mid-ocean ridge basalts and continental tholeiites with the Nb-Zr-Y diagram. *Chemical geology*, 56(3-4):207-218.
- Montgomery, C. and Hurley, P. (1978). Total-rock UPb and RbSr systematics in the Imataca Series, Guayana Shield, Venezuela. *Earth And Planetary Science Letters*, 39(2):281-290.
- Moyen, J.-F. (2011). The composite Archean grey gneisses: petrological significance, and evidence for a non-unique tectonic setting for Archean crustal growth. *Lithos*, 123(1-4):21-36.
- Moyen, J.-F. and Martin, H. (2012). Forty years of TTG research. *Lithos*, 148:312-336.
- Myers, J. S. (1995). The generation and assembly of an Archean supercontinent: evidence from the Yilgarn craton, Western Australia. *Geological Society, London, Special Publications*, 95(1):143-154.
- Naipal, R. and Kroonenberg, S. (2016). Provenance signals in metaturbidites of the Paleoproterozoic greenstone belt of the Guiana Shield in Suriname. *Netherlands Journal of Geosciences*, 95(4):467- 489.
- Nicollet, C. and Andriambololona, D. R. (1980). Distribution of transition elements in crustal metabasic igneous rocks. *Chemical Geology*, 28:79-90.
- Nisbet, E., Cheadle, M., Arndt, N., and Bickle, M. (1993). Constraining the potential temperature of the Archean mantle: a review of the evidence from komatiites. *Lithos*, 30(3-4):291-307.
- Pearce, J. A. and Cann, J. R. (1973). Tectonic setting of basic volcanic rocks determined using trace element analyses. *Earth and planetary science letters*, 19(2):290-300.
- Pearce, J. A., Harris, N. B., and Tindle, A. G. (1984). Trace element discrimination diagrams for the tectonic interpretation of granitic rocks. *Journal of petrology*, 25(4):956-983.

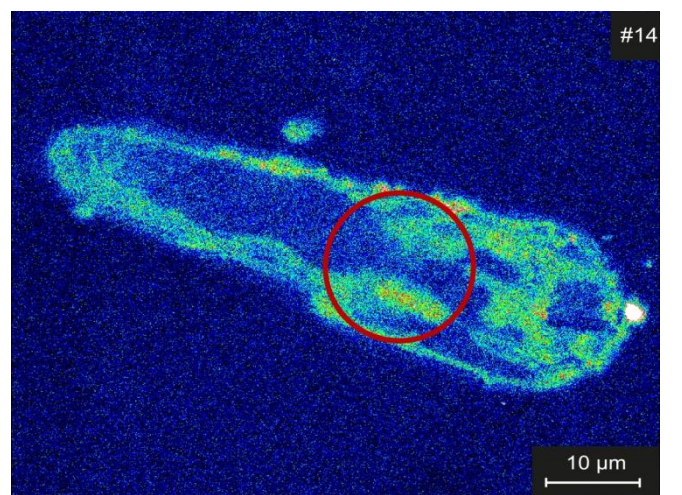
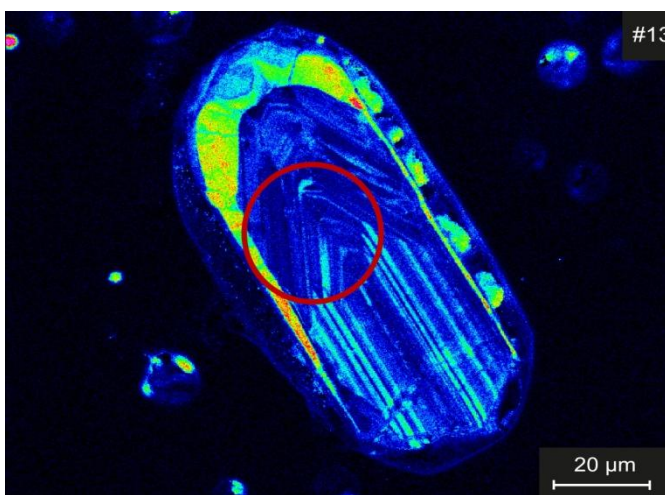
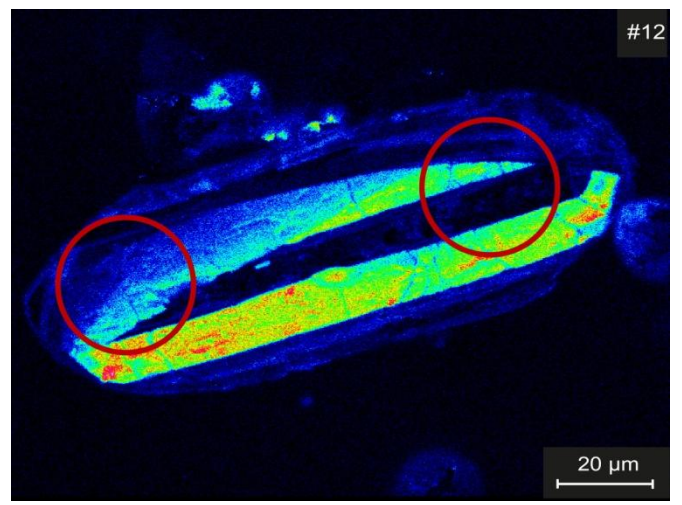
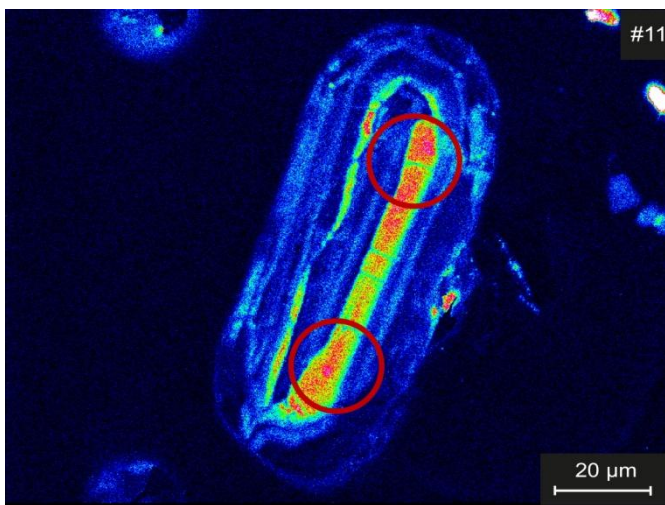
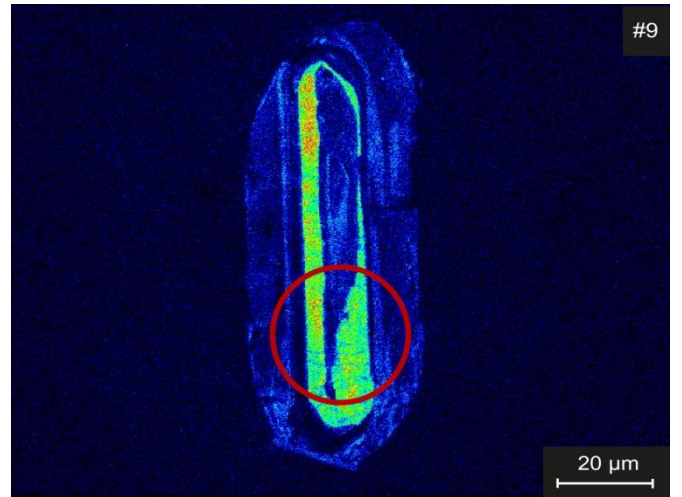
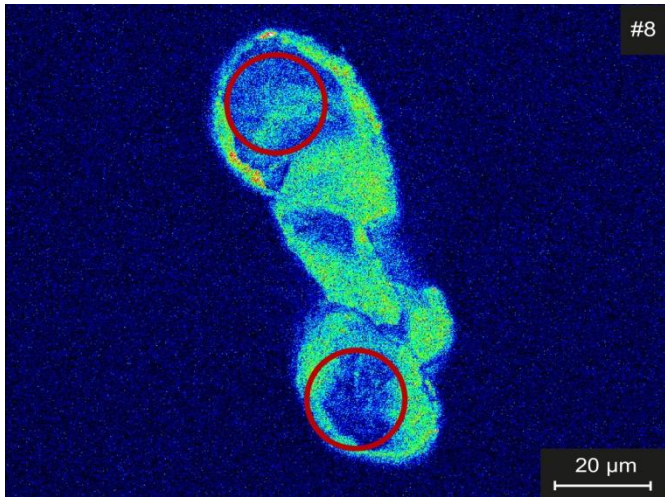
- Reis, N. J., Faria, M. S. G. d., Fraga, L. M. B., and Haddad, R. C. (2000). Orosirian calc-alkaline volcanism and the Orocaina event in the Northern Amazonian Craton, Eastern Roraima State, Brazil.
- Rosa-Costa, L. d., Ricci, P., Lafon, J., Vasquez, M., Carvalho, J., Klein, E., and Macambira, E. (2003). Geology and geochronology of Archean and Paleoproterozoic domains of the southeastern Amapá and northwestern Pará, Brazil-southeastern Guiana Shield. *Geologie de la France*, 2(3):4.
- Saunders, A. D. and Tarney, J. (1984a). Geochemical characteristics of basaltic volcanism within back-arc basins. *Geological Society, London, Special Publications*, 16(1):59-76.
- Saunders, A. D. and Tarney, J. (1984b). Geochemical characteristics of basaltic volcanism within back-arc basins. *Geological Society, London, Special Publications*, 16(1):59-76.
- Schols, H. and Cohen, A. (1951). Geologische overzichtskaart. *Geologisch Mijnbouwkundige Dienst Suriname, Jaarboek*, 1950:11-17.
- Schumacher, J. C. (1988). Stratigraphy and geochemistry of the Ammonoosuc Volcanics, central Massachusetts and southwestern New Hampshire. *American Journal of Science*, 288(6):619-663.
- Siivola, J. and Schmid, R. (2007). List of mineral abbreviations.
- Smithies, H., van Kranendonk, M., and Champion, D. (2006). Did plate tectonics begin in early Archean times? *Penrose conference, Lander, Wyoming*.
- Spear, F. S. and Spear, F. S. (1993). Metamorphic phase equilibria and pressure-temperature-time paths.
- Stern, R. J. (2008). Modern-style plate tectonics began in Neoproterozoic time: An alternative interpretation of Earth's tectonic history. *When did plate tectonics begin on planet Earth*, 440:265-280.
- Stevens, G. (2018). The truth about granites: Realistic phase equilibrium modelling of anatexis with changing bulk composition. *Lecture, Utrecht*.
- Streckeisen, A. L. (1967). Classification and nomenclature of igneous rocks. *N. Jb. Miner.*, 107:144-240.
- Sun, S.-S. and McDonough, W.-S. (1989). Chemical and isotopic systematics of oceanic basalts: implications for mantle composition and processes. *Geological Society, London, Special Publications*, 42(1):313-345.
- Tagini, B. (1971). Esquisse structurale de la Côte d'Ivoire. Essai de géotectonique régionale. *These Univ. Lausanne. Societe d'Etat pour le Developpement miniere de la Cote D'Ivoire*.
- Tajcmanová, L., Connolly, J., and Cesare, B. (2009). A thermodynamic model for titanium and ferric iron solution in biotite. *Journal of Metamorphic Geology*, 27(2):153-165.
- Tozer, C. (1955). The mode of occurrence of sillimanite in the Glen district, Co. Donegal. *Geological Magazine*, 92(4):310-320.
- Van Kranendonk, M. J., Smithies, R. H., Hickman, A. H., and Champion, D. C. (2007). Paleoarchean development of a continental nucleus: the East Pilbara terrane of the Pilbara Craton, Western Australia. *Developments in Precambrian Geology*, 15:307-337.
- Vanderhaeghe, O., Ledru, P., Thiéblemont, D., Egal, E., Cocherie, A., Tegye, M., and Milési, J.-P. (1998). Contrasting mechanism of crustal growth: Geodynamic evolution of the Paleoproterozoic granite-greenstone belts of French Guiana. *Precambrian Research*, 92(2):165-193.

- Veblen, D. R. and Ribbe, P. H. (19982). *Amphiboles: petrology and experimental phase relations*, volume 9B. Walter de Gruyter GmbH & Co KG.
- Veenstra, E. and de Vletter, D. (1983). *Petrology and Geochemistry of Sheet Ston Broekoe, Sheet 30, Suriname*. Geologisch Mijnbouwkundige Dienst van Suriname.
- Waldbaum, D. and Thompson Jr, J. (1968). Mixing properties of sanidine crystalline solutions: IV. Phase diagrams from equations of state. *American Mineralogist: Journal of Earth and Planetary Materials*, 54(9-10):1274-1298.
- Whalen, J. B., Currie, K. L., and Chappell, B. W. (1987). A-type granites: geochemical characteristics, discrimination and petrogenesis. *Contributions to mineralogy and petrology*, 95(4):407-419.
- Walton, B. (1973). The Early Precambrian Gneisses of the Godthab District, West Greenland: Discussion. *Philosophical Transactions of the Royal Society of London Series A*, 273:358.
- White, R., Powell, R., and Holland, T. (2001). Calculation of partial melting equilibria in the system Na<sub>2</sub>O-CaO-K<sub>2</sub>O-FeO-MgO-Al<sub>2</sub>O<sub>3</sub>-SiO<sub>2</sub>-H<sub>2</sub>O (NCKFMASH). *Journal of metamorphic Geology*, 19(2):139-153.
- White, W. M. (2013). *Geochemistry*. John Wiley & Sons.
- Wilson, M. (1989). *Igneous petrogenesis*. Springer, Dordrecht
- Winchester, J. A. and Floyd, P. A. (1977). Geochemical discrimination of different magma series and their differentiation products using immobile elements. *Chemical geology*, 20:325-343.
- Wood, D. A. (1980). The application of a Th-Hf-Ta diagram to problems of tectonomagmatic classification and to establishing the nature of crustal contamination of basaltic lavas of the British Tertiary Volcanic Province. *Earth and planetary science letters*, 50(1):11-30.
- Woodland, B. G. (1963). A petrographic study of thermally metamorphosed pelitic rocks in the Burke area, northeastern Vermont. *American Journal of Science*, 261(4):354-375.
- Yang, N. (2014). The Patamacca Granite in relation to other granitoids in Suriname and the Guiana Shield. Master's thesis.
- Zegers, T. E. and van Keken, P. E. (2001). Middle Archean continent formation by crustal delamination. *Geology*, 29(12):1083-1086.

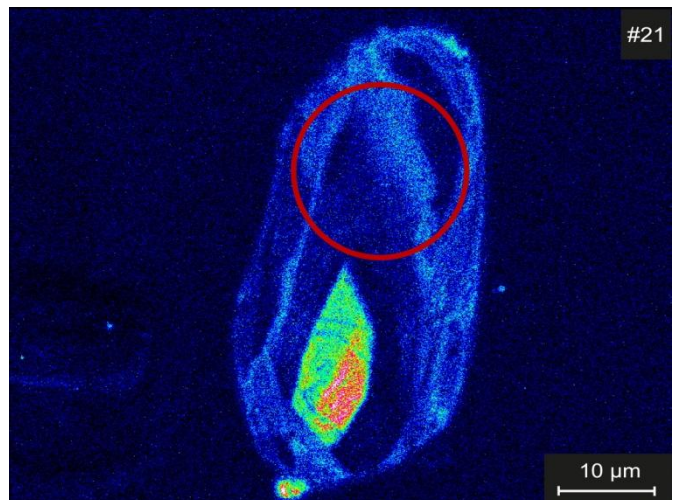
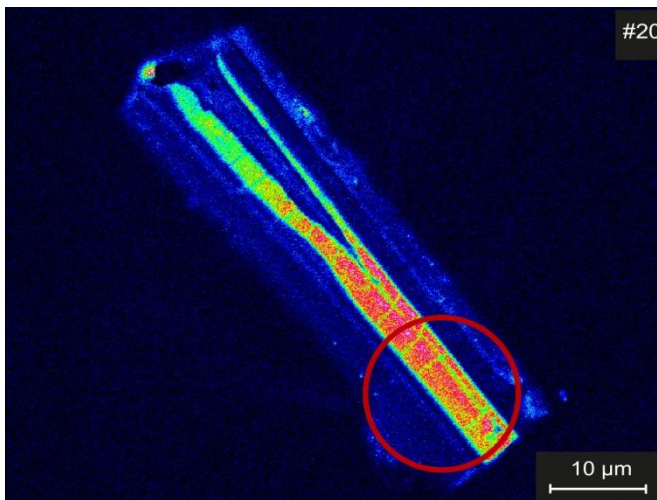
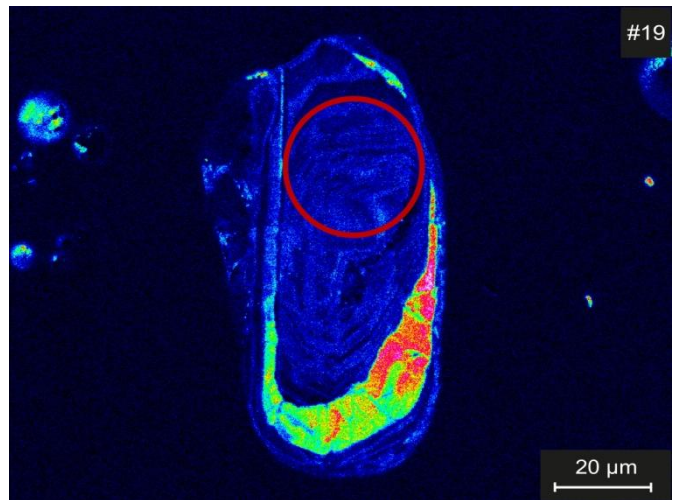
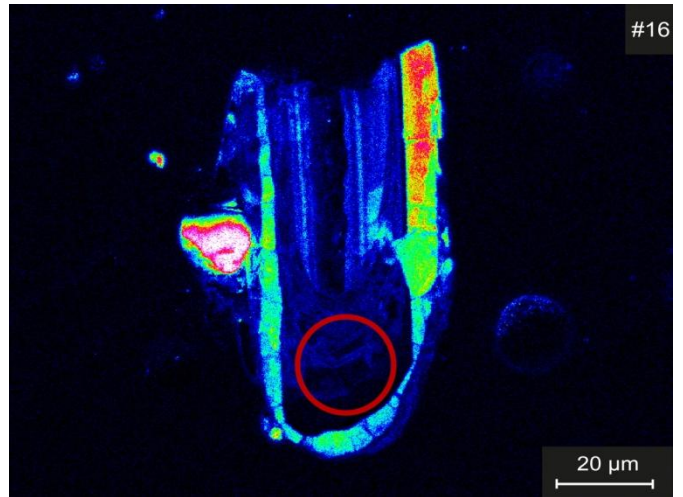
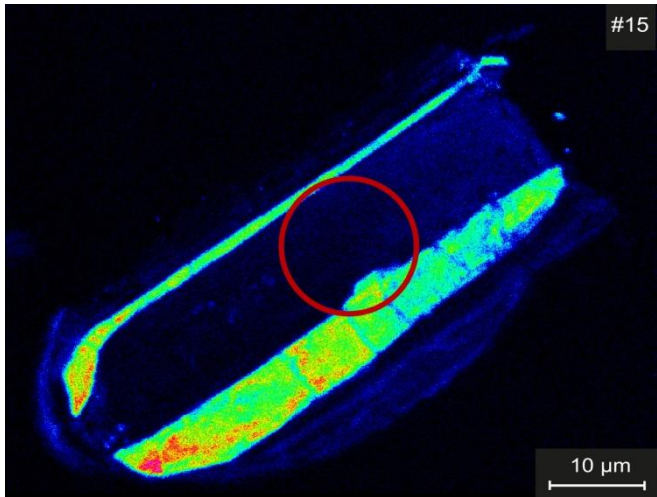
## Appendix A

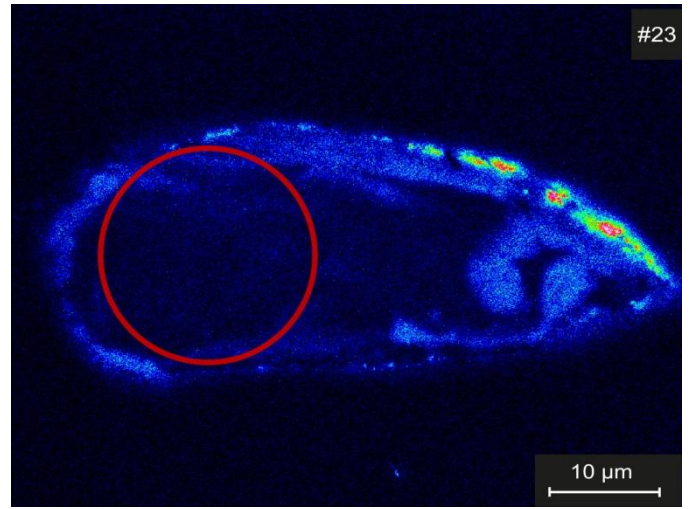
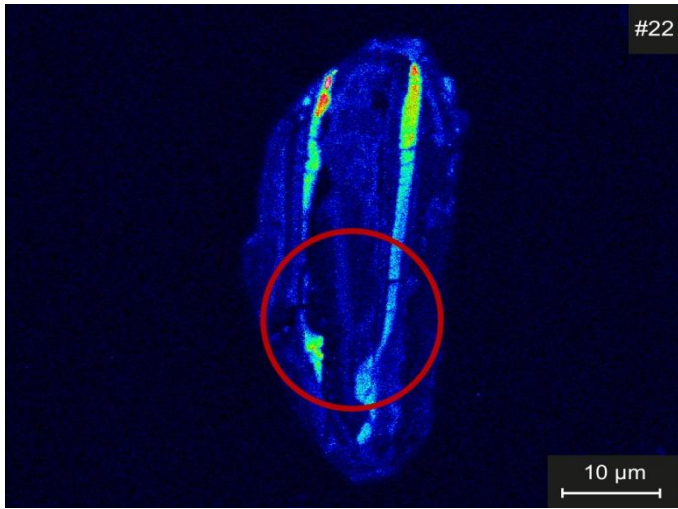
CL images of the eight largest and least altered zircons of KG1006. The red circle is the laser spot during LA-ICP-MS analysis. The number in the top right of each CL image is the measurement number.











## Appendix B

EPM data of garnet and biotite used for geothermometry. Concentrations are in wt.%.

LB106A:

Mineral	#	Si	Ti	K	Ca	Mg	Fe	Mn	Na	Cr	Al	O	Total
Garnet	64	17.75	b.d.	0.01	2.16	3.15	22.57	3.81	0.01	b.d.	11.15	40.64	101.21
	65	17.97	0.00	0.00	2.24	4.06	21.59	2.70	0.00	0.00	11.35	41.11	101.04
	66	17.96	0.00	0.00	2.33	4.16	21.46	2.70	0.01	b.d.	11.36	41.18	101.17
	67	18.01	b.d.	0.00	2.44	4.11	21.41	2.65	b.d.	b.d.	11.34	41.18	101.13
	68	18.06	b.d.	b.d.	2.48	4.05	21.25	2.63	0.01	0.01	11.37	41.21	101.07
	69	18.06	b.d.	0.00	2.58	4.16	21.34	2.58	b.d.	0.01	11.30	41.26	101.28
	70	18.00	b.d.	b.d.	2.62	4.14	20.97	2.55	b.d.	b.d.	11.42	41.18	100.86
	71	17.99	0.01	b.d.	2.63	4.19	21.05	2.50	b.d.	0.00	11.42	41.22	100.99
	72	17.96	0.01	0.00	2.66	4.16	21.02	2.49	0.02	b.d.	11.31	41.08	100.71
	73	17.94	0.01	0.01	2.64	4.16	21.22	2.53	0.01	0.00	11.48	41.27	101.25
	74	17.73	0.01	b.d.	2.59	3.34	22.40	3.00	b.d.	0.01	11.20	40.69	100.95
	75	17.81	0.01	0.00	2.58	3.58	22.04	2.77	b.d.	b.d.	11.32	40.87	100.96
	76	17.89	0.01	0.00	2.56	3.69	22.14	2.65	0.01	b.d.	11.34	41.03	101.30
	77	17.97	b.d.	0.01	2.55	3.98	21.49	2.50	0.00	b.d.	11.32	41.07	100.88
	78	17.99	b.d.	b.d.	2.51	4.24	21.19	2.51	b.d.	0.00	11.40	41.23	101.07
	79	17.96	b.d.	0.00	2.46	4.21	21.39	2.54	b.d.	b.d.	11.36	41.18	101.09
	80	18.05	b.d.	b.d.	2.37	4.24	21.15	2.53	b.d.	0.01	11.47	41.30	101.12
	81	18.02	b.d.	b.d.	2.32	4.23	21.24	2.61	0.00	b.d.	11.40	41.23	101.04
	82	18.05	b.d.	0.00	2.28	4.25	21.41	2.63	b.d.	b.d.	11.38	41.29	101.28
	83	18.00	0.00	b.d.	2.18	4.26	21.49	2.62	0.01	0.01	11.39	41.23	101.18
	84	18.12	0.01	b.d.	2.03	4.25	21.57	2.65	b.d.	0.01	11.36	41.31	101.30
	85	18.04	0.00	b.d.	1.96	4.30	21.49	2.67	0.01	b.d.	11.35	41.19	101.00
	86	17.94	b.d.	b.d.	1.89	4.24	21.75	2.65	0.01	0.01	11.44	41.17	101.10
	87	17.90	b.d.	b.d.	1.78	4.00	22.28	2.72	b.d.	0.00	11.32	40.97	100.97
	Biotite	88	17.88	0.86	6.74	0.04	9.97	9.28	0.05	0.21	0.02	9.11	39.77
89		17.57	0.83	6.56	0.09	9.87	9.63	0.04	0.23	0.00	8.87	39.19	92.89
90		16.83	0.83	6.08	0.28	9.12	9.69	0.07	0.24	b.d.	8.63	37.64	89.40
91		17.22	0.86	6.34	0.18	9.32	9.87	0.06	0.23	0.00	8.92	38.56	91.56
92		17.63	0.87	6.59	0.09	9.53	9.59	0.05	0.23	0.01	9.07	39.24	92.91
93		17.37	0.84	6.26	0.08	9.80	9.92	0.06	0.20	0.01	8.97	39.02	92.52
94		17.77	0.96	6.79	0.04	9.65	9.80	0.05	0.21	b.d.	8.98	39.53	93.77
95		17.73	0.99	6.78	0.02	9.65	9.90	0.04	0.20	0.00	9.02	39.55	93.87
96		17.93	0.96	6.81	0.03	9.54	9.67	0.05	0.18	0.00	9.13	39.72	94.02
97		17.97	0.96	6.84	0.02	9.59	9.56	0.05	0.20	b.d.	9.21	39.84	94.24
98		17.90	0.95	6.84	0.02	9.51	9.38	0.04	0.21	0.00	9.17	39.62	93.63

LB106B:

Mineral	#	Si	Ti	K	Ca	Mg	Fe	Mn	Na	Cr	Al	O	Total
Garnet	143	17.81	b.d.	b.d.	1.84	3.40	22.81	3.39	b.d.	b.d.	11.22	40.77	101.24
	144	17.69	0.01	b.d.	2.00	2.82	24.09	3.28	b.d.	b.d.	11.16	40.60	101.65
	145	17.61	b.d.	0.00	1.93	2.40	23.73	4.17	0.02	0.01	11.07	40.28	101.22
	146*	12.17	0.02	0.07	0.05	12.47	9.66	0.09	0.02	b.d.	11.80	35.41	81.74
	147	17.59	0.01	0.00	1.93	2.16	23.86	4.91	0.01	b.d.	10.93	40.22	101.60
Biotite	138	17.63	0.86	6.78	0.01	9.70	9.81	0.11	0.11	0.02	9.10	39.42	93.54
	139	17.52	0.92	6.76	0.01	9.54	10.08	0.07	0.10	0.01	9.01	39.21	93.23
	140	17.59	0.90	6.79	0.00	9.53	9.83	0.03	0.08	0.02	9.00	39.17	92.93
	141	17.06	0.80	5.89	0.04	9.56	10.44	0.04	0.06	b.d.	9.16	38.65	91.69
	142	17.31	0.84	6.52	0.01	9.71	9.53	0.05	0.06	b.d.	9.22	38.98	92.23

\*Measurement #146 was not used in the chemical profiles because the total concentration was too low due to an analytical error.